ABSTRACT

JIA, TAO. Single and Multicarrier Adaptive Transmission Systems with Long-Range Prediction Aided by Noise Reduction. (Under the direction of Professor Alexandra Duel-Hallen).

Adaptive transmission methods have evolved as one of the key enabling technologies to meet the increasing demand for high-speed wireless data access services. In this dissertation, we address several adaptive transmission systems and techniques required for their implementation.

First, we focus on multicarrier code-division multiple access (MC-CDMA) system with adaptive frequency hopping (AFH). A suboptimal water-filling (WF) channel allocation algorithm was previously proposed for the reverse link of this system. To overcome the limitations of the WF algorithm in the presence of fading-induced near-far problem, a new allocation algorithm is proposed and demonstrated to improve performance when the conventional matched filter (MF) receiver is employed. Moreover, the allocation methods are extended to accommodate multiuser detectors (MUDs) at the receiver for MC-CDMA system with AFH. It is demonstrated that the combination of the improved allocation algorithm and the linear MUDs is very efficient in mitigating fading and multi-access interference (MAI) for realistic mobile radio channels with correlated subcarriers, channel state information (CSI) mismatch, and imperfect power control. Numerical results show that the proposed adaptive transmission method has much greater system capacity than conventional non-adaptive MC direct-sequence (DS)-CDMA system.

Second, the adaptive modulation (AM) system is investigated. To ensure high spectral efficiency (SE) for AM systems, the CSI needs to be predicted to compensate for the feedback and data processing delay and system constraints. The long-range prediction (LRP) method achieves high prediction accuracy at practical predication ranges when the signal-to-noise ratio (SNR) of the observations is sufficiently high. However, its accuracy degrades severely at low and medium SNR. Hence, the noise reduction (NR) techniques are required for the LRP to achieve the desired prediction accuracy. A novel data-aided noise reduction (DANR) method is proposed. The DANR includes an adaptive pilot transmis-

sion mechanism, robust noise reduction, and decision-directed channel estimation. Due to improved prediction accuracy and low pilot rates, the DANR results in higher SE than previously proposed NR techniques, which rely on oversampled pilots. While adaptive coded modulation (ACM) is more sensitive to prediction errors than uncoded adaptive modulation (UAM), this DANR method maintains the coding gain and outperforms previous investigated prediction methods in terms of SE at practical prediction ranges. It is also demonstrated that adaptive modulation aided by LRP has better performance for the realistic physical model than for the Jakes model in the practical SNR range.

Finally, we investigate the orthogonal frequency division-multiplex (OFDM) system with adaptive bit-interleaved coded modulation (ABICM) aided by LRP. New ABICM methods based on the expurgate bound are proposed. They achieve better bit-error rate (BER) accuracy than the existing method. In particular, one of the proposed methods generates the BER that is very close to the specified target BER. Compared with ACM and UAM, the ABICM is much less sensitive to prediction errors. However, the LRP technique still significantly improves the SE of ABICM over the outdated CSI method at practical prediction ranges.

In summary, we address several important problems in the implementation of single and multicarrier adaptive transceivers. In particular, we design an improved allocation algorithm to efficiently exploit the predicted CSI in the MC-CDMA system with AFH. Combined with MUDs, this system achieves higher system capacity than the non-adaptive MC-CDMA systems. Next, a DANR technique is proposed for single-carrier adaptive modulation system. Due to improved prediction accuracy and low pilot rates, the DANR results in higher SE than previously proposed NR techniques, which rely on oversampled pilots. Finally, we investigate ABICM, which is less sensitive to the prediction errors than UAM and adaptive trellis coded modulation (ATCM). New adaptation methods that achieve improved BER accuracy are proposed for ABICM. It is demonstrated that with the aid of LRP, the OFDM system with ABICM maintains high SE at long prediction ranges.

Single and Multicarrier Adaptive Transmission Systems with Long-Range Prediction Aided by Noise Reduction

by

Tao Jia

A dissertation submitted to the Graduate Faculty of
North Carolina State University
in partial fullfillment of the
requirements for the Degree of
Doctor of Philosophy

Electrical Engineering

Raleigh, North Carolina

2008

APPROVED BY:

Dr. Brian L. Hughes	Dr. Huaiyu Dai
Dr. Alexandra Duel-Hallen Chair of Advisory Committee	Dr. Hans Hallen Co-chair of Advisory Committe

DEDICATION

To my parents

To my wife *Han*

BIOGRAPHY

Tao Jia received his B. S. degree in electronics and M. Eng. degree in electrical engineering, both from Peking University, Beijing, China, in 2001 and 2004, respectively. At Peking University, he worked in the area of digital CDMA transceiver implementation on FPGA and digital signal processor. From 2001 to 2004, he was a part-time intern at Intel China Research Center, where he did research on the acoustic and audio speech signal processing topics. In August 2004, He started his Ph. D. study at North Carolina State University. Under the advisory of Professor Alexandra Duel-Hallen, his research topics include multicarrier CDMA system with adaptive frequency hopping, prediction and estimation of fading channels, and adaptive modulation techniques.

ACKNOWLEDGMENTS

This dissertation would never have become reality without the help and suggestions from many people, only a proportion of which I have space to acknowledge here.

First, I would like to express my gratitude to my advisor, Dr. Alexandra Duel-Hallen, for her supervision, support and encouragement throughout my four-year Ph. D. study at North Carolina State University. I truly appreciate her help in developing my research skills, writing technical papers, preparing my presentations, and planning my career.

I would like to thank Dr. Hans Hallen for his time as the co-chair of my advisory committee, and for his help and instructions on the research of long-range prediction. I would also like to thank Dr. Brian L. Hughes and Dr. Huaiyu Dai for serving as my advisory committee members. Their courses on communication and signal processing have provided me with the fundamental knowledge required for this dissertation.

It was my pleasure to have worked closely with my colleagues in Dr. Duel-Hallen's group: Dr. Ming Lei, Dr. Jia Liu, Dr. Li Ma, Shailesh Jha, and Ayon Quayum. I have benefited significantly from enlightening discussions with them.

Last but not least, I am grateful for my family who have encouraged and supported me. I thank my parents for rising me up and their unconditional love. I am so fortunate to have my wonderfully wife *Han*, who stood behind me though the development of this dissertation. This dissertation is dedicated to them.

TABLE OF CONTENTS

LIST OF TABLES

LIST OF FIGURES

LIST OF ABBREVIATIONS AND ACRONYMS

ABICM adaptive bit-interleaved coded modulation

ACM adaptive coded modulation

AFH adaptive frequency hopping

AM adaptive modulation

AR autoregressive

ATCM adaptive trellis coded modulation

AWGN additive white Gaussian noise

BER bit-error rate

BICM bit-interleaved coded modulation

BPSK binary phase shifted keying

CDMA code-division multiplex access

CP cyclic prefix

CSI channel state information

DANR data-aided noise reduction

DS-CDMA direct-sequence code-division multiplex-access

FFT fast Fourier transform

IFFT inverse fast Fourier transform

ISI inter-symbol interference

LDD linear decorrelating detector

LP linear prediction

LRP long-range prediction

MAI multiple-access interference

MC DS-CDMA multicarrier direct-sequence code-division multiple-access

MC-CDMA multicarrier code-division multiplex-access

MF matched filter

ML maximum likelihood

MMSE minimum mean square error

MQAM multiple quadrature amplitude modulation

MRC maximum ratio combining

MSE mean square error

MUD multiuser detection

NMSE normalized mean square error

NPMSE normalized prediction mean square error

NR noise reduction

OFDMA orthogonal frequency-division multiple access

OFDM orthogonal frequency division-multiplex

PDF probability density function

PEP pair-wise error probability

QPSK quadrature phase shifted keying

SE spectral efficiency

SIC successive interference canceller

SINR signal to interference and noise ratio

SNR signal-to-noise ratio

SOS sum-of-sinusoidal

TCM trellis coded modulation

UAM uncoded adaptive modulation

WLAN wireless local area networks

WMAN wireless metropolitan networks

Chapter 1

Introduction

1.1 Adaptive Transceivers

In the past decade, the wireless communication industry has experienced explosive growth. Cellular phones have become ubiquitous in people's daily life. The wireless local area networks (WLAN) have replaced wired networks in many homes, universities, and companies. The evolving forth generation (4G) cellular networks and wireless metropolitan networks (WMAN) will further change the way we access the internet today.

The demand for high-quality mobile internet services has increased significantly lately. Both the 4G cellular networks and wireless metropolitan networks (WMAN) are intended to provide broadband services to the mobile terminals. Since these systems are designed to support mobile multimedia services, the amount of information that needs to be transmitted over the wireless links is enormous. However, the bandwidth available to those services is usually limited, considering the large number of potential users. Hence, efficient utilization of limited bandwidth has been an active area for the wireless communication research.

In addition to the bandwidth efficiency, another technical challenge that must be addressed to enable mobile radio application is to maintain the quality of the wireless link. As the signal propagates through a mobile radio channel, it experiences random fluctuations

in both time and frequency domain due to changing reflections and attenuation as the transmitter or receiver moves. Hence, transceivers with fixed parameters are not expected to achieve high bandwidth efficiency while maintaining the quality of service. On the other hand, the "smart" transceivers that can adapt themselves to the varying channel conditions have attracted significant attention. While the original idea of adaptive transceivers can be dated back to as early as 1968 [1], this is still an active area of research in the twenty-first century [2, 3].

In adaptive transceivers, the reaction to the changes in channel quality is usually divided into the following steps [2]:

1. Prediction: To select the appropriate transmission parameters, the channel state information (CSI) has to be estimated. Since there is always a time difference between the time that the channel is measured and the time that the corresponding transmission is made, prediction is required to maintain the reliability of CSI.

2. Adaptation: Based on the estimated channel condition, the transmitter selects the appropriate modulation and transmission parameters for the following transmission.

3. Signaling of employed parameters or CSI feedback: When the adaptation decision is performed at the receiver/transmitter, the transmitter/receiver needs to be informed about the selected transmission parameters.

In this dissertation, we focus on the the first two steps: prediction and adaptation.

1.2 Long-Range Prediction

To enable adaptive transceivers, accurate CSI is required for the adaptation. In some mobile radio systems, the CSI is estimated at the receiver and fed back to the transmitter. In other systems, the adaptation decisions are made at the receiver and only the decisions are fed back to the transmitter. In either case, unless the mobile speed is very low, the estimated CSI quickly becomes outdated due to the fast varying channel condi-

tion. Hence, the estimated CSI cannot be used directly to select the parameters of adaptive transceiver. To enable adaptive transceiver for mobile radio systems, prediction of future fading channel coefficient is required.

In adaptive transceivers, the feedback delay can vary from a fraction of a millisecond to several milliseconds [4], which is much longer than the symbol duration. As a result, the prediction ranges of predictor are typically much larger than in channel estimation methods. Hence, the prediction techniques designed to enable adaptive transceiver are termed as "long-range prediction (LRP)" in literature [5, 4].

The LRP algorithms can be classified into three categories according to the their channel model: autoregressive (AR), sum-of-sinusoidal (SOS), and band-limited process model based algorithms. Different channel model leads to different LRP algorithms.

For AR model based algorithms, the AR coefficients are estimated from noisy channel observations. Previously, modified covariance, Burg, least mean square (LMS), recursive least square (RLS), QR-decomposition-based RLS, affine projection were proposed [6]. In [6], it was shown that the modified covariance methods achieves the best performance among all these methods. However, Baddour and Beaulieu showed that the Burg predictor slightly outperforms the modified covariance predictor in their channel model [7].

The frequently used SOS model based algorithms are ROOT MUSIC and ESPRIT [8, 9]. Recently, a low-complexity ESPRIT algorithm was proposed in [10]. It uses the subspace tracking method to track the frequency changes of sinusoidals.

Band-limited process model-based prediction algorithms were proposed in [11, 12, 13]. In those algorithms, some time-concentrated and band-limited sequences are selected as the base functions. Then the observed fading process is decomposed using these basis functions. Finally, the channel prediction is obtained by extrapolating these basis functions.

The performance of AR model-based and SOS-based algorithms was compared in [6]. When fixed parameter SOS models, e.g., the Jakes model, are employed, the SOS-based methods outperform the AR model-based algorithms. However, when more complex, non-stationary channel model is applied, the AR model-based algorithms perform better.

The band-limited process model-based prediction algorithms have not been investigated for non-stationary models [4]. Since non-stationary channels are usually encountered in practice, we will focus on the AR model-based algorithms in this dissertation. In addition to the Jakes model, we employ our realistic physical model [4, 5, 14] to test the proposed prediction methods.

In the originally proposed AR model-based predictor, the channel is sampled at a low sampling rate, which is slightly higher than the Nyquist sampling rate. The channel observations can be obtained by transmitting pilot symbols. For example, a sampling rate of five times of the maximum Doppler frequency is frequently used [5, 15]. This low sampling rate enables us to exploit the large sidelobes of the autocorrelation function of the fading channel when the order of predictor is limited. For high signal-to-noise ratio (SNR), the predictor achieves very small mean square error (MSE). For example, the MSE at prediction range of 0.2 wavelengths is as low as 10^{-3} when the SNR is higher than 60 dB [5]. However, the MSE strongly depends on the SNR of channel observations. When the SNR is lower than 20 dB, the prediction MSE is higher than 0.1 at the same prediction range [16]. To maintain the reliability of CSI, highly oversampled pilots can be transmitted to enable noise reduction (NR) prior to prediction [7, 15]. These NR techniques significantly improve the prediction accuracy at practical SNR levels. However, the transmitted high-rate pilots usually consume a large portion of the available bandwidth.

In this dissertation, we focused on how to improve the prediction accuracy without sacrificing the spectral efficiency (SE) of the adaptive systems. A novel data-aided noise reduction (DANR) method is proposed for the LRP-aided adaptive modulation (AM) system [16, 17]. This method comprises an adaptive pilot transmission mechanism that compensates for outages, robust NR and decision-directed channel estimation. Due to the exploitation of data decisions, the noise power in the channel observations is significantly reduced, while the pilot symbols only occupy a small portion of the bandwidth. This DANR method achieves higher SE in AM systems than the traditional pilot-based methods.

1.3 Adaptive Modulation and Coding

At the inception of adaptive modulation, Hayes proposed the adaptation of transmission power when the channel quality varies [1]. The drawback of this approach is that it increases the peak power of transmission as well as the instantaneous power of interference to other users. As a consequence, high-linearity power amplifier, which has low power efficiency, is required for such system [2]. To overcome this problem, the adaptive multiple quadrature amplitude modulation (MQAM) schemes that change the constellation sizes according to the channel quality were proposed in [18, 19] using star shaped MQAM constellations. Later, the square-shaped MQAM constellations were applied in [20]. Goldsmith and Chua showed that the variable-power variable-rate MQAM scheme has 5-10 dB power gain over variable-power fixed-rate modulation [21]. Moreover, it was shown that the SE of constant-power variable-rate scheme is very close to that of variable-power variable-rate modulation [21].

To further improve the system capacity, the trellis or lattice codes are imposed on the adaptive MQAM [22, 23, 24, 25]. The resulting method is usually termed as adaptive coded modulation (ACM) or adaptive trellis coded modulation (ATCM). By adopting the set partition of well known trellis coded modulation (TCM), the trellis codes designed for the additive white Gaussian noise (AWGN) channel is applied in those papers. This scheme achieves coding gain in the fading channel when the CSI is accurate. However, it was also shown that this coding gain diminishes as the reliability of CSI degrades [23, 17]. We investigated the performance of uncoded adaptive modulation (UAM) and ACM enabled by the LRP that utilizes DANR for rapidly varying mobile radio channels. Due to improved prediction accuracy and low pilot rate, the DANR-aided LRP outperforms previously proposed prediction methods that rely on oversampled pilots to achieve NR. While ACM is more sensitive to prediction errors than UAM, utilization of DANR substantially increases its SE relative to previously proposed methods.

Interleaving was introduced to maintain the SE of ACM [26]. In this scheme, the

coded bits are interleaved before mapping to the MQAM symbols. Due to the time-diversity caused by interleaving, it performs better than the original ATCM scheme when the CSI is unreliable. However, since there are still uncoded bits, the improvement is limited. Ormeci et. al. proposed adaptive bit-interleaved coded modulation (ABICM), in which all information bits are encoded and interleaved [27]. Although this scheme has reduced Euclidean distance compared with the ATCM, it significantly outperforms the latter under unreliable CSI.

In this dissertation, we also investigate ABICM. In [27], the Bhattacharyya bound of single-bit-error probability is considered to determine the constellation size while maintaining the target bit-error rate (BER). Due to the fact that this method produces only coarse estimate of to the BER, the simulated BER deviates from the target BER significantly in some scenarios. We propose to use more accurate expurgated bounds to calculate the BER. When this method is applied to determine the constellation size and symbol energy required to maintain the target BER, the simulated BER is very close to the target BER. Moreover, the performance of this ABICM method in the LRP-aided orthogonal frequency division-multiplex (OFDM) system is evaluated. For practical prediction range and SNR levels, the ABICM outperforms both UAM and ATCM. The ATCM only achieves higher SE when the prediction range is less than 0.1 wavelength. Although ABICM is less sensitive to the quality of CSI than ATCM and UAM, we demonstrate that the LRP technique is still needed to maintain its SE.

1.4 Multicarrier CDMA with Adaptive Frequency Hopping

In addition to AM, we investigate another adaptive transmission system - multicarrier code-division multiplex-access (MC-CDMA) with adaptive frequency hopping (AFH).

MC-CDMA is a multiple access method that combines code-division multiplex access (CDMA) and OFDM techniques. The multicarrier CDMA has three popular implementation schemes: MC-CDMA, multicarrier DS-CDMA, and multitone CDMA [28]. For

all these schemes, each user is allowed to transmit on all or some of the subcarriers, thus achieving frequency diversity. One or more signature codes are assigned to each user so that it is possible to differentiate the signal transmitted by multiple users at the receiver. As in OFDM, both transmitter and receiver in MC-CDMA system employ the fast Fourier transform (FFT) device to reduce complexity.

During the past decade, several MC-CDMA systems with adaptive frequency hopping (AFH) were proposed for cellular communication systems in [29, 30, 31] and have attracted significant attention due to their excellent spectral efficiency. In these systems, the data of each user is multiplexed over one or several substreams, and multiple subcarriers are employed to transmit the substreams of all users. Direct sequence spread spectrum (DS/SS) codes are assigned to all substreams in the system. Each substream is transmitted on one subcarrier. The subcarriers are allocated using the knowledge of the CSI. MC-CDMA with AFH exploits both frequency and multiuser diversity and was shown to improve on non-adaptive MC direct-sequence (DS)-CDMA system in [32].

For the reverse link, a MC-CDMA system with AFH was investigated in [29]. In this system, multiple substreams are employed for each user, and random signature sequences are assigned for all substreams, resulting in enhanced MAI and intra-user interference. A sub-optimal water-filling (WF) allocation algorithm was proposed, and it was demonstrated this system has better performance than direct-sequence code-division multiplex-access (DS-CDMA) system with RAKE receiver and the non-adaptive multicarrier direct-sequence code-division multiple-access (MC DS-CDMA) system [29]. However, the WF algorithm offers limited protection to weaker users. Thus, it suffers from the near-far problem caused by short-term fading and imperfect power control. As a result, the bit error rate (BER) of the WF method is degraded in moderate-to-high signal-to-noise ratio (SNR) region.

In this dissertation and [33, 34], we investigated an improved MC-CDMA system with AFH for the reverse link. This system exploits realistic quasi-synchronous reverse link model [35] and utilizes orthogonal spreading sequences for all substreams of the same

user, thus eliminating intra-user interference. Moreover, we proposed a new allocation algorithm to overcome the limitations of the WF algorithm in [29], and demonstrate the resulting BER improvement. In addition to the traditional matched filter (MF) receivers, we also employed the MUDs jointly with the proposed allocation algorithm by utilizing the signal to interference and noise ratio (SINR) analysis [33]. Performance gains achieved using the multiuser detection (MUD) combined with the proposed allocation method are demonstrated.

1.5 Dissertation Outline

This dissertation focuses on the single and multicarrier adaptive tranmission systems aided by long-range prediction.

In Chapter 2, we investigate the MC-CDMA system with AFH. First, the existing systems and adaptive allocation algorithms are briefly reviewed in Section 2.1. Then the reverse link model of this system is described in section 2.2. Section 2.3 analyzes the limitations of the existing water-filling allocation method, and describes the proposed allocation algorithm. Numerical results and conclusion are contained in section 2.4 and section 2.5, respectively.

In Chapter 3, we consider the data-aided noise reduction (DANR) technique for the LRP-aided AM systems. The existing prediction methods for AM system are reviewed in section 3.1. Then we describe coded and uncoded AM systems in section 3.2. The DANR technique is presented in Section 3.3. Both the standard Jakes model and a realistic physical model are employed to test the performance of this DANR technique in section 3.4. Finally, conclusions are provided in section 3.5.

In Chapter 4, the improved ABICM method for OFDM system is presented. We summarize the existing ACM schemes in section 4.1. Then we describe the model of OFDM system aided by LRP in section 4.2. Section 4.3 discusses the original and new ABICM methods. Simulation results and conclusions are contained in section 4.4 and 4.5, respec-

tively.

Finally, the conclusions of this dissertation are provided in Chapter 5.

Chapter 2

Multicarrier CDMA with Adaptive Frequency Hopping

2.1 Introduction

MC-CDMA methods have been extensively investigated and proposed for future mobile radio systems due to their high spectral efficiency, the interference suppression capability, the exploitation of frequency diversity, and the ability to adapt to time-varying channel conditions [28, 36, 37, 38]. During the past decade, several MC-CDMA systems with AFH were proposed for cellular communication systems in [29, 30, 31] and have attracted significant attention due to their excellent spectral efficiency. In these systems, the data of each user is multiplexed over one or several substreams, and multiple subcarriers are employed to transmit the substreams of all users. Direct sequence spread spectrum (DS/SS) codes are assigned to all substreams in the system. Each substream is transmitted on one subcarrier. The subcarriers are allocated using the knowledge of the channel state information (CSI). MC-CDMA with AFH exploits both frequency and multiuser diversity and was shown to improve on non-adaptive MC direct-sequence (DS)-CDMA system in [32].

In [30], a MC-CDMA system with AFH was proposed for the forward link. In this system, one substream/user is employed, and each user selects the subcarrier with the

largest fading amplitude for transmission. This allocation algorithm provides significant performance improvement over other diversity techniques such as non-adaptive MC DS-CDMA with the maximum ratio combining (MRC) [32]. However, this simple allocation algorithm does not take into account the multiple-access interference (MAI) present in realistic wireless systems. A near-optimal allocation algorithm was utilized in [39] to maximize the total signal to interference and noise ratio (SINR) and was shown to improve on the performance of the simple allocation policy in [30].

For the reverse link, a MC-CDMA system with AFH was investigated in [29]. In this system, multiple substreams are employed for each user, and random signature sequences are assigned for all substreams, resulting in enhanced MAI and intra-user interference. A sub-optimal water-filling (WF) allocation algorithm was proposed, and it was demonstrated this system has better performance than DS-CDMA system with RAKE receiver and the non-adaptive MC DS-CDMA system [29]. However, the WF algorithm offers limited protection to weaker users. Thus, it suffers from the near-far problem caused by short-term fading and imperfect power control. As a result, the bit error rate (BER) of the WF method is degraded in moderate-to-high SNR region.

In this dissertation and [33, 34], we investigate an improved MC-CDMA system with AFH for the reverse link. This system exploits realistic quasi-synchronous reverse link model [35] and utilizes orthogonal spreading sequences for all substreams of the same user, thus eliminating intra-user interference. Moreover, we propose a new allocation algorithm to overcome the limitations of the WF algorithm in [29], and demonstrate the resulting BER improvement.

MAI severely limits performance of spread spectrum systems. While it has been demonstrated that MUD can greatly improve spectral efficiency of DS-CDMA [40] and non-adaptive MC-CDMA [28, 41], to the best of our knowledge, it has not been utilized in MC-CDMA with AFH. In this dissertation, we employ the MUDs jointly with the proposed allocation algorithm by utilizing the SINR analysis [33]. Performance gains achieved using the MUD combined with the proposed allocation method are demonstrated. To reduce the

complexity of the allocation algorithm combined with linear MUDs, recursive update of the matrix inverse is utilized.

In previous research on MC-CDMA with AFH [29, 30], perfect knowledge of the CSI at the transmitter and independent fading for all subcarriers were assumed in the performance evaluation. These assumptions are too optimistic for realistic wireless channels. The impact of noisy CSI measurements was considered in [30, 31]. However, imperfect CSI is mainly caused by the feedback delay associated with sending channel allocation instructions from the base station to mobile users in a rapidly varying fading channel. While the impact of imperfect CSI has been studied extensively for other adaptive transmission systems [5, 15, 4, 16], this investigation has not been carried out for the MC-CDMA system with AFH. In addition, it is well known that correlated subcarriers reduce the frequency diversity of MC systems [42], and the assumption of independent subcarriers tends to overestimate the system performance [34]. In this dissertation, both imperfect CSI and correlated subcarriers are considered in the evaluation of system performance.

2.2 System Model

2.2.1 Transmitted Signal

System diagram of MC-CDMA with AFH is illustrated in Figure 2.1. In the system with K users, the total bandwidth W is divided into M subcarriers with equal bandwidths $\Delta f = W/M$. The data stream of each user is multiplexed over N substreams, and all substreams are spread by spreading codes in time domain. The low-pass equivalent signal at time t for the nth substream of the kth user is (see Table 2.1)

$$x_{k,n}(t)=\sqrt{2E_b}\sum_{l=-\infty}^{\infty}\sum_{i=0}^{PG-1} b_{k,n}(l)c_{k,n}(i)h(t-lT_b-iT_c) \tag{2.1}$$

where $b_{k,n}(l)\in\{-1,+1\}$ are the binary phase shifted keying (BPSK) modulated information symbols. The spreading code vector for this substream is defined as

$$\boldsymbol{c}_{k,n}=\Big[c_{k,n}(0) \quad c_{k,n}(1) \quad \dots \quad c_{k,n}(PG-1)\Big]^T \tag{2.2}$$

with $||\boldsymbol{c}_{k,n}|| = 1$, where $|| * ||$ is the Euclidean norm, and PG is the processing gain. The chip waveform $h(t)$ satisfies $\int_{-\infty}^{\infty} h^2(t) = 1$.

After spreading, the substream (k, n) is assigned to the $q_{k,n}$th subcarrier, where $q_{k,n} \in [1, \ldots, M]$. The subcarrier allocation is performed by a control unit at the base station based on the CSI received from the mobiles, and the channel allocation instructions $\{q_{k,n}\}$ are sent to each mobile via a forward control channel. As in [29], more than one substream of the same user can hop onto the same subcarrier. The total number of substreams assigned to the mth subcarrier is P_m. Note the bit energy E_b is the same for each substream independent of its subcarrier allocation. Thus, power control that adapts to large-scale fading variation is assumed. Better system performance can be achieved by combining subcarrier allocation and per-subcarrier power control, i.e., the power control that compensates for small-scale fading variations. However, the latter would increase the required feedback rate from the base station to the mobile users. Moreover, joint allocation of subcarrier and power is very complex. In contrast, our method exploits both frequency and multiuser diversity while maintaining relatively low complexity.

While it is not practical to maintain orthogonality among substreams of different users [29, 35], it is feasible to require it for each user k, i.e., $\boldsymbol{c}_{k,n}^T \boldsymbol{c}_{k,n} = 0$ for $n' \neq n$. These orthogonal codes are obtained by first assigning random spreading codes to all users and then multiplying the substreams of user k by orthogonal Walsh codewords [33, 43].

The low-pass equivalent transmitted signal for the kth user is the sum of modulated substream signals $S_k(t) = \sum_{n=1}^{N} x_{k,n}(t) \exp(-j2\pi f_{q_{k,n}} t)$, where $f_{q_{k,n}}$ is the subcarrier frequency offset from the carrier frequency f_c for the $q_{k,n}$th subcarrier.

2.2.2 Channel Model and Imperfect CSI

We assume slowly varying flat Rayleigh fading for each subcarrier. The channel coefficients $\gamma_{k,m}(t)$ of all subcarriers are identically distributed with $E[|\gamma_{k,m}(t)|^2] = 1$, and are independent for different users. Denote the amplitude $\alpha_{k,m}(t) = |\gamma_{k,m}(t)|$ and the phase $\phi_{k,m}(t) = \angle\gamma_{k,m}(t)$.

Table 2.1: Notation

K	number of users
M	number of subcarriers
N	number of substreams/user
k, k'	user indices
m, m'	subcarrier indices
n, n'	substream indices for a user
p, p'	substream indices on a given subcarrier
(k, n)	the nth substream of the kth user
E_b	bit energy
N_0	power spectral density of channel Gaussian noise
T_c	chip duration
T_b	bit duration
PG	processing gain $=T_b/T_c$
Δf	subcarrier bandwidth
σ_d	rms delay spread
$q_{k,n}$	allocation variable for substream (k, n)
$\gamma_{k,m}(t)$	fading coefficient on the mth subcarrier of user k
$\hat{\gamma}_{k,m}(t)$	prediction of $\gamma_{k,m}$
$\alpha_{k,m}(t)$,$\hat{\alpha}_{k,m}(t)$	amplitudes of $\gamma_{k,m}(t)$, $\hat{\gamma}_{k,m}(t)$
$\phi_{k,m}(t)$	phase of $\gamma_{k,m}(t)$
η	cross-correlation between $\gamma_{k,m}(t)$ and $\hat{\gamma}_{k,m}(t)$
$\mathbb{U}_m$	set of all substreams assigned to subcarrier m
P_m	number of substreams in subcarrier m
$\lambda(m, p)$	SINR for the pth substream on subcarrier m

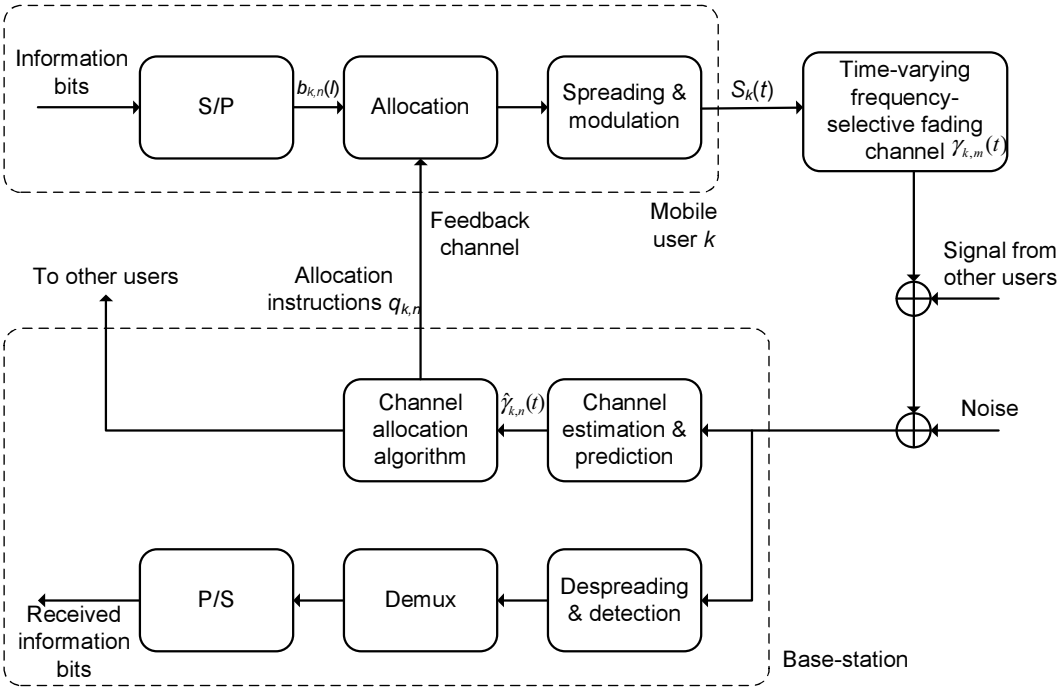

Figure 2.1: System diagram of MC-CDMA with AFH for reverse link

To assess realistic system performance, we employ correlated subcarriers. Assuming the propagation delay is exponentially distributed with rms delay spread σ_d [44, p. 50], the cross-correlation between $\gamma_{k,m}(t)$ and $\gamma_{k,m'}(t)$ with index difference $\Delta m = m - m'$ is given by [45].

$$r_f(\Delta m \Delta f) \triangleq \mathbb{E}\left[\gamma_{k,m}(t)\gamma^*_{k,m'}(t)\right] = \frac{1 + 2j\pi\Delta m\Delta f\sigma_d}{1 + (2\pi\Delta m\Delta f\sigma_d)^2} \tag{2.3}$$

In the reverse link, the base station accurately estimates the current CSI of all users at each subcarrier by employing pilot signals [46]. However, due to the delay caused by the calculation of allocation variables and feeding the allocation assignments back to mobile users, the CSI used for allocation is different from the actual channel conditions experienced during the transmission. An efficient approach to reliable transmission in the presence of CSI mismatch is to predict future CSI $\gamma_{k,m}(t)$ based on outdated observations using the AR model-based linear prediction (LP) $\hat{\gamma}_{k,m}(t)$ [5, 4]. Since the random variables $\hat{\gamma}(k,m)(t)$ and $\gamma_{k,m}(t)$ are jointly Gaussian, the reliability of prediction is characterized by the subcarrier-

independent cross-correlation $\eta \triangleq \mathbb{E}\left[\gamma_{k,m}(t)\hat{\gamma}^*_{k,m}(t)\right] / \sqrt{\mathbb{E}\left[|\gamma_{k,m}(t)|^2\right]\mathbb{E}\left[|\hat{\gamma}_{k,m}(t)|^2\right]}$. The normalized prediction mean square error (NPMSE) is given by $1-\eta^2$ [16]. For example, η=0.925, 0.95, 0.975 and 1.0 correspond to the NPMSE=0.144, 0.098, 0.049, and 0, i.e., poor, degraded, reliable and perfect prediction, respectively [4, 16]. Implementation of reliable practical prediction algorithm for MC-CDMA with AFH is outside the scope of this dissertation. To evaluate performance for prediction accuracy specified by the reliability parameter in simulations, we generate predicted channel coefficients as $\hat{\gamma}_{k,m}(t) = \eta^2\gamma_{k,m}(t) + \omega(t)$, where $\omega(t)$ is white Gaussian noise with variance $\eta^2(1-\eta^2)$ that is independent of $\gamma_{k,m}(t)$.

2.2.3 The Receiver

At the base station, the low-pass equivalent received signal is

$$r(t) = \sum_{k=1}^{K}\sum_{n=1}^{N} \alpha_{k,q_{k,n}} \exp\{\varphi_{k,n}(t) - 2\pi f_{q_{k,n}} t\} + v(t) \tag{2.4}$$

where $v(t)$ is the complex additive white Gaussian noise with power spectral density N_0, τ_k is the timing offset of the kth user, and $\varphi_{k,n}(t) = 2\pi f_{q_{k,n}}\tau_k + \phi_{k,q_{k,n}}(t)$. In this dissertation, we assume perfect knowledge of the timing and frequency offsets for all users, and perfect CSI at the receiver. As discussed in [35], we adopt the quasi-synchronous assumption that is suitable for the reverse link in practice, i.e., the timing of all users is aligned within a small synchronization window of one to a few chips in length.

Without loss of generality, we focus on detection of the symbol $b_{k,n}(l)$ at the output of the correlator at the receiver and drop the symbol index l. Denote $\gamma_{k,m} \triangleq \gamma_{k,m}(t)$, $\alpha_{k,m} \triangleq \alpha_{k,m}(t)$, and $\varphi_{k,m} \triangleq \varphi_{k,m}(t)$ for all k and m during this symbol period.

Define $\mathbb{U}_m$ of size P_m as the index set of all substreams allocated to the mth subcarrier, i.e. $\mathbb{U}_m = \{(k,n)|q_{k,n} = m\}$. Without loss of generality, we replace the substream index pair $(k,n) \in \mathbb{U}_m$ with a single index p, and assume the corresponding $\phi_{k,m} = 0$, $\tau_k = 0$, and $\alpha_p = \alpha_{k,m}$. The output of the correlator for the pth substream is given by

[29, 30, 32]

$$Z_p = \tilde{S}_p + \tilde{I}_p + \tilde{N}_p, p \in [1, \ldots, P_m] \tag{2.5}$$

where $\tilde{S}_p = \sqrt{E_b}\alpha_p b_p$ carriers the desired bit information, and $\tilde{I}_p$ is the interference term

$$\tilde{I}_p = \sqrt{E_b} \sum_{p' \in \mathbb{U}_m \& p' \neq p}^{1} \alpha_{p'} b_{p'} \rho_{p',p} \tag{2.6}$$

where $\rho_{p'p}$ is the cross-correlation between the waveforms of corresponding substreams [40]

$$\rho_{(k',n')(k,n)} = e^{j(\varphi_{k',m} - \varphi_{k,m})} \int_0^{T_b} \left[\sum_{i_1=0}^{PG-1} c_{k',n'}(i_1) h(t - i_1 T_c - \tau_{k'}) \right] \cdot \left[\sum_{i_2=0}^{PG-1} c_{k,n}(i_2) h(t - i_2 T_c) \right] dt \tag{2.7}$$

In (2.6), the inter-user interference from adjacent symbols and other subcarriers is negligible [29, 32, 33]. First, under the assumption of quasi-synchronization, the interference from adjacent symbols is only a few chips in duration. For large processing gain, this interference can be ignored. Second, the interference from adjacent subcarriers is suppressed by the filtering in the frequency domain as well as the despreading operation. It can also be omitted. Thus, the interference term in (2.6) is due primarily to the symbols of other users transmitted on the mth subcarrier that start in the same synchronization window as the desired symbol b_p. Finally, the covariance between the zero-mean Gaussian noise terms $\tilde{N}_p$ in (2.5) is $\mathbb{E}(\tilde{N}_p \tilde{N}^*_{p'}) = N_0 \rho_{p',p}$.

2.2.4 SINR analysis

The received signal (2.5) is detected and demultiplexed at the receiver to make decisions (see Figure 2.1). The analytical SINR of the detector is utilized by the allocation method. The SINR $\lambda_(m,p)$ for the pth substream of the mth subcarrier is given by the ratio of the desired signal power to the total power of residual interference and noise at the input to the decision device. The SINR of the MF detector is [29, 40]

$$\lambda_{MF}(m,p) \approx \frac{E_b \alpha_p^2}{\frac{E_b}{PG} \sum_{p'=1}^{P_m} \Delta(p',p) \alpha_{p'}^2 + N_0} \tag{2.8}$$

where

$$\Delta(p',p) \triangleq \Delta\left[(k',n'),(k,n)\right] \triangleq \begin{cases} 1, & \text{if } k' \neq k, \\ 0, & \text{otherwise} \end{cases} \tag{2.9}$$

In (2.8), we assume perfect synchronization, since this assumption results in the worst case system performance [33, 34, 43]. The reason is that the SINR of MF can be computed as [43]:

$$\lambda_{MF}(m,p) \approx \frac{E_b \alpha_p^2}{\beta \frac{E_b}{PG} \sum\limits_{p'=1}^{P_m} \Delta(p',p)\alpha_{p'}^2 + N_0}, \tag{2.10}$$

where $\beta \leq 1$. For asynchronous CDMA channel, we have $\beta = 2/3$ [43].

When the linear decorrelating detector (LDD) is utilized, multiple-access interference (MAI) is completely eliminated in (2.6), so the SINR is given by the SNR [40, p.249]

$$\lambda_{LDD}(m,p) = \frac{E_b \alpha_p^2}{N_0 \left(\boldsymbol{R}^{-1}\right)_{p,p}} \tag{2.11}$$

where the $P_m \times P_m$ cross-correlation matrix $\boldsymbol{R}$ has component $\boldsymbol{R}_{p,p'} = \rho_{p,p'}$ (see (2.7)).

The SINR of the linear minimum mean square error (MMSE) detector can be computed for the pth substream as [40, p.293-298][47]

$$\lambda_{MMSE}(m,p) = \frac{1}{\left[\boldsymbol{I} + \frac{E_b \boldsymbol{A}\boldsymbol{R}\boldsymbol{A}^H}{N_0}\right]^{-1}_{p,p}} - 1 \tag{2.12}$$

where $\boldsymbol{A} = diag\{\alpha_1, \alpha_2, \ldots, \alpha_{P_m}\}$, and $\boldsymbol{I}$ is $k \times k$ identity matrix.

When the successive interference canceller (SIC) is applied to (2.5), we assume without loss of generality that $\alpha_1 \geq \alpha_2 \geq \ldots \geq \alpha_{P_m}$. In the pth stage, the remaining user with the strongest received signal is demodulated as

$$\hat{b}_p = sgn\left(Z_p - \sum_{p'=1}^{p-1} \sqrt{E_b}\alpha_{p'}\rho_{p',p}\hat{b}_{p'}\right) \tag{2.13}$$

where $sgn(\cdot)$ is the sign function. The SINR of the pth substream on the mth subcarrier can be approximated as [40, p.360]

$$\lambda_{SIC}(m,p) \approx E_b\alpha_p^2 / \left[N_0 + \frac{E_b}{PG} \sum_{p'=p+1}^{P_m} \Delta(p',p)\alpha_{p'}^2 + \frac{4E_b}{PG} \sum_{p'=1}^{p-1} \Delta(p',p)\alpha_{p'}^2 P_{e,SIC}(m,p') \right] \tag{2.14}$$

where the BER of the p'th substream is

$$P_{e,SIC}(m,p') \approx Q\left[\sqrt{2\lambda_{SIC}(m,p')}\right], \tag{2.15}$$

$$Q(x) = \int_x^\infty \exp(-t^2/2)dt/\sqrt{2\pi}m \tag{2.16}$$

and $\Delta(p',p)$ is defined in (2.9).

2.3 Allocation Algorithms

In this section, we discuss the limitations of previously proposed WF allocation algorithm and describe a novel allocation method for the reverse link. As discussed in section 2.2 (see Figure 2.1), these algorithms are implemented at the base station, and the resulting allocation assignments are sent back to the mobile, where they are employed to select the reverse link subcarriers for each substream. Thus, the computational load associated with channel allocation is borne entirely by the base station, which can afford much greater complexity than the mobiles. Moreover, the feedback load is low since only a few allocation bits need to be fed back at a low rate on the order of the maximum Doppler shift.

All allocation methods employ the SINR minimization criterion and utilize the SINR expression $\lambda(m,p)$ in (2.8), (2.11), (2.12), or (2.14) that depends on the type of the receiver utilized at the base station. Otherwise, the allocation methods do not depend on the receiver design and can be easily adapted to various receiver choices.

Subcarrier allocation methods were also addressed in [48, 49, 50, 51, 52]. However, these papers focus on the orthogonal frequency-division multiple access (OFDMA) system,

and the throughput and fairness among users are primary concerns, since the target application is the internet protocol (IP)-based packet transmission system. In contrast, we consider MC-CDMA with AFH that has fixed data rate for all users in the system, which is suitable for such applications as voice and circuit-switched data transmission. Thus, it is reasonable to use the minimum SINR as performance measure to guarantee the quality of service for all users. Moreover, since the multi-access interference (MAI) is not significant in OFDMA, design of the allocation algorithm is simpler for this system than for MC-CDMA.

2.3.1 The Waterfilling Algorithm

The WF algorithm was proposed in [29] for the MF receiver. Note that this method is not the water-filling solution that achieves the information-theoretic capacity, although its design was inspired by the latter. The WF algorithm is an iterative allocation algorithm, i.e., one substream is allocated in each iteration. The sequence of KN iterations is divided into N consecutive groups, with K iterations per group. In each group, one substream per user is allocated. During each iteration of the nth group, all users whose substreams have not yet been allocated in this group select the subcarrier with the highest SINR, and the user that has the lowest selected SINR level is assigned to that subcarrier [29]. The protection of weak users offered by the order of subcarrier allocation in the WF method is limited due to two reasons. First, weak users already assigned to given subcarrier cannot contribute large interference level that would prevent allocation of a much stronger user's substream to this subcarrier. Second, the WF algorithm does not take into account the MAI impact of assigning a new substream on the substreams already allocated to certain subcarrier. As a result, the BER of the WF allocation algorithm is very high for some realizations of channel fading coefficients. This case is demonstrated in the following example.

Example: Consider a system with $K = N = M = 2$, $PG = 16$, $E_b = 1$, $N_0 = 0.01$ and $\eta = 1.0$. Suppose fading amplitudes are represented by $\{\alpha_{1,1}^2 = 0.1, \alpha_{1,2}^2 = 0.09, \alpha_{2,1}^2 = 1, \alpha_{2,2}^2 = 0.1\}$.

The WF algorithm [29] performs the allocation in four iterations. The resulting

allocation is $\{q_{1,1}=1, q_{1,2}=2, q_{2,1}=1, q_{2,2}=1\}$. Suppose that substream $(k=1, n=1)$ corresponds to substream $p=1$ of the first subcarrier. From (2.8), the BER of this substream is approximated as $P_{e,MF}(m=q_{1,1}=1, p=1) \approx Q(\sqrt{\frac{2\times 0.1}{0.01+2/16}}) \approx 0.11$.

A better allocation solution is to assign the substreams of the first user to the first subcarrier and the substreams of the second user to the second subcarrier, i. e., $\{q_{1,1}=1, q_{1,2}=1, q_{2,1}=2, q_{2,2}=2\}$. The resulting BERs are $P_{e,MF}(m,p) \approx Q(\sqrt{2\times 0.1/0.01}) \approx 3.8\times 10^{-6}$ for $m,p \in \{1,2\}$.

This example illustrates that the WF algorithm has poor performance when the instantaneous fading amplitude of one user (user 2 in this example) is much larger than that of the other user. While such events are unlikely, they dominate the average BER in moderate to high SNR region. Therefore, it is desirable to design an allocation algorithm that overcomes the limitations of the WF method.

2.3.2 Proposed Allocation Algorithm

Our allocation method has the following optimization criterion. As in [29], we focus on the performance of the substream with the lowest SINR since the error events associated with this substream dominate the error rate. The optimization objective is to maximize the SINR of the allocated substream with the lowest SINR, i.e., to find the set of allocation variables that

$$\mathbb{Q}_o = \arg\max_{\mathbb{Q}} \left\{ \min_{m\in[1,\ldots,M], p\in[1,\ldots,P_m]} \lambda(m,p) \right\} \tag{2.17}$$

where $\mathbb{Q}=\{q_{k,n}|k\in[1,\ldots,K], n\in[1,\ldots,N]\}$ is the set of all possible allocation variables, and $\lambda(m,p)$ is the SINR calculated from (2.8), (2.11), (2.12), or (2.14), depending on the type of the detector employed at the receiver. In (2.17), SINRs of all substreams are used for allocation, so the weak user is protected well. Thus, better performance is expected relative to the WF algorithm.

Theoretically, the search over the elements of $\mathbb{Q}$ produces the optimal solution for (2.17). To find out the number of possible solutions, we first consider the number of ways

in which N identical substreams may be distributed among M different subcarriers. This is the same as the number of integer vectors of length M that satisfy the constraints

$$[n_1, n_2, \ldots, n_M]^T \text{ with } 0 \leq n_m \leq N \text{ and } \sum_{m=1}^{M} n_m = N \tag{2.18}$$

where n_m is the number of substreams assigned to the mth subcarrier for one user. The number of ways is given by $(N + M - 1)!/[(M - 1)!N!]$. Since we have K users in the system, there are $\{(N + M - 1)!/[(M - 1)!N!]\}^K$ possible ways to allocate N equivalent substreams/user into M distinct subcarriers. Thus, the computational complexity of finding the exact solution to (2.17) is very high, and a suboptimal method with moderate complexity is desirable.

Inspired by the iterative algorithms in [29, 39, 48, 49], we design an iterative allocation method to find a suboptimal solution for (2.17). In this algorithm, one substream is assigned at each iteration, and all substreams are allocated after KN iterations. For simplicity, the substreams are assigned consecutively, i.e. the substream (k, n) is allocated at the $[K(n - 1) + k]$th iteration. The algorithm is based on the following idea. Suppose the substream (k, n) is allocated to the subcarrier m. We observe that in this case only the substream (k, n) and the substreams previously assigned to this subcarrier experience the SINR degradation. Denote the set of such substreams $\mathbb{U}'_m$. For each $m \in [1, \ldots, M]$, we determine the lowest SINR level in $\mathbb{U}'_m$ assuming that the substream (k, n) is allocated to subcarrier m. Then find the subcarrier m_o that produces the maximum value of this lowest SINR among all M values and allocate the substream (k, n) to subcarrier m_o. In our allocation process, the substreams are allocated consecutively, and the interference from a subset of all substreams is taken into account for each allocation. Therefore, it results in a suboptimal solution to (2.17). However, it improves upon the WF method in [29] since it protects previously allocated weaker users. The proposed improved allocation algorithm consists of the steps in Table 2.2.

In Table 2.2, the substreams are assigned consecutively, i.e. the substream (k, n) is allocated at the $[K(n - 1) + k]$th iteration. Here we consider a more sophisticated

Table 2.2: Improved Allocation Algorithm

Initialize $P_m = 0$ and $\mathbb{U}_m = \{\varnothing\}$ for all $m \in [1, \ldots, M]$,.

for $n = 1$ to N

for $k = 1$ to K

S1) Augment $\mathbb{U}'_m = \{\mathbb{U}_m, (k, n)\}$ for $m \in [1, \ldots, M]$. Let $\lambda(m, p)$ be the SINR of the pth substream ($p \in [1, \ldots, P_m+1]$) assuming that substream (k, n) is assigned to the mth subcarrier.

S2) Find m_o that satisfies

$$m_o = \arg \max_{m \in [1,\ldots,M]} \left\{ \min_{p \in [1,\ldots,P_m+1]} \lambda(m, p) \right\}$$

S3) Assign substream (k, n) to the m_oth subcarrier, i.e., set $q_{k,n} = m_o$. Then update $P_{m_o} = P_{m_o} + 1$, and $\mathbb{U}_{m_o} = \mathbb{U}'_{m_o}$.

Table 2.3: Allocation Algorithm with Ordering

Initialize $P_m = 0$ and $\mathbb{U}_m = \{\varnothing\}$ for all $m \in [1, \ldots, M]$,.

for $n = 1$ to N

S1) Initialize set $\mathbb{K} = \{1, 2, \ldots, K\}$

S2) Augment $\mathbb{U}'_m = \{\mathbb{U}_m, (k, n)\}$ for $m \in [1, \ldots, M]$, and $k \in \mathbb{K}$. Let $\lambda(k, m, p)$ be the SINR of the pth substream ($p \in [1, \ldots, P_m+1]$) assuming that substream (k, n) is assigned to the mth subcarrier.

S3) Find $\lambda_o(k)$ and $m_o(k)$ that satisfies

$$\lambda_o(k) = \max_{m \in [1,\ldots,M]} \left\{ \min_{p \in [1,\ldots,P_m+1]} \lambda(k, m, p) \right\}, k \in \mathbb{K} \tag{2.19}$$

$$m_o(k) = \arg \max_{m \in [1,\ldots,M]} \left\{ \min_{p \in [1,\ldots,P_m+1]} \lambda(k, m, p) \right\}, k \in \mathbb{K}$$

S4) Find $k_o \in \mathbb{K}$ that $k_o = \arg \max_{k' \in \mathbb{K}} \lambda_o(k')$

S5) Assign substream (k_o, n) to the $m_o(k)$th subcarrier, i.e., set $q_{k_o,n} = m_o(k)$. Then update $P_{m_o(k)} = P_{m_o(k)} + 1$, and $\mathbb{U}_{m_o(k)} = \mathbb{U}'_{m_o(k)}$. Remove k_o from $\mathbb{K}$.

S6) Repeat steps S2)-S5) until $\mathbb{K}$ is empty.

allocation method. In this algorithm, we find the minimum SINR among all subcarriers if we allocate one substream from the kth user into each subcarrier. Then the user that causes the maximum minimum SINR is permitted to assign one of its substreams into its favorite subchannel as in WF algorithm. The resulting algorithm is shown as in Table 2.3,

To compare the performance of the proposed algorithm and the algorithm with ordering in Table 2.3, we consider a system with $K = 16$ users, $N = 8$ substreams/uers and $PG = 64$. The number of subcarriers M is 4 or 8, which corresponds to moderate and heavy system loads, respectively. When LDD is used at the receiver, the simulated BERs are shown in Figure 2.2. We observe that these two algorithms have similar average BER performance at all SNR values. The simple proposed algorithm even outperforms the algorithm with ordering at high SNR. The reason is that allocating the user with the worst favorite channel first deteriorates the BERs of other users so the average BER over all users is limited. In addition to this figure, we also simulated different system parameter sets with moderate to heavy system load (not shown in this dissertation). Those simulation results show that these two algorithms have similar BER performance.

2.3.3 Imperfect CSI

When perfect CSI is available at the base station, the SINR in step S1 in the proposed allocation algorithm of the improved allocation algorithm is calculated using the expression (2.8), (2.11), (2.12), or (2.14), depending on the type of the detector employed at the receiver. As discussed earlier, this perfect knowledge of CSI assumed in the calculation of $\lambda(m, p)$ is usually unavailable. Instead, one can design an allocation algorithm based on the average BER conditioned on the predicted CSI as

$$\bar{P}_e(m,p) = \int_{-\infty}^{\infty}\int_{-\infty}^{\infty} Q[\sqrt{\lambda(m,p)}]p(\alpha_1,\ldots,\alpha_{P_m}|\hat{\alpha}_1,\ldots,\hat{\alpha}_{P_m})d\alpha_1\ldots\alpha_{P_m} \tag{2.20}$$

where $\hat{\alpha}_p = |\hat{\gamma}_p|$, and $p(\alpha_1,\ldots,\alpha_{P_m}|\hat{\alpha}_1,\ldots,\hat{\alpha}_{P_m})$ is the joint conditional probability density function of perfect CSI given predicted CSI. However, the evaluation of (2.20) is very complex for a large number of substreams. For simplicity, we focus on a simpler approach

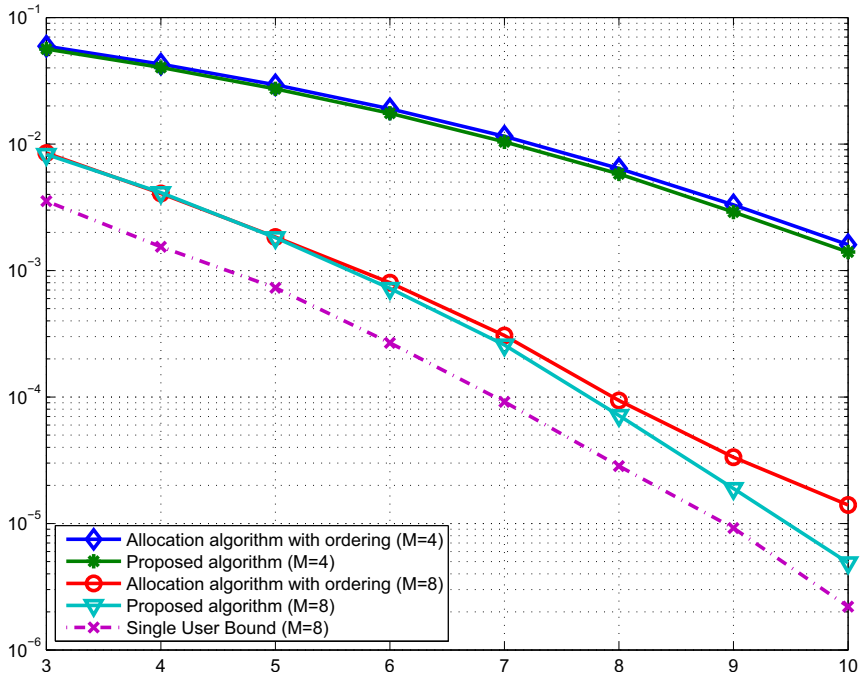

Figure 2.2: BER of proposed allocation algorithm and the algorithm with ordering for $K = 16$ users, M =4 or 8 subcarriers, $N = 8$ substreams/uers and $PG = 64$.

that employs the predicted fading amplitude $\hat{\alpha}_p$ instead of α_p in the SINR $\lambda(m,p)$ and obtains the SINR estimate $\hat{\lambda}(m,p)$. Thus, the predicted CSI is treated as if it was perfect, and $\hat{\lambda}(m,p)$ is used as performance measure in step S1 of our allocation method. The sensitivity of allocation algorithm to the prediction errors is tested using simulations in section 2.4.

2.3.4 Complexity Reduction

In our allocation algorithm, the computational complexity is mainly determined by the calculation of the SINR. For MF and SIC receivers, the calculation of the SINR given by (2.8) and (2.14), respectively, involves only simple scalar operations. On the other hand, the allocation algorithms for the LDD or MMSE detector are complex due to the matrix inversion in (2.11) and (2.12), which has to be performed for every $\mathbb{U}'_m$ in step S1 of the improved allocation algorithm. However, it is possible to reduce complexity by recursive computation of this inverse as discussed below for the case of the LDD at the receiver.

In this recursion, for each m in step S1, denote the $P_m \times P_m$ cross-correlation matrix of the substreams previously assigned to subcarrier m as $\boldsymbol{R}(P_m)$. The inverse of this matrix $[\boldsymbol{R}(P_m)]^{-1}$ has been computed during an earlier iteration. In the current iteration, we need to evaluate the SNR $\lambda_{LDD}(m,p)$, $p \in [1,\ldots,P_m+1]$ when assignment of new (P_m+1)st substream is examined for subcarrier m in step S1. This computation requires the inversion of an augmented correlation matrix

$$\boldsymbol{R}(P_m+1) = \begin{bmatrix} \boldsymbol{R}(P_m) & \boldsymbol{\rho} \\ \boldsymbol{\rho}^H & 1 \end{bmatrix} \tag{2.21}$$

where $\boldsymbol{\rho} = [\rho_{P_m+1,1}, \rho_{P_m+1,2}, \ldots, \rho_{P_m+1,P_m}]^T$ is the vector of the cross-correlation coefficients between the new substream and P_m existing substreams determined by (2.7). The inverse of (2.21) can be computed by exploiting the existing $[\boldsymbol{R}(P_m)]^{-1}$ as follows [53, eq. (35)]:

$$[\boldsymbol{R}(P_m+1)]^{-1} = \begin{bmatrix} [\boldsymbol{R}(P_m)]^{-1} + u\,[\boldsymbol{R}(P_m)]^{-1}\boldsymbol{\rho}\boldsymbol{\rho}^H[\boldsymbol{R}(P_m)]^{-1} & -u\,[\boldsymbol{R}(P_m)]^{-1}\boldsymbol{\rho} \\ -u\boldsymbol{\rho}^H[\boldsymbol{R}(P_m)]^{-1} & u \end{bmatrix} \tag{2.22}$$

where $u = \left[1 - \boldsymbol{\rho}^H[\boldsymbol{R}(P_m)]^{-1}\boldsymbol{\rho}\right]^{-1}$.

To calculate this recursion (2.22), first we need to perform $[\boldsymbol{R}(P_m)]^{-1}\boldsymbol{\rho}$, which requires P_m^2 multiplications. The vector multiplication $[\boldsymbol{R}(P_m)]^{-1}\boldsymbol{\rho}\boldsymbol{\rho}^H[\boldsymbol{R}(P_m)]^{-1}$ would normally consume P_m^2 multiplications. However, since the resulting matrix is Hermitian, we only need to calculate approximately half of the entries in the matrix. For all other operations in (2.22), the order of complexity is less than P_m.

Therefore, this recursion requires about $1.5(P_m+1)^2$ complex multiplications and divisions, which is significantly less than the $(P_m+1)^{log_2 7}$ operations of efficient Strassen's method for direct matrix inversion [54].

The SINR calculation for MMSE detector (2.12) can be simplified similarly. Here, we define

$$\boldsymbol{F}(P_m) \triangleq \boldsymbol{I}(P_m) + \frac{E_b}{N_0}\boldsymbol{A}(P_m)\boldsymbol{R}(P_m)\boldsymbol{A}^H(P_m) \tag{2.23}$$

where $\boldsymbol{I}(P_m)$ is the $P_m \times P_m$ identity matrix and $\boldsymbol{A}(P_m) = diag\{\alpha_1,\ldots,\alpha_{P_m}\}$. Using this

Table 2.4: Computational complexity of allocation algorithms (for $KN \gg M$ case)

Allocation algorithm	Order of complexity
WF with MF receiver	$O(K^2N)$
Proposed algorithm for MF receiver	$O(K^2N^2)$
Proposed algorithm for LDD	$O(K^3N^3)$
Proposed algorithm for SIC	$O(K^3N^3)$

definition, the recursion can be written as

$$[\boldsymbol{F}(P_m+1)]^{-1} = \begin{bmatrix} [\boldsymbol{F}(P_m)]^{-1} + u\,[\boldsymbol{F}(P_m)]^{-1}\,\boldsymbol{f}\boldsymbol{f}^H\,[\boldsymbol{F}(P_m)]^{-1} & -u\,[\boldsymbol{F}(P_m)]^{-1}\,\boldsymbol{f} \\ -u\boldsymbol{\rho}^H\,[\boldsymbol{F}(P_m)]^{-1} & u \end{bmatrix} \quad (2.24)$$

where $u = \left[1 - \boldsymbol{f}^H[\boldsymbol{R}(P_m)]^{-1}\boldsymbol{f}\right]^{-1}$, and $\boldsymbol{f} = \{\boldsymbol{F}_{1,1}, \ldots, \boldsymbol{F}_{P_m,1}\}^T$.

Using the recursion (2.22), we show the number of operations required to allocate all KN substreams in Table 2.4 (see Appendix A). Our allocation algorithm outperforms the WF algorithm at the price of increased complexity. The utilization of MUDs results in the allocation algorithm complexity increase relative to the MF receiver. Note that although SIC is much simpler than the LDD, their allocation algorithms have the same order of complexity.

2.4 Numerical Results

First, we compare the average BER (over all users and fading realizations) of the WF algorithm, the optimal allocation method (2.17) and the proposed algorithm for the MF detector in Figure 2.3. As in [29], the assumptions of perfect CSI knowledge and independent fading subcarriers are adopted in this simulation, as well as in Figure 2.4-2.6. Due to very high complexity of the optimal allocation, small number of substreams is employed in this comparison. We observe that the proposed algorithm incurs a small penalty relative to the optimal allocation method for high SNR and outperforms the latter for low SNR since the average BER is not the optimality criterion. As expected, the WF

algorithm has the worst performance among the three allocation algorithms in moderate to high SNR. Figure 2.3 also demonstrates that the AFH system with the proposed allocation algorithm provides 2-3dB power gain over the non-adaptive MC DS-CDMA with MRC [32] in this multiuser scenario.

Figure 2.4 compares the average BER of the WF method and the proposed allocation algorithm for the MF receiver and a larger number of users in the system. We observe that the performance gain of the proposed algorithm over the WF method increases as the SNR grows. The comparison in Figure 2.4 corroborates our discussion on the limitations of the WF algorithm in section 2.3.

In principle, the WF algorithm can also be employed with LDD. The only change made to the original WF algorithm is to replace the SINR analysis of MF (2.8) with that of LDD (2.11). Figure 2.5 shows that the WF algorithm has significant performance loss compared with the proposed algorithm when LDD is employed for both algorithms.

Figure 2.6 shows the average BER of the proposed allocation algorithm for moderate system load (K comparable to M) combined with receivers discussed in section 2.2. To illustrate the potential of combined subcarrier allocation and MUD, the single user bound (SUB), i.e., the BER of the system with only one user, is included in the figure. The linear methods (the MMSE detector and LDD) have much better performance than the SIC and the MF detectors for moderate to high SNR. The linear detectors approach the SUB in this system because the adaptive allocation algorithm separates the substreams with high cross-correlations into different subcarriers. This adaptive allocation policy also reduces the effect of noise enhancement that degrades LDD in conventional CDMA channels, so it is only slightly outperformed by the MMSE detector in our system. We also note that when the allocation method is employed with the SIC, it is impaired in the first few stages by the inaccuracy of the SINR approximation (2.14) when the number of substreams is small [40].

We investigate the effect of imperfect CSI in Figure 2.7. Observe that while the BER of the adaptive system with LDD increases as the reliability of CSI degrades, it is still smaller than the SUB of non-adaptive MC DS-CDMA even for $\eta = 0.95$, which is easily

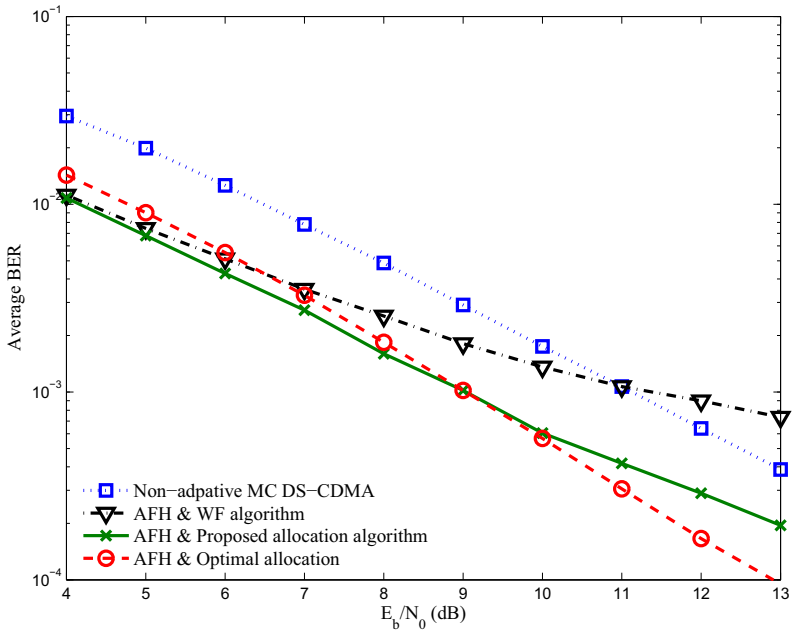

Figure 2.3: BER performance of adaptive MC-CDMA with WF, optimal and proposed allocation algorithms ($N = 1$ substream/user, $PG = 64$ and perfect CSI knowledge), and non-adaptive MC DS-CDMA with MRC (time domain processing gain $PG = 64$). For both systems, $K = 6$ users, $M = 4$ subcarriers, independent fading subcarriers ($\Delta f \sigma_d = \infty$), and MF receiver are assumed.

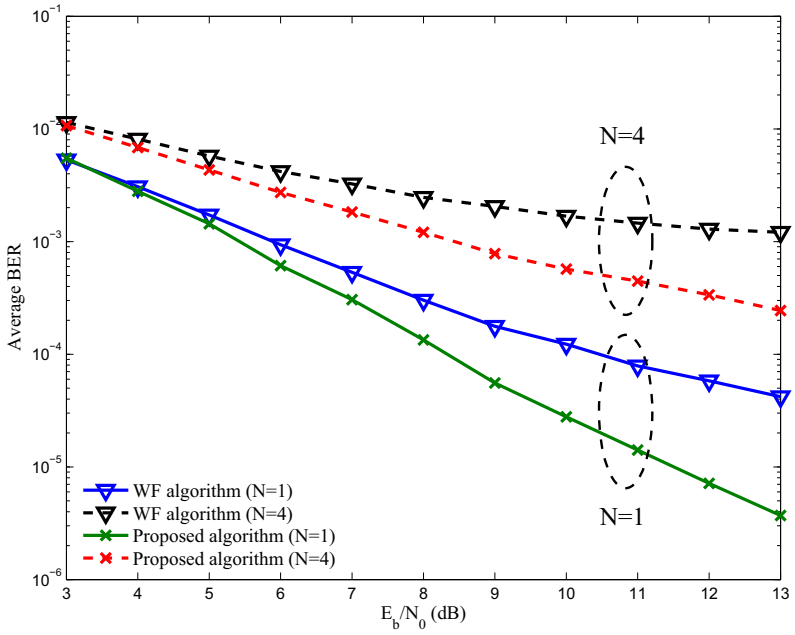

Figure 2.4: BER performance of adaptive MC-CDMA with MF receiver for $K = 16$, $M = 8$, $PG = 64$, $\Delta f \sigma_d = \infty$, and $\eta = 1.0$

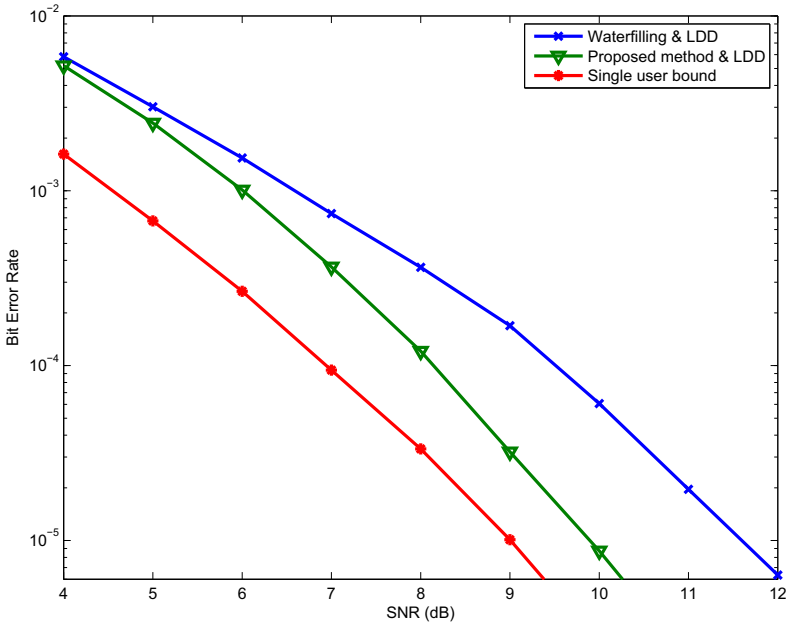

Figure 2.5: BER performance of adaptive MC-CDMA with LDD receiver for $K = 16$, $M = 8$,$N = 4$ substreams/user, $PG = 64$, $\Delta f \sigma_d = \infty$, and $\eta = 1.0$

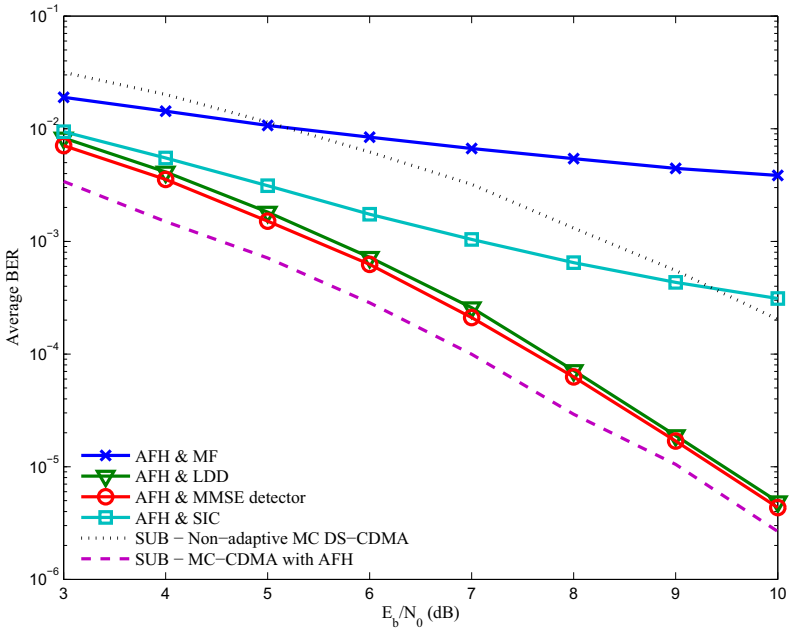

Figure 2.6: BER performance of MC-CDMA with AFH for $K = 16$, $N = 8$, and $\eta = 1.0$. In all systems, $M = 8$, $PG = 64$, and $\Delta f \sigma_d = \infty$

achievable in realistic scenarios [15, 4].

Figure 2.8 illustrates the impact of correlated subcarriers on the BER of the adaptive system when perfect knowledge of the CSI is assumed. As expected, the performance degrades as $\Delta f\sigma_d$ decreases. However, for $\Delta f\sigma_d$ as small as 0.3, the performance is very close to the case of independent fading subcarriers ($\Delta f\sigma_d = \infty$). Observe that the BER gap between the LDD and SIC narrows as $\Delta f\sigma_d$ decreases in Figure 2.8 since fading, not MAI, becomes the dominant source of performance degradation as diversity reduces for small $\Delta f\sigma_d$. Similarly, it is shown in [33] that performance gap between these two detectors narrows when the predicted CSI is unreliable in the adaptive system. The complexity comparison in [33] reveals that the allocation algorithms for SIC and linear detectors have similar complexity. Therefore, the LDD or MMSE detectors provide the best complexity/performance/robustness trade-off in this adaptive system.

In Figure 2.9 and 2.10, we investigate a practical system design with the available bandwidth set to 1.25MHz, the bandwidth of single carrier in IS-95 and CDMA2000 standard. The rms delay spread of the channel is assumed σ_d=1 us, which is typical for the urban environment [43, p. 200]. Since the coherence bandwidth is approximately $1/5\sigma_d$=200KHz [43, p. 202], we divide the available bandwidth into 12 subcarriers with the subcarrier bandwidth of 102.4 KHz to assure flat fading for each subcarrier. Assuming $N = 8$ substreams and $PG = 64$, the system supports a 12.8 Kbps data service to each user. Moreover, for comparison, we have simulated a non-adaptive MC DS-CDMA system with the same system bandwidth, number of subcarriers, and data rate as for the adaptive system. To maintain the data rate, the time-domain processing gain of eight is required in the latter system. While in the original MC DS-CDMA design, the same spreading code was used for all subcarriers of one user [32], we employ different random spreading codes for different subcarriers as proposed in [41] to reduce the variance of the cross-correlation between the waveforms of different users.

Figure 2.9 shows the BER of the adaptive system for varying numbers of users. For all detectors, the BER level is maintained provided the number of users K is sufficiently

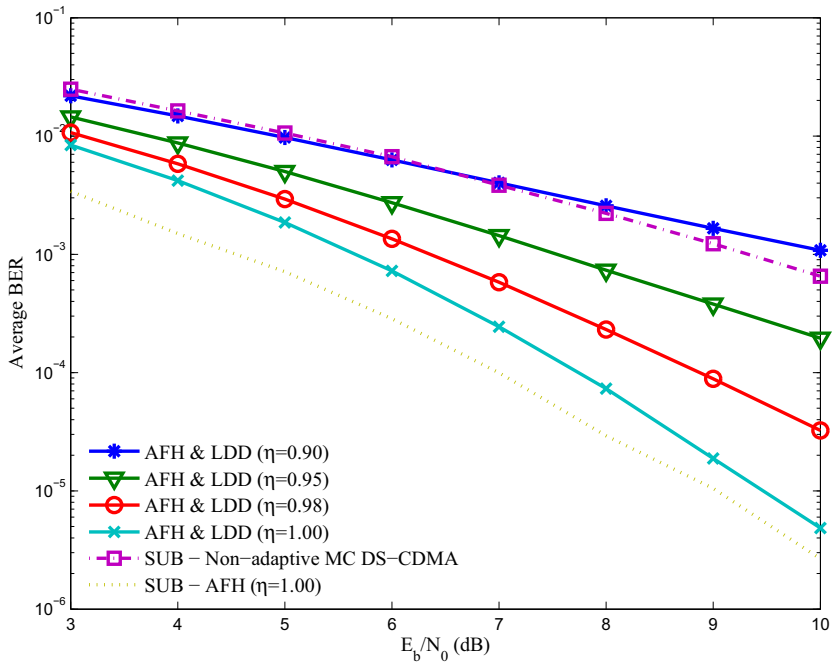

Figure 2.7: Comparison of SUB of non-adaptive MC DS-CDMA with the BER of MC-CDMA with AFH and LDD for $K = 16$, $N = 8$, and varying CSI reliability η. In all systems, $PG = 64$, $M = 8$, and $\Delta f \sigma_d = \infty$.

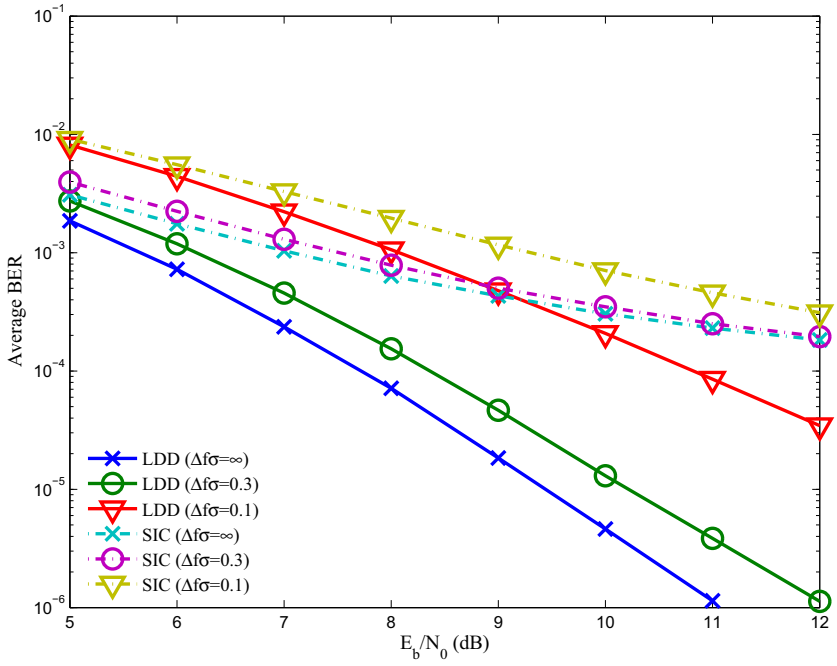

Figure 2.8: BER vs. number of users in the adaptive system with improved allocation algorithm for SNR=10dB, $M = 12$, $N = 8$, $PG = 64$, $\eta = 0.95$, and $\Delta f \sigma_d = 0.1024$

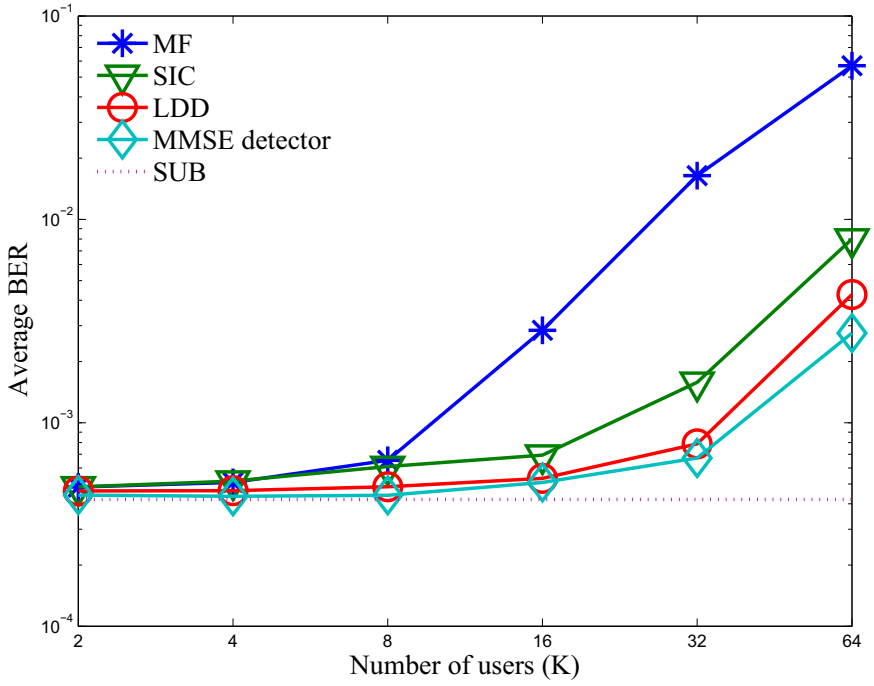

Figure 2.9: BER vs. number of users in the adaptive system with improved allocation algorithm for SNR=10 dB, $M = 12$, $N = 8$, $PG = 64$, $\eta = 0.95$, and $\Delta f \sigma_d = 0.1024$

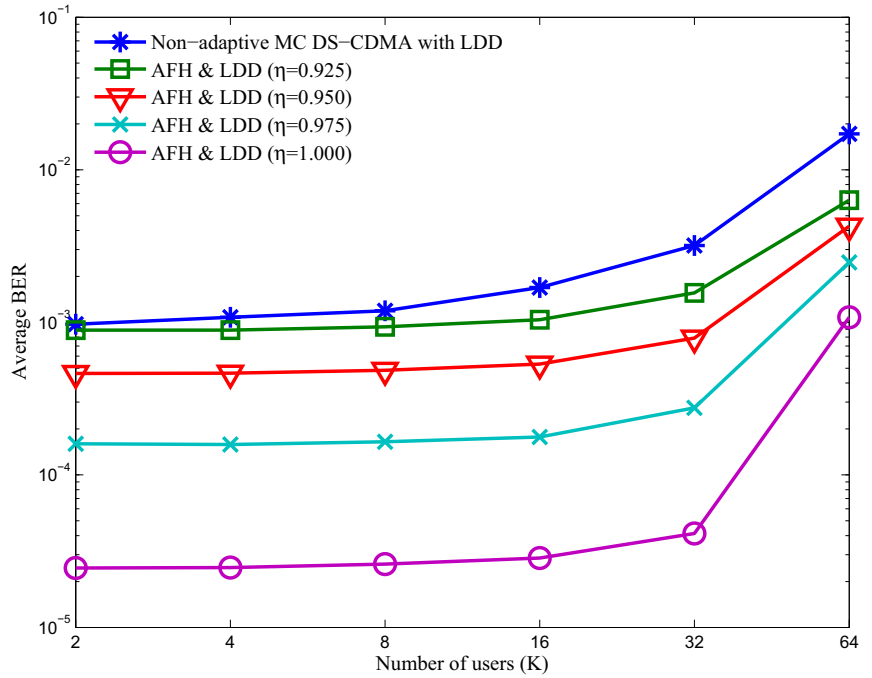

Figure 2.10: BER vs. number of users in the system with LDD for SNR=10dB, $M = 12$, $N = 8$, $PG = 64$, and $\Delta f \sigma_d = 0.1024$.

small. This is due to the fact that the fading induced near-far problem can be easily suppressed for a small number of users. While the BER of the MF receiver degrades for $K \geq M$, the MUDs maintain reliable performance unless the system load is very large, i. e., when $K \gg M$. The MMSE detector has the best performance, but its gain over the LDD is very small as discussed above.

In Figure 2.10, the BERs of the adaptive and non-adaptive systems with the LDD are compared. For the non-adaptive system, this MUD is derived from the RAKE LDD designed for the multipath fading channel in [55]. Even with poorly predicted CSI ($\eta = 0.925$), the AFH system outperforms the non-adaptive system. For target BER of 10^{-3}, the adaptive system can support from 12 to 63 users, depending on the quality of the predicted CSI, while only two users are feasible for the non-adaptive system.

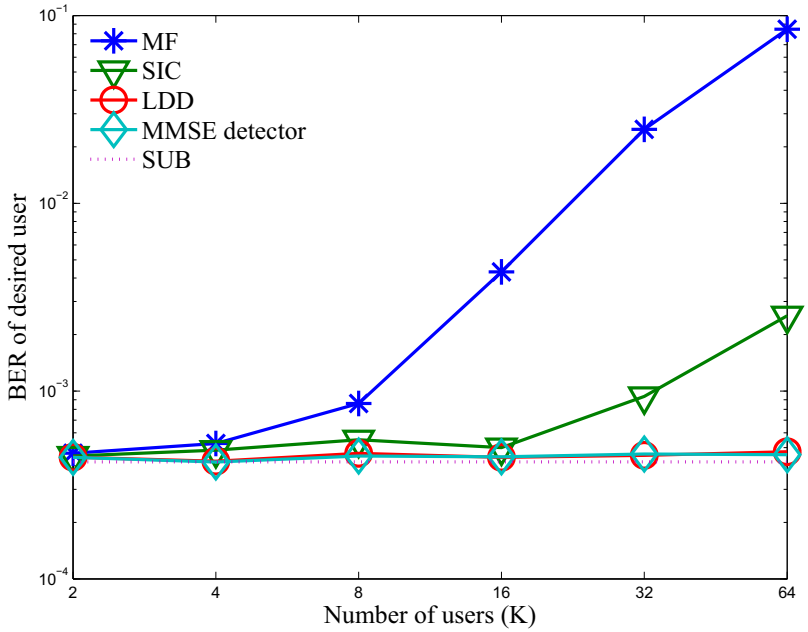

Figure 2.11: BER vs. number of users in the adaptive system with imperfect power control for $M = 12$, $N = 8$, $PG = 64$, $\eta = 0.95$, and $\Delta f \sigma_d = 0.1024$. The SNR is 10 dB for desired user and 20 dB for other users.

In previous simulations, the power control that adapts perfectly to large-scale fading is assumed, i.e., E_b is the same for all users. To investigate the effect of the near-

far problem caused by imperfect power control on the proposed allocation algorithm, the SNR of randomly chosen desired user is set to 10 dB, while $K-1$ interfering users have SNR=20 dB. Given the same system parameters as in Figure 2.9, the simulated BER of the desired user is shown in Figure 2.11. Note that MUDs in this figure have lower BER than for the perfect power control case in Figure 2.9, and the BERs of linear detectors are very close to the system SUB even for heavily loaded near-far scenario. The reason is that the weakest user's substreams are assigned into their favorite subcarriers by our allocation algorithm, while the interfering stronger users are competing for remaining subcarriers. In previous figures, our allocation policy was shown to alleviate small-scale fading-induced near-far problem. Figure 2.11 demonstrates that combined proposed allocation algorithm and MUD are also very effective in compensating for large-scale fading and imperfect power control.

2.5 Conclusions

A novel allocation algorithm that outperforms the WF algorithm for MC-CDMA system with AFH for the reverse link was proposed. The proposed allocation algorithm is combined with MUDs using the SINR analysis. It is demonstrated that combined improved subcarrier allocation and MUD is very effective in mitigating MAI, resulting in much larger system capacity than for the non-adaptive MC DS-CDMA system. This conclusion is confirmed for realistic rapidly varying fading channels with correlated subcarriers, CSI mismatch, and imperfect power control.

Chapter 3

Data-Aided Noise Reduction for Long-Range Fading Prediction in Adaptive Modulation Systems

3.1 Introducton

Adaptive modulation (AM) has been investigated extensively due to its effectiveness and simplicity [21]. The UAM schemes that employ MQAM were studied in [21, 56]. To improve the SE, the ACM methods, also known as ATCM, were proposed [22, 24, 25, 23, 57]. The SE of AM schemes decreases as the accuracy of the CSI degrades at the transmitter [56, 23, 58]. Moreover, the ACM achieves significant coding gain over the UAM for reliable CSI [22], but the coding gain diminishes when the CSI accuracy degrades, and UAM outperforms ACM when CSI is unreliable [23, 57].

To ensure high SE for AM systems and to achieve the coding gain in realistic time-varying fading channels, the CSI needs to be predicted to compensate for the feedback and data processing delay and system constraints. Several fading prediction methods have been proposed to enable mobile radio adaptive transmission methods [5, 4]. In this dissertation, we focus on the AR model-based linear prediction (LP), referred to as the LRP method,

which was shown to achieve superior performance for realistic channel models and measured channels [5, 4, 14]. The LRP method has low MSE at spatial prediction ranges over one carrier wavelength when the SNR of the observations is sufficiently high [5]. However, its performance degrades severely at low and medium SNR. Utilization of highly oversampled pilots in NR prior to LP was proposed in [7, 15]. These NR techniques, referred to as the high-rate pilot methods, improve the prediction accuracy for practical SNR over the low-rate raw pilot prediction algorithm, which relies only on the pilot symbols necessary for noiseless fading coefficient prediction [11]. Fading prediction aided by the high-rate pilot method was utilized in AM systems in [15, 24, 23, 56]. However, the resources consumed by transmitting pilots were not considered in these investigations. In this dissertation, we demonstrate that the high-rate pilot method consumes excessive system bandwidth due to transmitting oversampled pilots, so the overall SE does not increase significantly despite better prediction accuracy. Although the rate and power of raw pilots are optimized to maximize the SE under given power constraint in [58], the pilots still consume a large portion of the available bandwidth in that method.

We propose to exploit the data symbols in NR to achieve high accuracy of prediction without significantly increasing the pilot rate and power, thereby improving the SE [16]. The data-aided methods have been widely used for channel equalization [59], estimation, and tracking [60]. In [61], decision-directed short-range prediction of fading channels was investigated, and in [5, 62], data-aided NR was employed in LRP to enable adaptive channel inversion. However, these decision-directed methods are not applicable to the adaptive modulation systems directly.

In this dissertation and [16, 17], a novel DANR method is proposed for the LRP-aided AM systems. This method comprises an adaptive pilot transmission mechanism that compensates for outages, robust noise reduction and decision-directed channel estimation. The prediction accuracy and SE of the proposed method are compared with those of the high-rate pilot and raw pilot methods, and the advantages of the DANR approach are demonstrated for practical SNR and prediction ranges. In addition to taking into account

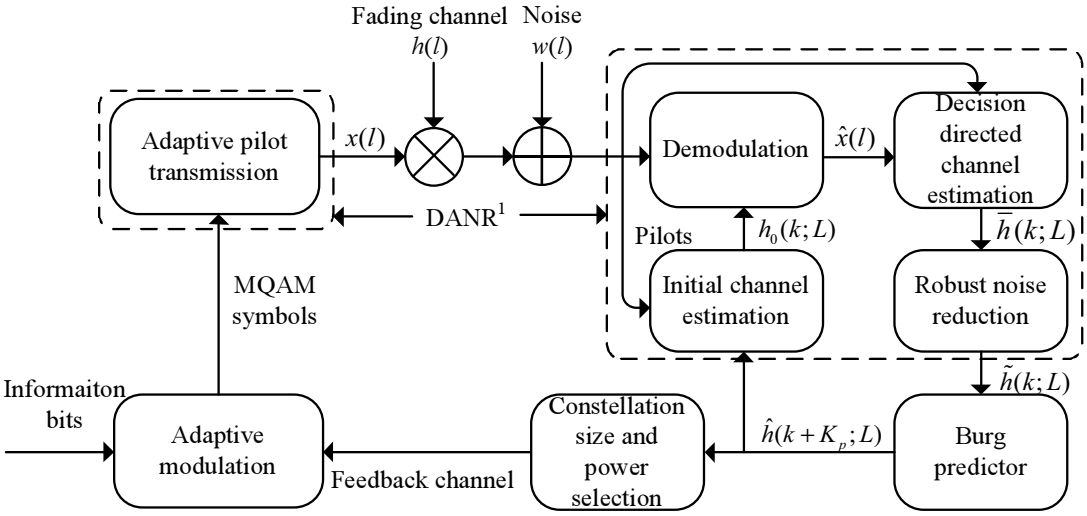

Figure 3.1: System Diagram

the resources consumed by pilots, we investigate practical UAM and ACM systems enabled by DANR-aided LRP, which do not relay on unrealistic assumptions employed in previous investigations, e. g., perfect knowledge of channel statistics [25, 57, 58, 63], or extremely large filter order [24]. Moreover, we employ the standard Jakes and our physical fading channel models in the simulations, and determine the set of SNR values where realistic distribution of reflectors aids prediction performance.

The remainder of this chapter is organized as following. The UAM and the ACM schemes enabled by LRP are reviewed in section 3.2. The proposed DANR method is described in section 3.3. Finally, numerical results and conclusions are presented in sections 3.4 and 3.5, respectively.

3.2 AM AIDED BY PREDICTED CSI

The proposed system model is illustrated in Figure 3.1, and frequently used notation is summarized in Table I. We consider a single-carrier flat fading channel and assume

the symbol rate f_s. The equivalent lowpass received lth sample is

$$y(l) = x(l)h(l) + w(l) \tag{3.1}$$

where $x(l)$, $h(l)$, and $w(l)$ are the transmitted symbol, the complex fading channel coefficient with $\mathbb{E}[|h(l)|^2] = 1$, and complex white Gaussian noise with variance N_0, respectively. The channel coefficient is modeled as complex zero-mean Gaussian process with unit variance. We employ the widely used Jakes model, with the autocorrelation function of the channel coefficient approximated by that of the Rayleigh fading, $\mathbb{E}[h(l)h^*(l-\Delta l)] = J_0(2\pi f_{dm}\Delta l/f_s)$ [44], where $J_0(*)$ is the Bessel function of the first kind, and f_{dm} is the maximum Doppler frequency. The transmitted symbols can be either pilots or data symbols. Without loss of generality, we assume that $x(l) = \sqrt{E_p}$ when pilots are transmitted.

To enable adaptive modulation, the fading coefficient is predicted using a linear predictor (LP) [5]. The actual fading coefficient $h(l)$ and its prediction $\hat{h}(l)$ are jointly Gaussian distributed with the cross-correlation [63]

$$\rho \triangleq \mathbb{E}[h(l)\hat{h}^*(l)]/\sqrt{E\left[|h(l)|^2\right]\sigma_{\hat{h}}^2} \tag{3.2}$$

where $\sigma_{\hat{h}}^2 = \mathbb{E}\left[|\hat{h}(l)|^2\right]$. Without loss of generality, we omit the index l, and denote $\gamma = |h|^2$ and $\hat{\gamma} = |\hat{h}|^2$.

In our simulations, the cross-correlation ρ in (3.2) is measured from the observed data set. For the fixed SNR and target BER, the adjustment of thresholds in the adaptive modulation system is determined by ρ. For the linear MMSE predictor, the normalized MSE NMSE $\triangleq \mathbb{E}\left[|h(l) - \hat{h}(l)|^2\right]/\mathbb{E}[|h(l)|^2]$ is given by $1 - \rho^2$ [63], and for general LP, NMSE $\geq 1 - \rho^2$. While the NMSE is often used to measure prediction performance, the SE of AM is affected by the quality of prediction via the joint distribution of γ and $\hat{\gamma}$ [23, 56, 58]. Since ρ in (3.2), not the NMSE, determines this joint distribution [26], the NMSE is not an appropriate indicator of SE in AM aided by fading prediction. Hence, we define the *normalized prediction MSE* as NPMSE $\triangleq 1 - \rho^2$ and use it as a performance measure of predictors in all our plots.

Consider a coded or uncoded AM system that employs MQAM constellation sizes $\{M_1, M_2, \ldots, M_N\}$, $0 < M_{i_1} < M_{i_2}$ for $i_1 < i_2$, and switching thresholds $\{\gamma_0, \gamma_1, \ldots, \gamma_{N+1}\}$, where $0 \leq \gamma_i \leq \gamma_{i+1}$, $\gamma_0 = 0$, and $\gamma_{N+1} = \infty$. When predicted CSI $\hat{\gamma}$ falls in the interval $[\gamma_i, \gamma_{i+1})$, the constellation size M_i is used in transmission. When $0 \leq \hat{\gamma} < \gamma_1$, an outage occurs. For ACM, we adopt the scheme in [22, Fig. 2] that employs a simple rate 1/2 convolutional encoder with four states [64]. It was shown in [3] that this ACM scheme achieves approximately 3 dB power gain relative to the UAM when the CSI is perfect. In this ideal scheme, pilots were not employed. However, in practice, pilot allocation affects both power and bandwidth consumption.

We employ constant power allocation, i.e., the same average MQAM symbol energy E_d is utilized for all $M_i > 0$, due to its excellent performance and low required feedback rate [56, 58]. Given fixed average SNR=E_s/N_0, where E_s is the average overall symbol energy that includes energy of both data and pilot symbols, the calculation of average MQAM data symbol energy E_d depends on the pilot transmission scheme. In all LRP methods investigated in this dissertation, the pilot energy E_p is equal to the average symbol energy, i.e., $E_p = E_s$. Thus, $E_s = E_d \int_{\gamma_1}^{\infty} p(\hat{\gamma}) d\hat{\gamma} = E_d \exp[-\gamma_1/\sigma_{\hat{h}}^2]$ [16, 56], where $p(x)$ is the probability density function of a random variable x. When the SE loss caused by transmitting pilots is not taken into account, the SE is evaluated as

$$S_d = \sum_{i=1}^{N} q_i \int_{\gamma_i}^{\gamma_{i+1}} p(\hat{\gamma}) d\hat{\gamma} \tag{3.3}$$

where q_i is the number of information bits associated with the modulation level M_i.

For imperfect CSI, we employ the UAM method described in [15, 56], and the ACM design in [23]. Given the reliability of prediction ρ (3.2), these methods select thresholds to maximize the SE (3.3) while maintaining the average BER below the target BER P_t [56, 23]. In this chapter, the set of constellation sizes {4, 16, 64, 256} and $P_t = 10^{-4}$ are used for simulations if not specified otherwise. Figure 3.2 shows the SE of these systems S_d for several average SNR levels when the SE degradation due to pilots is not taken into account. For the NPMSE on the order of 10^{-2} or smaller, prediction is sufficiently reliable to maintain

near-optimal bit rate, and the SEs of both UAM and ACM are not sensitive to the variation of the NPMSE. On the other hand, these SEs decrease rapidly as the NPMSE approaches 10^{-1}. We refer to this phenomenon as "crossing the NPMSE threshold". Moreover, the rate of SE decrease is greater for ACM than for UAM. This observation confirms the conclusion in [6, 7] that ACM is more sensitive to prediction errors than UAM. For NPMSE$\approx 10^{-2}$, ACM has about 0.5 bps/Hz coding gain over UAM, while UAM outperforms ACM when the NPMSE approaches 10^{-1}, which is often the case for realistic SNR values in practical mobile radio scenario [5, 57]. Therefore, to achieve positive coding gain in practical systems, the NPMSE should be decreased by employing NR.

Sensitivity of ACM to prediction errors was investigated in [56, 57], and can be explained intuitively as follows. When prediction is unreliable, the BER of M_i-QAM for the AWGN channel at low SNR dominates the calculation of thresholds [23, 56] and results in reduced SE. Since TCM has higher BER than uncoded MQAM given the same bits/symbol in the AWGN channel with low SNR [21], UAM outperforms ACM as the prediction accuracy decreases.

3.3 Long-Range Prediction with Data-Aided Noise Reduction

3.3.1 Frame Structure and Adaptive Pilot Transmission

The frame structure employed in this dissertation is illustrated in Figure 3.3. At the transmitter of the proposed AM system, the transmitted symbols are grouped into frames with L symbols in each frame. To reduce the feedback rate and the complexity of NR, the constellation size is fixed in each frame. Thus, we assume that the fading coefficient is constant during each frame and choose $f_s/L = 100 f_{dm}$ to justify this assumption [65]. We use vectors $\boldsymbol{x}(k) = [x(kL), x(kL-1), \ldots, x(kL-L+1)]^T$ and $\boldsymbol{y}(k) = [y(kL), y(kL-1), \ldots, y(kL-L+1)]^T$ to represent the transmitted and received symbols of the kth frame, respectively (see (3.1)). In addition, we denote $h(k;L) \approx h(kL-l)$, $l \in [0, L-1]$ as the

Table 3.1: Notation

f_{dm}	Maximum Doppler frequency
f_s	Symbol rate
$h(l)$	Channel coefficient of the lth symbol
$h(k;L)$	Channel coefficient of the kth frame
$h_0(k;L)$	Initial channel estimate for the kth frame
$\bar{h}(k;L)$	Decision directed channel estimate for the kth frame
$\tilde{h}(k;L)$	The noise-reduced channel estimate for the kth frame
$\hat{h}(k;L)$	The predicted channel coefficient for the kth frame
$\tilde{h}(n)$, $\hat{h}(n)$	Down-sampled $\tilde{h}(k;L)$ and $\hat{h}(k;L)$ at rate $f_{\text{pred}}=\frac{f_s}{LK}$
L	Frame size
K	Superframe size
E_p	Pilot symbol energy
E_d	Average energy of MQAM symbols
$\bar{E}_d$	Average data (outage and MQAM) symbol energy
$\bar{E}_s$	Average energy of all symbols

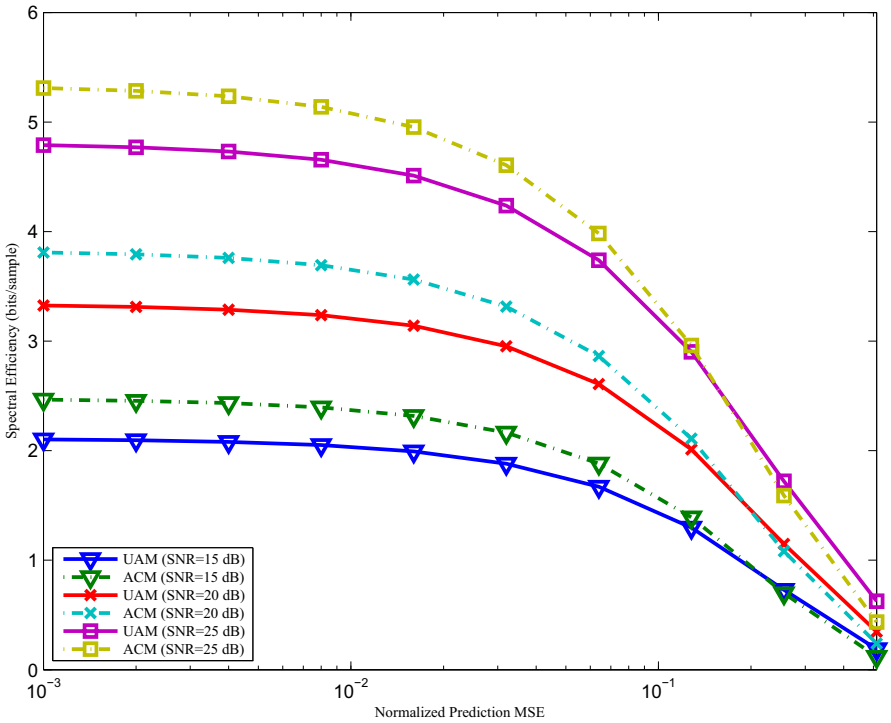

Figure 3.2: Spectral efficiency of adaptive modulation vs. NPMSE for target BER $P_t = 10^{-4}$.

channel coefficient associated with the kth frame.

If one pilot is transmitted in each frame to facilitate NR in LP, the pilot rate is $f_p = f_s/L = 100 f_{dm}$, which is the pilot rate in [15]. However, as stated earlier, this approach wastes a large portion of the available bandwidth due to transmitting oversampled pilots.

In the proposed approach, which combines pilots and decisions to predict the fading coefficient, we group K consecutive frames into one superframe. The observed signals of the mth superframe are represented by a vector of length KL, $\boldsymbol{y}_s(m) = [\boldsymbol{y}^T(mK), \ldots, \boldsymbol{y}^T(mK - K + 1)]^T$. In each superframe, one pilot is transmitted at the last symbol position. It is denoted $x(mKL)$, and referred to as *superframe pilot*. These pilots are used to obtain the initial channel estimates for the demodulation of data symbols. Moreover, if a frame does not contain the superframe pilot and experiences an outage, we also transmit one pilot symbol at the end of that frame. These additional pilot symbols are necessary to

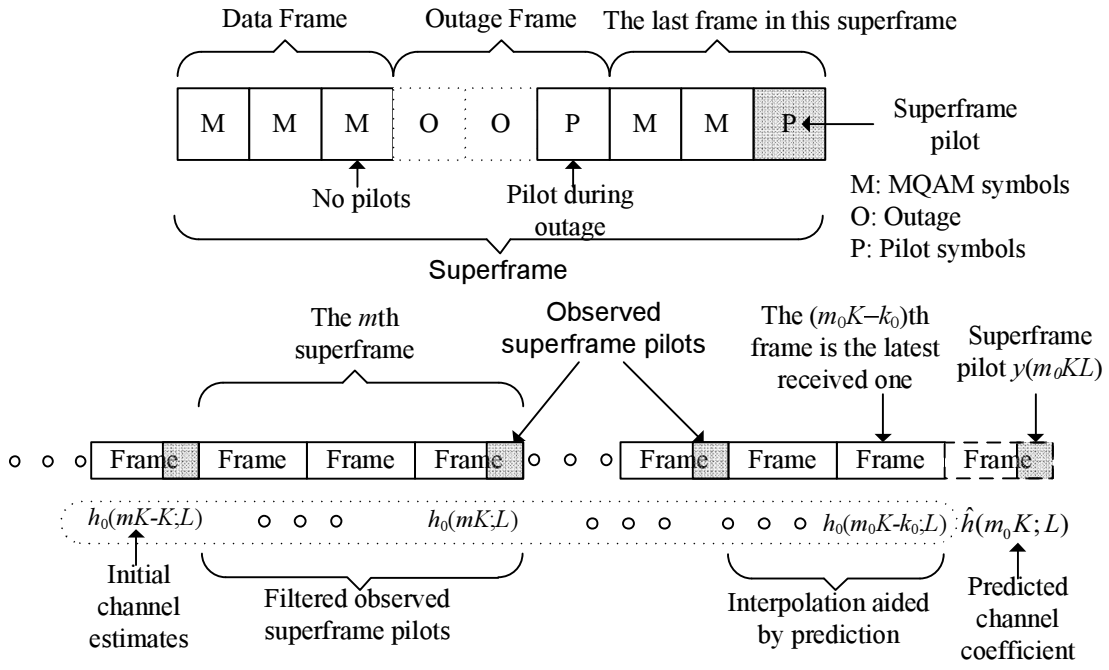

Figure 3.3: Frame structure and initial channel estimates for demodulation (see equation (3)). L=3 symbols/frame, K=3 frames/superframe.

maintain the reliability of prediction during an outage, when decision directed estimation is not possible. This method is referred to as adaptive pilot transmission.

Let $\eta = f_p/f_s$ denote the fraction of bandwidth dedicated to pilots. The actual SE of the system is $\bar{S} = (1-\eta)S_d$ bps/Hz, where S_d is the SE when pilots are not taken into account (3.3). In these systems the pilot rate is on the order of $100f_{dm}$ or $\eta = 1/K$ [15], i.e., the frame rate in DANR, while $\eta = 1/KL$ in DANR. Note that pilots adaptively transmitted during outage frames in our adaptive pilot transmission method do not incur SE penalty since data symbols are not transmitted in those frames.

The power loss caused by transmitting pilots in adaptive pilot transmission also affects system performance. We select $E_s = E_p$ as in a pilot symbol assisted modulation (PSAM) system [46]. Although higher SE is achieved by optimally allocating power to data symbols and pilots as in [58], the SE loss of our method relative to the optimal allocation [58] is small due to the following reasons. First, the pilot symbols account for a small percentage of the available bandwidth. Therefore, reducing the power allocated to pilot

symbols would not significantly improve the power allocated to the data symbols. Second, in DANR, the prediction accuracy mostly depends on the decision-directed data symbols. Increasing the pilot power by sacrificing data symbol power would not significantly improve the prediction accuracy provided the pilot SNR is maintained high enough to demodulate the received data symbols reliably (see Figure 3.14 and 3.15). In addition, in our method, the selected pilot energy does not depend on the accuracy of prediction and is known at the transmitter while in the variable pilot energy method it depends on the NPMSE and needs to be fed back [58]. Thus, our method reduces the required feedback relative to the technique in [58].

In the proposed adaptive pilot transmission, M_i-QAM symbols ($M_i > 0$) occupy $\frac{KL-1}{KL}\int_{\gamma_i}^{\gamma_{i+1}} p(\hat{\gamma})d\hat{\gamma}$ fraction of the bandwidth, and the pilots transmitted during outage frames that do not contain superframe pilots occur with probability $\frac{K-1}{KL}\int_{0}^{\gamma_1} p(\hat{\gamma})d\hat{\gamma}$. Therefore, the power constraint for our DANR method is given by

$$E_s = \frac{KL-1}{KL}E_d\int_{\gamma_1}^{\infty} p(\hat{\gamma})d\hat{\gamma} + \eta E_p + \frac{E_p}{KL}(K-1)\int_{0}^{\gamma_1} p(\hat{\gamma})d\hat{\gamma} \tag{3.4}$$

This power constraint is used in the optimization of thresholds for adaptive modulation.

3.3.2 Initial Channel Estimation for Demodulation

To demodulate received data symbols, we obtain initial channel estimates as illustrated in Figure 3.3. Without loss of generality, assume that the latest received frame has index $(m_0K - k_0)$, $k_0 \in [0, K-1]$. This frame belongs to the m_0th superframe. The initial estimate for frame $(mK-k) \leq (m_0K-k_0)$ in superframe $m \leq m_0$ is computed as

$$h_0(mK-k;L) = \tag{3.5}$$
$$\begin{cases} \frac{k}{K}h_0(m_0K-K;L) + \frac{K-k}{K}\hat{h}(m_0K;L), \text{ if } m = m_0 \text{ and } k_0 \neq 0 \\ \sum_{p=0}^{P_{\text{est}}-1}\omega^*_{est}(k,p)y(mKL-pKL), \text{ otherwise} \end{cases}$$

In the first case in (3.5), the superframe pilot $y(m_0KL)$ associated with superframe m_0 has not been received. Therefore, the initial channel estimates for frames in this

superframe are obtained via simple linear interpolation between $h_0(m_0K-K;L)$ (the initial channel estimate for the last frame in the previous superframe) and $\hat{h}(m_0K;L)$ (the prediction of the channel coefficient for the last frame in the m_0th superframe), where the prediction method is discussed in subsection 3.3.5.

In the second case in (3.5), the mth superframe pilot has been observed (see Figure 3.3). Thus, either $m < m_0$ or $k_0 = 0$. In the latter case, the latest observed frame includes the superframe pilot. The estimation is made by filtering superframe pilot observations $\boldsymbol{y}_p = \begin{bmatrix} y(mKL) & y(mKL-KL) & \dots & y(mKL-P_{\text{est}}KL+KL) \end{bmatrix}^T$, where P_{est} is the order of the estimation filter. Since channel statistics are unknown and time-variant in practice, we employ a robust filter that assumes a flat Doppler spectrum with support $[-f_{dm}, f_{dm}]$ [6]. The $P_{\text{est}} \times 1$ vector of filter coefficients is constructed as

$$\begin{bmatrix} \omega_{est}(k,0) & \dots & \omega_{est}(k,P_{\text{est}}-1) \end{bmatrix}^T = (\boldsymbol{R}+N_0\boldsymbol{I})^{-1}\boldsymbol{r}(k) \tag{3.6}$$

where the $P_{\text{est}} \times P_{\text{est}}$ autocorrelation matrix $\boldsymbol{R}$ has elements $\boldsymbol{R}_{i_1,i_2} = \text{sinc}[(i_1-i_2)\hat{f}_{dm}KL/f_s]$, the $P_{\text{est}} \times 1$ cross-correlation vector $\boldsymbol{r}(k)$ has elements $[\boldsymbol{r}(k)]_i = \text{sinc}[(iK-k)\hat{f}_{dm}L/f_s]$, $\boldsymbol{I}$ is the $P_{\text{est}} \times P_{\text{est}}$ identity matrix, and $\hat{f}_{dm}$ is the estimated maximum Doppler frequency obtained by the FFT operation in [7] aided by decision-directed channel estimates. To calculate $\hat{f}_{dm}$, we first collect past observed decision-directed channel estimates at the frame rate $\bar{h}(k;L)$. The method to obtain $\bar{h}(k;L)$ is introduced in the next subsection. Then we use the FFT method proposed in [66] to obtain $\hat{f}_{dm}$.

Finally, $h_0(k;L)$ is used to obtain $\hat{x}(l)$, the decisions of data symbols$x(l)$ for kth frame. By definition, $\hat{x}(l) = \sqrt{E_p}$ for pilot symbols, and $\hat{x}(l) = 0$ during outage. For UAM, these estimates are employed to demodulate the received data symbols coherently. In the ACM system, coherent demodulation is performed as follows. Suppose the initial channel estimate for the kth frame is denoted $h_0(k;L)$, and assume this frame is not an outage frame. The soft input to the Viterbi decoder for symbol l (see (3.1)) is given by $y(l)/h_0(k;L)$, where $l \in [kL-L+1,\dots,KL]$ are the indices of symbols in the kth frame. To reduce the BER of decisions used for the decision-directed NR, it is desirable to employ

the decoded information bits. At time l_0, we select the survival path with the smallest metric, and use the information bits corresponding to this path as the decisions [67]. These decisions are re-encoded to obtain $\hat{x}(l, l0)$, $l \leq l_0$, the decision of symbols $x(l)$ at time l_0. The decoder traceback length is short for very recently observed data symbols, and they have high error rate. However, a traceback length of $5U$ (where U is the constraint length of the encoder) is sufficient for the decoding [14], and for the four-state encoder used in our system, the corresponding traceback length is only 15 information bits. This interval is much shorter than the memory span of the observation interval used for prediction [5]. Thus, the impact of increased decoding error rate on the performance of our DANR method is small.

3.3.3 Decision-Directed Channel Estimation

Next, the decisions $\hat{x}(l)$ are employed in the estimation of channel coefficient $h(k; L)$ at the frame rate. To derive the estimation filter, we assume perfect decisions $\hat{x}(l)$. This assumption is realistic since error propagation is negligible for $P_t \leq 10^{-2}$ employed in practical AM systems [59, 60]. When kth frame is not an outage frame, we can write out the following observation equation

$$\begin{bmatrix} x(KL-L+1) \\ \dots \\ x(KL) \end{bmatrix} h(k;L) + \begin{bmatrix} w(KL-L+1) \\ \dots \\ w(KL) \end{bmatrix} = \begin{bmatrix} y(KL-L+1) \\ \dots \\ y(KL) \end{bmatrix} \tag{3.7}$$

The least square (LS) estimation of $h(k; L)$ is [68, p. 439]

$$\bar{h}(k;L) = \frac{\begin{bmatrix} x(KL-L+1) & \dots & x(KL) \end{bmatrix}^* \begin{bmatrix} y(KL-L+1) & \dots & y(KL) \end{bmatrix}^T}{\begin{bmatrix} x(KL-L+1) & \dots & x(KL) \end{bmatrix}^* \begin{bmatrix} x(KL-L+1) & \dots & x(KL) \end{bmatrix}^T} \tag{3.8}$$

or

$$\bar{h}(k;L)=\frac{\sum_{l=kL-L+1}^{kL} y(l)\hat{x}^*(l)}{\sum_{l=kL-L+1}^{kL} |\hat{x}(l)|^2}=h(k;L)+\frac{\sum_{l=kL-L+1}^{kL} w(l)\hat{x}^*(l)}{\sum_{l=kL-L+1}^{kL} |\hat{x}(l)|^2}. \tag{3.9}$$

Obviously, we have $\mathbb{E}[\bar{h}(k;L)] = h(k;L)$ so this is an unbiased estimation. The variance of this decision-directed estimate is

$$\begin{aligned} v(k;L) &= \mathbb{E}\left[|\bar{h}(k;L)-h(k;L)|^2\right] \\ &= \frac{\sum_{l=kL-L+1}^{kL} \mathbb{E}[|w(l)\hat{x}^*(l)|^2]}{\left(\sum_{l=kL-L+1}^{kL} |\hat{x}(l)|^2\right)^2} \\ &= \frac{N_0}{\sum_{l=kL-L+1}^{kL} |\hat{x}(l)|^2}. \end{aligned} \tag{3.10}$$

Since $\sum_{kL-L+1}^{kL} |\hat{x}(l)|^2 \approx LE_d \gg E_p$ for large frame size L, the noise power is greatly reduced at the output of (3.9). For outage frames, the noisy pilot observation is employed for channel estimation, i. e., $\bar{h}(k;L) = y(kL)/\sqrt{E_p} = h(k;L) + w(kL)/\sqrt{E_p}$ and $v(k;L) = N_0/E_p$.

3.3.4 Robust Noise Reduction

Since the sampling rate in (3.9) is given by the frame rate, the channel coefficients are highly correlated, while the noise samples are independent at the output $\bar{h}(k;L)$ of the decision-directed estimator. Thus, the power spectrum density of the noise samples is much wider than that of the fading signal. To reduce noise further, we pass $\bar{h}(k;L)$ through a robust NR filter that removes the noise power falling outside of the frequency band of the fading signal. In vector form, the input to this NR filter is $\bar{\boldsymbol{h}}(k;L) = \begin{bmatrix} h(k;L) & \dots & h(k-P_{NR}+1;L) \end{bmatrix}^T$, where P_{NR} is the filer order. Similarly to (3.6), the coefficients of this filter are expressed as a $P_{NR}\times 1$ vector

$$\boldsymbol{\omega}_{NR}(k) = \left[\boldsymbol{R}_{NR} + \boldsymbol{V}(k)\right]^{-1} \boldsymbol{r}_{NR} \tag{3.11}$$

where the $P_{NR}\times P_{NR}$ matrix $\boldsymbol{R}_{NR}$ has elements $[\boldsymbol{R}_{NR}]_{i_1,i_2} = \text{sinc}[(i_1-i_2)\hat{f}_{dm}L/f_s]$, the $P_{NR}\times 1$ vector $\boldsymbol{r}_{NR}$ has elements $[\boldsymbol{r}_{NR}]_i = \text{sinc}[i\hat{f}_{dm}L/f_s]$, and $\boldsymbol{V}(k) = \text{diag}[v(k;L),\ldots,v(k-P_{NR}+1;L)]$. Note that $v(k;L)$ is time-variant and depends on whether given frame experiences an outage. The outputs of the NR filter are

$$\tilde{h}(k;L) = \boldsymbol{\omega}_{NR}^H(k)\bar{\boldsymbol{h}}(k;L) \tag{3.12}$$

Our filter is similar to the NR filter used in [7], but we employ decision-directed channel estimates instead of the over-sampled pilot observations.

Note that the initial channel estimate $h_0(k;L)$ of each frame except the last frame in a superframe is computed by interpolation first, then using filtering (see (3.5)) to improve accuracy. The associated data symbols are also re-demodulated to reduce decision errors, and (3.9) and (3.12) are updated using these recomputed initial estimates.

3.3.5 Long-Range Prediction

Since the outputs of (3.12) are generated at the frame rate, they are decimated by factor J as each new sample $\tilde{h}(k;L)$ is computed, so the effective sampling rate used for prediction $f_{\text{pred}} = f_s/(JL)$ is on the order of f_{dm} [5, 4, 15]. In our simulation, $J = K$, the number of frames per superframe. We denote the sequences $\tilde{h}(k;L)$ and $\hat{h}(k;L)$, decimated at rate f_{pred}, as $\tilde{h}(n)$ and $\hat{h}(n)$, respectively. The one-step prediction of channel coefficient is obtained as [5],

$$\hat{h}(n+1) = \sum_{p=0}^{P_{\text{pred}}-1} \omega_{\text{pred}}^*(p)\tilde{h}(n-p), \tag{3.13}$$

where P_{pred} is the order of predictor, and $\omega_{\text{pred}}(p)$, $p \in [0, P_{\text{pred}}-1]$, are the coefficients of the predictor. Note that a low sampling rate f_{pred} is employed in (3.13), while its outputs are computed at the frame rate. This approach improves prediction accuracy relative to prediction followed by interpolation [5]. Interpolations requires the predicted sample at desired prediction range as well as a few samples with longer prediction ranges. As prediction range increases, the accuracy of those samples decreases dramatically. Hence,

the accuracy of interpolation is significantly degraded by those samples. As in [7], we employ the Burg method to estimate $\omega_{\text{pred}}(p)$ using an observation window that contains B past noise-reduced samples at the rate f_{pred}, where usually $B \gg P_{\text{pred}}$. The normalized spatial prediction range in (3.13) is $f_{dm}JL/f_s$, usually expressed in multiples of carrier wavelength λ [4]. Finally, when the desired prediction interval is longer than J frames, we iterate (3.13) by using previously predicted samples instead of $\tilde{h}(n)$ [5].

The NPMSE and SE of this LRP form a feedback loop. Clearly, the system SE is a function of the NPMSE. Moreover, the accuracy of DANR-aided LRP increases with the effective data rate of the system. Since the theoretical solution for the equilibrium point of this feedback system is very complex, we resort to simulations. First, we employ a NPMSE guess to calculate the thresholds of AM. If the simulated NPMSE is higher/lower than the initial guess, the guessed NPMSE is increased/decreased by a small step Δ. This process is iterated until the guess and the simulated NPMSE are sufficiently close. The final NPMSE and SE represent the equilibrium point of this adaptive system.

3.4 Numerical Results

The standard Jakes model with nine oscillators (34 scatterers) [44] as well as our realistic physical model is employed in simulations [5, 4, 14]. The geometry of physical model data set used for testing LRP enabled by DANR is illustrated in Figure 3.4. It represents a typical flat fading urban mobile radio channel. For all models, we set rms delay spread σ_d=1 us and f_{dm}=100 Hz. In all simulations, the symbol rate f_s= 100 Ksps, the frame size L=10, and K=10 frames per superframe are selected. The sampling frequency of the predictor is f_p=1 KHz=10 f_{dm} and the order P_{pred}=20. The observation window of Burg predictor contains 200 and 100 samples for the Jakes and our practical physical models, respectively.

For comparison, we also simulated the performance of low-rate raw pilot [5] and high-rate pilot methods [15] with the pilot rates $10f_{dm}$ and $100f_{dm}$, respectively. In the

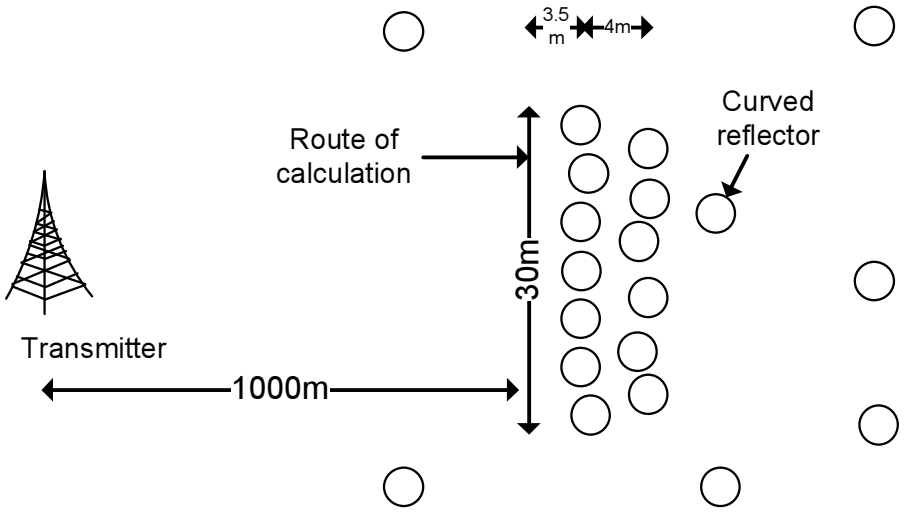

Figure 3.4: Geometry of physical model

raw pilot method, Burg predictor is employed to predict future channel coefficients. In the high rate pilot method, four filters with smoothing lags {0,2,5,10} [15] and filter order 20 perform NR on observed pilots symbols. These NR filters are constructed from estimated f_{dm} as proposed in [7]. Their outputs are down-sampled to a rate of $f_p = 10 f_{dm}$ and then fed into the Burg predictor. For fair comparison, the spatial memory span is given by 2λ for all prediction methods. Moreover, we have employed the outdated CSI method [26] with the same delay as for the prediction methods in this dissertation.

To illustrate the potential of our DANR method, the performance of several techniques that employ ideal assumptions is illustrated for the Jakes model. First, we plot the SE when perfect CSI is available at the transmitter of the adaptive modulation system, and $\eta = 0$. This method provides an upper bound to the achievable SE of all other techniques. Second, we show the performance of the outdated CSI scheme, where one noiseless channel coefficient delayed by the normalized prediction range is employed to enable the adaptive modulation [26]. Finally, the performance of the following "MMSE bound" predictor is also illustrated for the Jakes model. Suppose channel statistics are known, and consider a linear MMSE predictor that employs pilots transmitted at the data rate. Let the memory span of

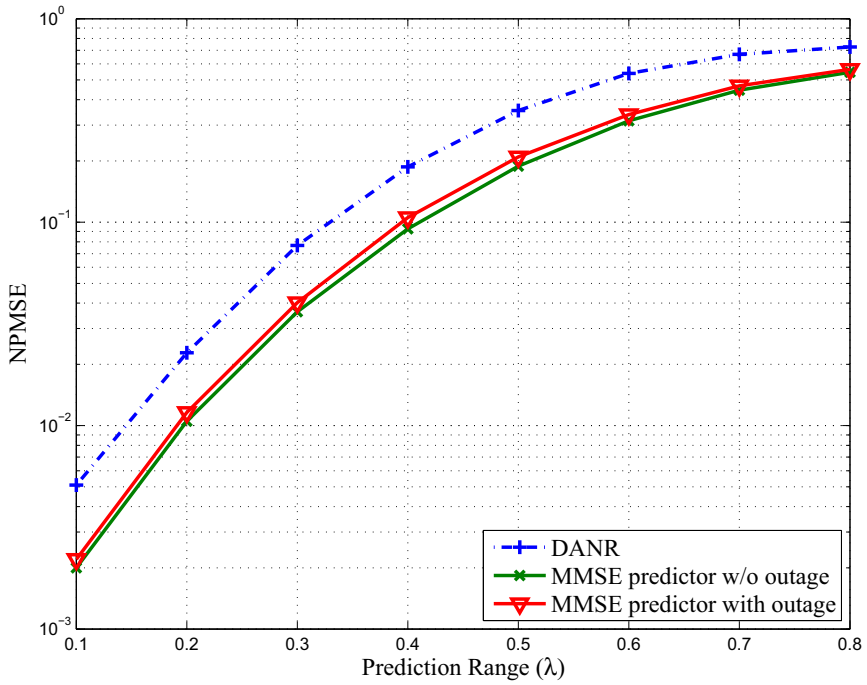

Figure 3.5: NPMSE vs. prediction ranges for DANR method and its MMSE bounds at SNR=20 dB, Jakes model

this predictor be the same as for DANR-aided LRP. Thus, the corresponding filter order of this MMSE predictor is $P_{pred}KL$. Suppose this predictor enables an adaptive modulation scheme with parameters described in section 3.2 and bandwidth loss $\eta = 1/KL$ as for the DANR method.

In Figure 3.5, we consider another MMSE predictor that experiences outages at the same rate as in the LRP-aided adaptive modulation system, i.e. it utilizes adaptive pilot transmission where one pilot symbol is transmitted in each outage frame. This predictor has the same frame structure as our DANR method (Figure 3.3). The outage occurs when the predicted channel power $\hat{\gamma}$ of a frame is below the threshold γ_1, which is calculated for the UAM with pilot-aided prediction methods. For each non-outage frame, L pilots are transmitted. As shown in Figure 3.5, this MMSE predictor with outage shows similar performance to our ideal MMSE predictor. Thus, the impact of outages on the performance of predictors using adaptive pilot transmission is small.

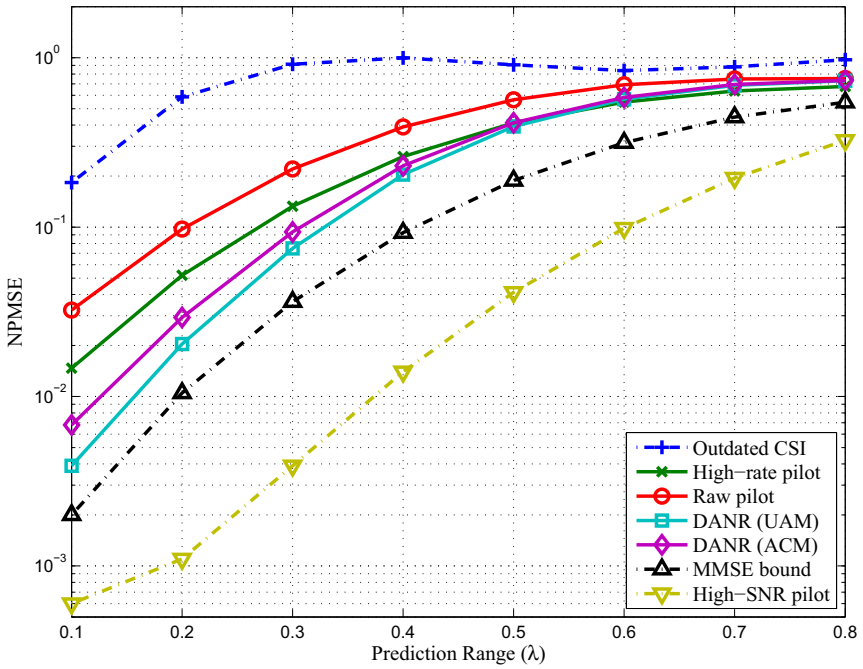

Figure 3.6: NPMSE vs. prediction range for SNR=20dB, target BER of 10^{-4}, and Jakes model

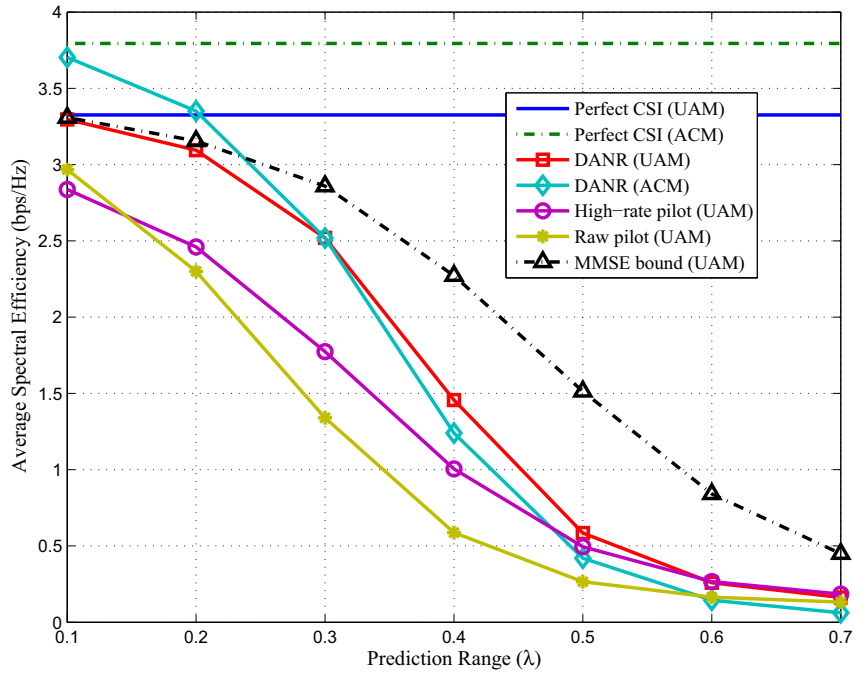

Figure 3.7: Spectral efficiency vs. prediction range for SNR=20dB, target BER of 10^{-4}, and Jakes model

Figure 3.6 and 3.7 illustrate the NPMSE and SE of several prediction methods for the Jakes model when the SNR is 20 dB. Due to accurate decisions of recently received data symbols, the DANR-aided prediction for the UAM is more reliable than for the ACM. However, as discussed in section 3.2, the difference between these two schemes is very small. At short to medium prediction ranges (under 0.3λ), the DANR for both UAM and ACM exhibits excellent prediction accuracy and outperforms the pilot-aided methods. In Figure 3.6, we also simulated the performance of the high-SNR pilot method, i.e., the raw pilot method where the pilot SNR=60 dB is much higher than for the data symbols without incurring power penalty. This method was employed in [5] and it provides a lower bound on the achievable NPMSE for NR methods. As the prediction increases, the residue of AR model instead of the observation noise dominates the prediction error so that the NPMSE gap between high-SNR pilot and raw pilot methods diminishes in Figure 3.6. Therefore, the improvement in NPMSE provided by NR is less significant at large prediction ranges.

In Figure 3.7, the DANR method has higher SE than pilot-aided methods for prediction ranges below 0.5λ. Its gain over the raw pilot method is as high as 1.2 bps/Hz when UAM is used. Even though the ACM is more sensitive to prediction errors than the UAM, the ACM aided by DANR still achieves excellent performance for prediction ranges under 0.2λ, where its SE loss relative to the perfect CSI case is at most 0.43 bps/Hz. This prediction range is sufficient for most adaptive modulation applications [4, 58]. For prediction ranges above 0.2λ, the NPMSE of all practical prediction methods simulated in this dissertation approaches 10^{-1} (see Figure 3.6). Thus, as illustrated in Figure 3.2, they cross the NPMSE threshold, and the SE drops rapidly with the increasing NPMSE at these larger prediction ranges in Figure 3.7. We also observe that although the high-rate pilot scheme has better prediction accuracy than the raw pilot scheme, they have the same SE at short prediction ranges (0.1λ) since the former is penalized by high η values, i.e., oversampled pilots. Finally, we note that excellent performance achieved by the MMSE bound method illustrates the potential of the data-aided prediction approach.

Figure 3.8 and 3.9 illustrate the dependency of NPMSE and SE, respectively, on

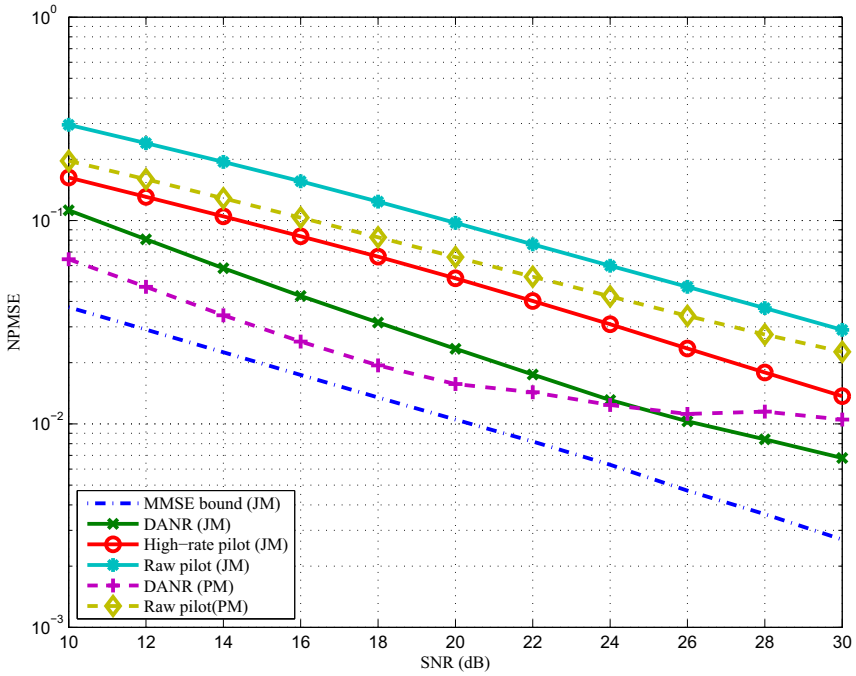

Figure 3.8: NPMSE vs. SNR for prediction range at 0.2λ, UAM, target BER of 10^{-4}, Jakes model (JM) and physical model (PM)

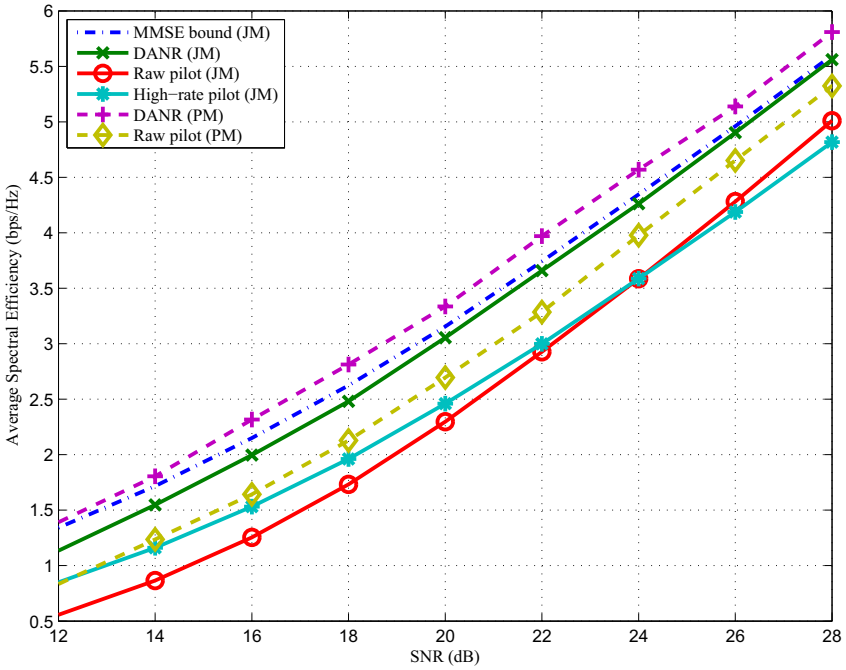

Figure 3.9: Spectral efficiency vs. SNR for prediction range at 0.2 λ, UAM, target BER of 10^{-4}, Jakes model (JM) and physical model (PM)

the system SNR for the prediction range of 0.2λ for the Jakes and physical models when the UAM is employed. For both models, the proposed DANR method outperforms the pilot-aided methods. The SE gain of DANR over the raw pilot method is as large as 0.75 bps/Hz for the Jakes model. We observe that the physical model data set is easier to predict than the Jakes model for most SNR values in Figure 3.8, while the opposite conclusion was reached in [4, 5, 14] for high pilot SNR. This can be explained as follows: for lower SNR, noise dominates prediction performance, and the prediction is aided by lower number and non-uniform distribution of reflectors in the realistic physical model data set. For example, Figure 3.10 shows two scenarios of the physical model. Scenario B is created from scenario A by adding several large reflectors. Figure 3.11 show the NPMSE of these two scenarios obtained by using raw pilot method at SNR=20 dB. With more paths, the NPMSE of the scenario B is higher than that of the scenarios A, while it is still much smaller than that of the Jakes model, which has a larger number of scatterers (34 scatterers). On the other hand, for pilot SNR$\geq$30dB, non-stationarity of fading coefficient dominates prediction errors and limits the accuracy of prediction for the physical model relative to the Jakes model [4, 14].

In Figure 3.8, the NPMSE degradation of the DANR-aided LRP relative to the MMSE bound predictor is due to several practical limitations, including decision errors, AR coefficient mismatch and robust NR filtering. Moreover, in the DANR method, decomposition of the prediction into three stages (decision-directed NR, robust filtering, and Burg predictor) results in simple but suboptimal solution relative to a single MMSE predictor with very large filter order. Note that in this case the SEs of the DANR and the ideal MMSE bound method are very similar (not shown) since the NPMSE is close to or below the NPMSE threshold for both methods (see Figure 3.8).

For the Jakes model, the SE gain of ACM over UAM is illustrated in Figure 3.12 for different SNR and prediction ranges. Both systems are enabled by DANR-aided LRP. The maximum gain, 0.5 bps/Hz, is achieved at SNR=24 dB and the shortest prediction range (0.02λ). As the additive noise level and/or prediction range increase, the SE gap reduces due to less accurate prediction for the ACM system. To achieve a positive gain, the

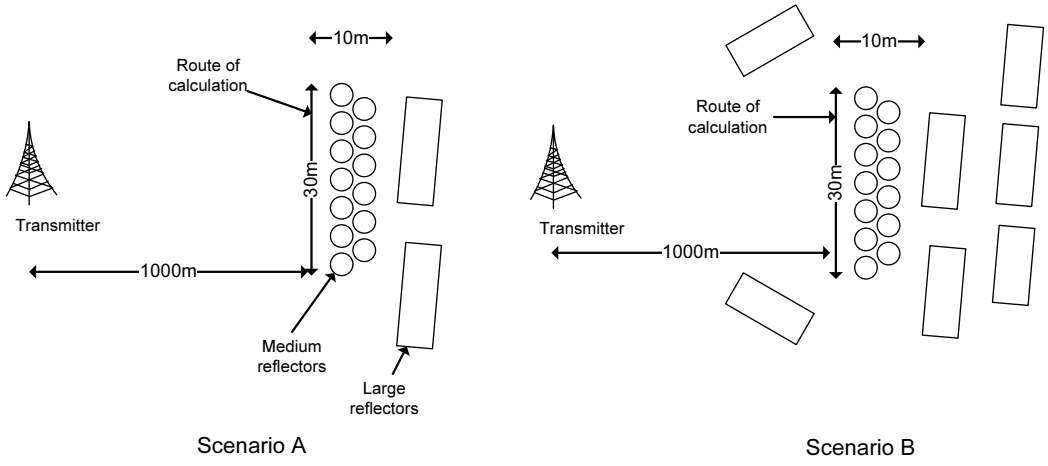

Figure 3.10: Two scenarios of physical model

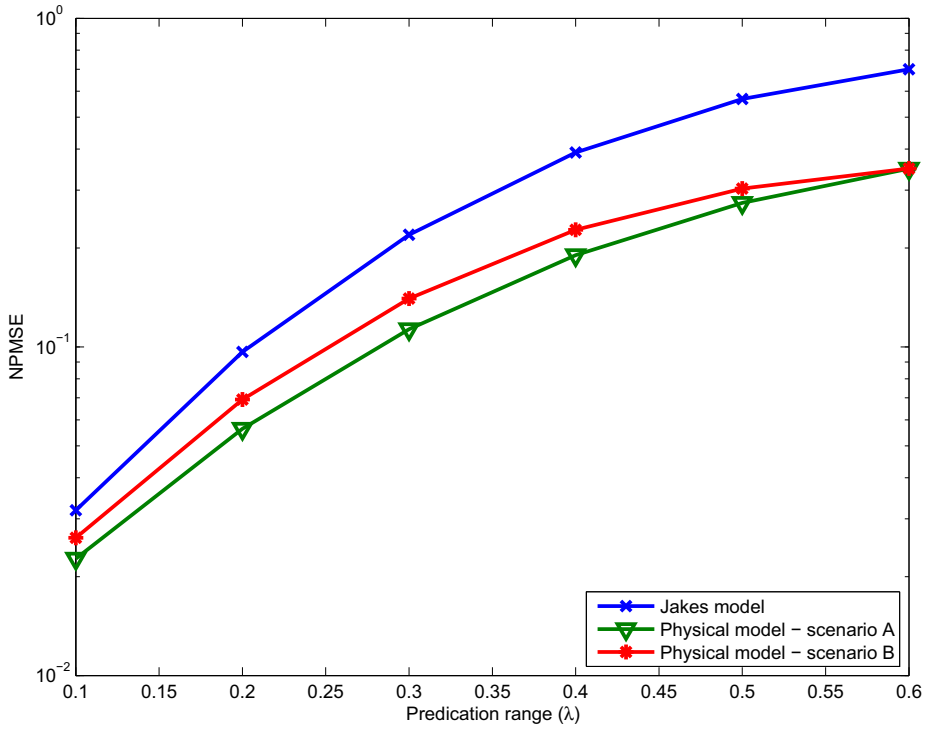

Figure 3.11: NPMSE of different models for SNR=20dB using raw pilot method

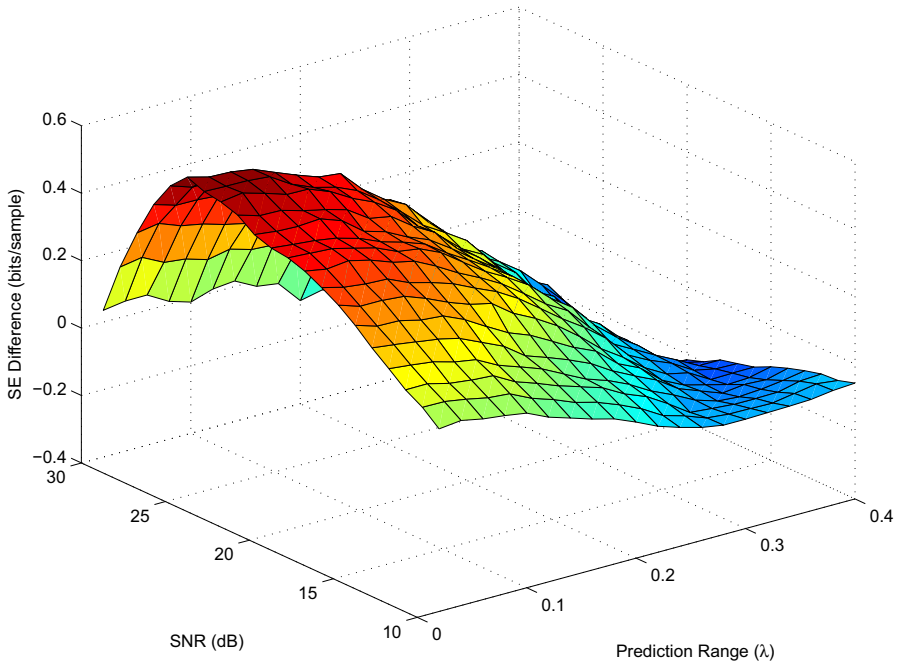

Figure 3.12: Difference in SE between ACM and UAM with LRP enabled by DANR for Jakes model and target BER of 10^{-4}

prediction range has to be less than 0.35λ.

While previous simulations utilized a simple four-state encoder, a more complex encoder with 64 states is considered in Figure 3.13. For short prediction range at 0.1λ and target BER $P_t = 10^{-5}$, the 64-state encoder achieves an additional coding gain of 0.2 bps/Hz over the 4-state encoder. However, as the prediction range grows, this coding gain diminishes and 64-state encoder is outperformed by the 4-state encoder for prediction range larger than 0.2 λ. Similar result was also observed in [57]. It can be explained intuitively as follows. Increasing the number of states improves the coding gain for medium to high SNR, but degrades the BER at low SNR for the AWGN channel [22]. Therefore, the sensitivity of ACM to prediction errors increases as the number of states grows. This conclusion indicates that the selection of encoder for ACM depends on the prediction range of the application. When the CSI can be reliably predicted, selection of large constraint length improves the SE. On the other hand, when the prediction is unreliable, it is unnecessary to use complex encoders/decoders as they will only reduce the SE.

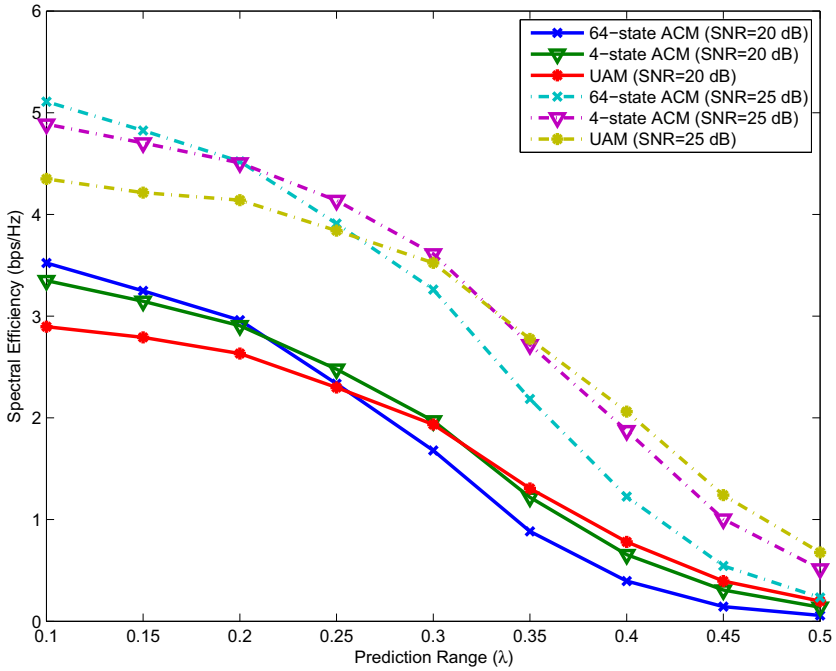

Figure 3.13: Spectral efficiency vs. prediction range for Jakes model and target BER of 10^{-5}

Finally, we analyze the effect of the pilot energy on the DANR performance. In the following, we allow the energy of pilot symbols (E_p) to be Δ_pdB higher than the average energy of all symbols (E_s). In Figure 3.14 the prediction accuracy improves as Δ_p increases. However, the improvement is insignificant since both data and pilot symbols are employed in the DANR method. Increasing pilot energy means decreasing the data energy at the same time. Therefore, as long as the average SNR is fixed, the prediction accuracy remains approximately the same. The small improvement for large Δ_p stems from the fact that higher pilot energy reduces the error in data decisions. In Figure 3.15, the SE for Δ_p={0dB, 3dB, 6dB} are approximately the same. Although the prediction accuracy is slightly improved for high Δ_p values, this advantage is offset by the reduced average data symbol energy. Therefore, the spectral efficiency stays the same for increasing Δ_p. When Δ_p=10dB, the resulting SE is even lower than for smaller Δ_p. The reason is that too much power is allocated to the pilots, and the resulting improvement in prediction accuracy can-

not compensate this power loss of data symbols. On the other hand, it is possible to reduce the pilot energy so that it is lower than the average symbol energy. Although the saved power is allocated to data symbols, this improvement is negligible since the pilots only consume a small portion of the total power in our DANR method. Moreover, the trend in Figure 3.14 shows that reducing the pilot energy would degrade the prediction accuracy.

3.5 Conclusion

A novel DANR method for fading channel prediction is proposed for UAM and ACM systems. It is demonstrated that, compared with previously investigated pilot-aided NR techniques, DANR achieves higher throughput by improving the prediction accuracy while maintaining relatively low pilot rate. The set of SNR values and prediction ranges where positive coding gain is achieved by ACM enabled by DANR-aided LRP is determined and the effect of the prediction range on the choice of the encoder is analyzed. Finally, it is shown that AM aided by LRP has better performance with the realistic physical model than for the Jakes model in the practical SNR range.

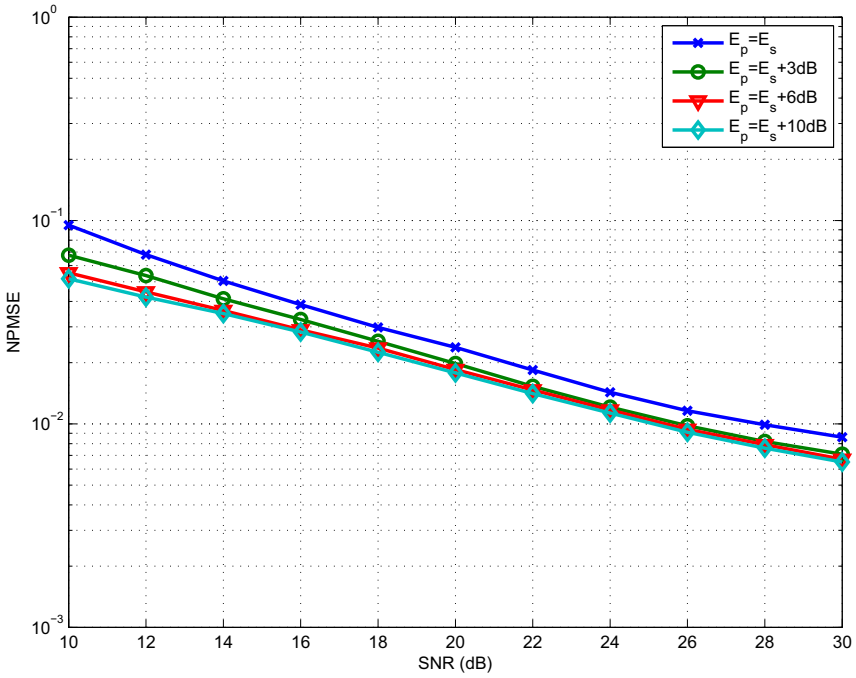

Figure 3.14: Simulated NPMSE vs. average SNR using DANR method for prediction range 0.2λ, UAM, and Jakes model.

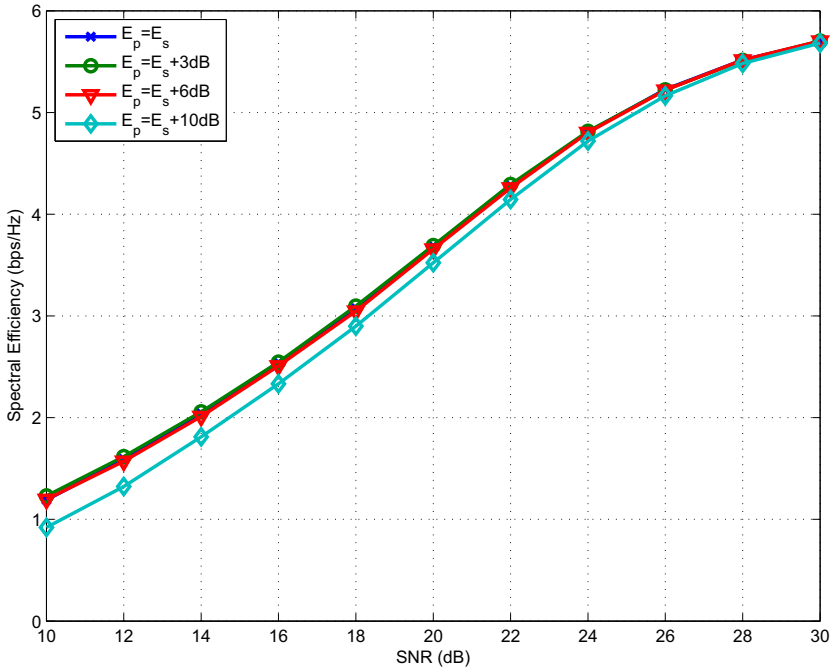

Figure 3.15: Simulated spectral efficiency vs. average SNR using DANR method for prediction range 0.2λ, UAM, and Jakes model.

Chapter 4

Adaptive Bit-Interleaved Coded Modulation for Adaptive OFDM Aided by Long-Range Prediction

4.1 Introduction

The adaptive modulation methods have been studied intensively in the past to combat the severe channel conditions encountered in wired and wireless channels. Among them, the adaptive MQAM that adapts the constellation sizes according to the channel condition significantly improves the SE of the system [21] when the knowledge of CSI is perfect at the transmitter. To further improve the SE, the ATCM are employed to achieve coding gain over the original uncoded MQAM when the CSI is reliable. However, the delay caused by processing and feeding CSI from the receiver back to the transmitter would significantly degrade the quality of CSI. The performance of both ATCM and uncoded MQAM decreases dramatically as the reliability of CSI degrades [56, 23], while the coding gain of ATCM over uncoded MQAM diminishes at the same time [23]. For extremely unreliable CSI, the uncoded MQAM even outperforms ATCM [17].

To improve the reliability of CSI, the LRP techniques was proposed [5, 4]. Com-

pared with outdated CSI caused by delay [26], the LRP techniques provides more accurate CSI for practical delay values. However, even when advanced LRP techniques are employed, the SEs of ATCM and UAM are still reduced noticeable by the prediction errors [16, 17] at medium prediction range (0.2-0.5 carrier wavelength). Therefore, for mobile radio systems where the delay falls in that prediction range, it is necessary to find adaptive modulation schemes are are less sensitive to the prediction errors.

As one of the diversity methods, bit-interleaved coded modulation (BICM) has shown good performance over the unreliable wireless communication channel [69, 70]. Compared with the bandwidth efficient trellis coded modulation (TCM) scheme, it achieves higher code diversity, but at the price of reduced Eucliean distance [70]. Moreover, the adaptive bit-interleaved coded modulation (ABICM) was proposed in [27] to combat the unreliable CSI by utilizing its high code diversity. The simulation results show that the ABICM maintains the SE even for highly unreliable CSI.

In the original ABICM method [27], the Bhattacharyya bound of single-bit-error probability and only the minimum distance between coded bit sequences are considered to determine the constellation size while maintaining the target BER. This method only provides coarse estimates to the single-bit-error probability. The result is compared with the single-bit-error probability of a non-adaptive BICM scheme, whose BER performance is known from simulation, to infer the BER of ABICM. Then the constellation size is selected to maintain the target BER. Due to inaccurate estimates of BER, the simulated BER of this ABICM method significantly deviates from the specified target BER [27]. Hence, additional experimental energy adaptations are required to bring the BER to the desired level.

The ABICM was also investigated in [71, 72]. However, these papers assumed that the perfect CSI is available to the transmitter, which is reasonable for static fading channel such as in-door channel, but not for the out-door mobile radio systems. Moreover, it was shown in [27] that ATCM is more suitable for reliable CSI than ABICM due to its high Eucliean distance. Therefore, in this dissertation, we focus on the application of ABICM in

mobile radio systems where the perfect CSI is hard to obtain.

In this dissertation, we advocate the usage of expurgated bound for ABICM. The expurgated bound, proposed in [70], provides accurate BER estimates to the BICM in AWGN channel as well as Rician and Rayleigh fading channels. New ABICM methods based on expurgated bound are developed. The resulting BER of these methods are closer to the target BER then the original ABICM method.

In [27], the outdated CSI is employed to demonstrate the performance of ABICM, while in practice the LRP technique usually provides more reliable CSI [5, 4]. In this dissertation, we illustrate the performance of ABICM in OFDM system aided by LRP. Although ABICM is less sensitive to the quality of CSI than ATCM and uncoded MQAM, the LRP technique still significantly improves the SE over the outdated CSI method.

The remainder of this chapter is organized as follows. In section 4.2, the model of OFDM system aided by LRP is presented. Section 4.3 discusses the original and new ABICM methods. The simulation results and conclusions are contained in section 4.4 and 4.5, respectively.

4.2 Adaptive OFDM Aided by Long-Range Prediction

The system diagram of the adaptive OFDM under investigation is shown in Figure 4.1. At the transmitter, the information bits are coded through a convolutional encoder, whose outputs are interleaved. The adaptive bit and power loading algorithm maps the interleaved bits into MQAM symbols for all subcarriers, and determines their constellation sizes and energies using the CSI fed back from the transmitter. To facilitate the LRP, pilot symbols are inserted. Then inverse fast Fourier transform (IFFT) is employed to get the OFDM symbol in the time domain. To prevent inter-symbol interference (ISI), a cyclic prefix (CP) is added to the OFDM symbol before transmission. The transmitted signal experiences frequency-selective Rayleigh fading channel. At the receiver, the CP is removed and the FFT restores the transmitted symbols in the frequency domain. The data

symbols are demodulated, de-interleaved and decoded to obtain the decisions of information bits. Based on the observed pilot symbols, the future CSI is predicted and fed back to the transmitter.

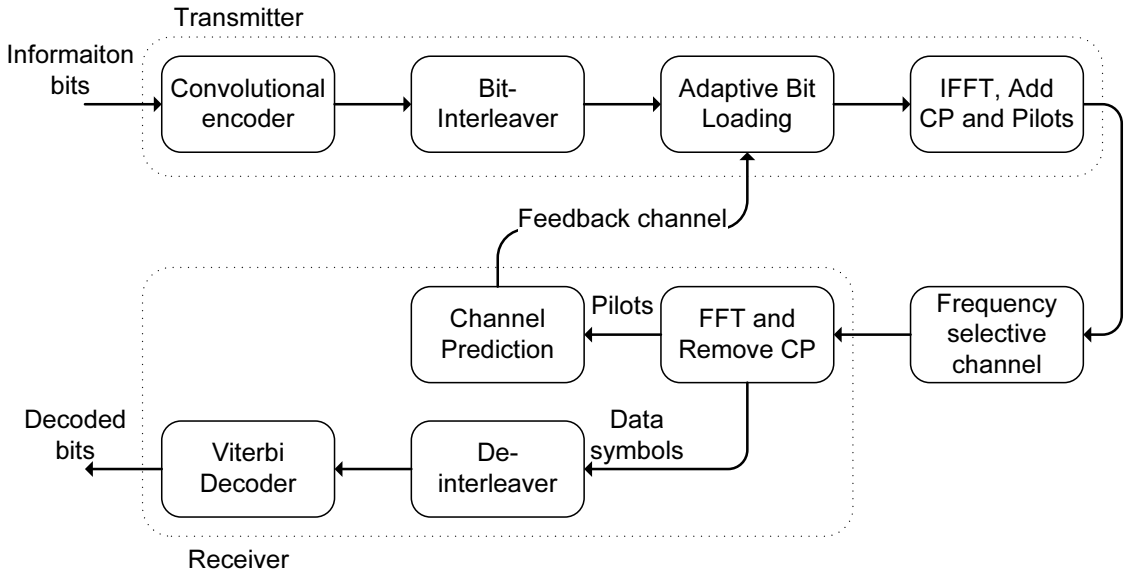

Figure 4.1: System diagram of adaptive OFDM that uses ABICM and LRP.

4.2.1 Channel Model

For the wireless channel, the complex channel coefficient is given by [59]

$$h(t,\tau) = \sum_{l=1}^{L} \gamma_l(t)\sigma\left[\tau - \tau_l(t)\right] \tag{4.1}$$

where $\tau_l(t)$ and $\gamma_l(t)$ are the delay and complex amplitude of the lth path, respectively. Further, the pth path can be decomposed into the result of N_l scatterers:

$$\gamma_l(t) = \sum_{p=1}^{N_l-1} \beta_{p,l} e^{j2\pi t f_{dm}\cos\theta_{p,l}} \tag{4.2}$$

where $\theta_{p,l}$ and $\beta_{p,l}$ are the incident angle and the amplitude of the pth scatter in the lth path, respectively, and f_{dm} is the maximum Doppler frequency. In the well known Jakes model, the angles $\theta_{p,l}$ are uniformally distributed in $[0, 2\pi]$. Then the corresponding

cross-correlation function in the time domain is $\mathbb{E}\left[\gamma_l(t)\gamma_l^*(t-\tau)\right]/\mathbb{E}\left[|\gamma_l(t)|^2\right] = J_0(2\pi f_{dm}\tau)$, where $J_0(*)$ is the modified Bessel function of the first kind [44]. In (4.1) and (4.2), τ_l and $\theta_{p,l}$ varies slowly compared with the OFDM symbol rate [73]. Therefore, it is reasonable to assume that they are constants and drop their time indices.

The frequency response of this OFDM channel at frequency f is obtained through Fourier transform of (4.1):

$$H(t,f) = \sum_{l=1}^{L} \gamma_l(t) e^{-2j\pi\tau_n f}. \tag{4.3}$$

Without loss of generality, we normalize the above frequency responses such that $H(n,k) \sim \mathcal{CN}(0,1)$. Define the symbol duration and the subcarrier spacing in OFDM system as T_s and Δf respectively. Then the discrete channel response samples are

$$H(n,k) \triangleq H(nT_s, k\Delta f) = \sum_{l=1}^{L} \gamma_l(nT_s) e^{-2j\pi\tau_n k\Delta f}. \tag{4.4}$$

The two-dimensional autocorrelation function of $H(n,k)$ is

$$\begin{aligned}
\mathbb{E}\left[H(n+\Delta n, k+\Delta k)H^*(n,k)\right] &= \sum_{l=1}^{L}\sum_{l'=1}^{L} \mathbb{E}\left[\gamma_l(nT_s+\Delta nT_s)\gamma_l'(nT_s)\right] e^{-2j\pi\tau_n\Delta k\Delta f} \\
&= \sum_{l=1}^{L} \mathbb{E}\left[\gamma_l(nT_s+\Delta nT_s)\gamma_l(nT_s)\right] e^{-2j\pi\tau_n\Delta k\Delta f} \\
&= J_0(\Delta nT_s) \sum_{l=1}^{L} \mathbb{E}\left[|\gamma_l|^2\right] e^{-2j\pi\tau_n\Delta k\Delta f} \\
&\triangleq r_t(\Delta n) r_f(\Delta k)
\end{aligned} \tag{4.5}$$

where

$$r_t(\Delta n) \triangleq \mathbb{E}\left[H(n+\Delta n,k)H^*(n,k)\right] = J_0(2\pi f_{dm}\Delta t T_s) \tag{4.6}$$

$$r_f(\Delta k) \triangleq \mathbb{E}\left[H(n,k+\Delta k)H^*(n,k)\right] = \sum_{l=1}^{L} \mathbb{E}\left[|\gamma_l|^2\right] e^{-2j\pi\tau_n\Delta k\Delta f} \tag{4.7}$$

are the cross-correlation in frequency and time domain, respectively.

When symbol $X(n,k)$ is transmitted on the kth subcarrier of the nth OFDM symbol, then the corresponding received signal is

$$Y(n,k) = H(n,k)X(n,k) + W(n,k) \tag{4.8}$$

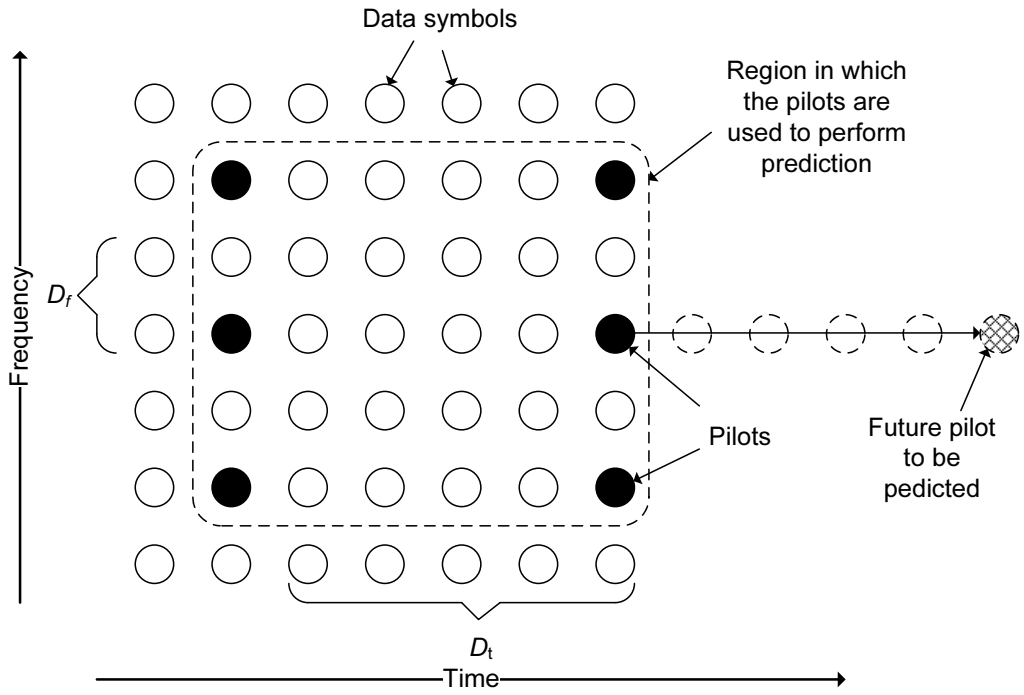

Figure 4.2: The pilots transmitted in OFDM system and long-range prediction.

where $W(n,k)$ is the complex additive white Gaussian noise with variance N_0.

4.2.2 Pilot-Symbol Assisted Long-Range Prediction

In this OFDM system, pilot symbols are transmitted to assist LRP. As shown in Figure 4.2, the pilots are transmitted on grids such that the time spacing between consecutive pilots symbols is D_tT_s and the frequency spacing between adjacent pilot tones is $D_f\Delta f$.

Without loss of generality, we assumed that the transmitted pilots in frequency domain are $X(n,k) = \sqrt{E_p}$, where E_p is the pilot symbol energy.

Next, we assume that the n_0th symbol is the latest observed pilot symbol, and consider the prediction on the k_0 subcarrier, which is also a pilot tone. Using the predictions on all pilot tones, the predictions on other tones can be obtained through interpolation. To predict on the k_0 subcarrier, we employ the past pilot observations within a rectangular

area as shown in Figure 4.2. This area includes the k_0th subcarrier and $2P_f$ closest pilot tones, and P_t past OFDM symbols that contain pilots. Thus, there are $(2P_f+1)P_t$ pilots in this area. Suppose that we need to predict n_p symbols ahead of the n_0th symbol. The corresponding normalized spatial prediction range is $f_{dm}n_pT_s$, which is usually expressed in the unit of carrier wavelength λ [4].

In vector form, the past P_t pilots on the kth subcarrier is

$$\boldsymbol{y}(k) = \begin{bmatrix} Y(n_0,k) & Y(n_0-D_t,k) & \dots & Y(n_0-D_tP_t+D_t,k) \end{bmatrix}^T. \tag{4.9}$$

Using this notation, the pilot observations that will be used to perform the prediction are contained in a single vector:

$$\underline{\boldsymbol{y}} = \begin{bmatrix} \boldsymbol{y}^T(k_0-P_fD_f) & \boldsymbol{y}^T(k_0-P_fD_f+D_f) & \dots & \boldsymbol{y}^T(k_0+P_fD_f) \end{bmatrix}^T \tag{4.10}$$

Note that if the k_0th subcarrier is the outmost subcarrier, there is no pilot tones on one of its sides. In that case, the quality of prediction would be different for different subcarriers as observed in [73]. For convenience, we assume that there are additional pilot tones transmitted outside of the system bandwidth so that the quality of predicted CSI is uniform across all subcarriers that contain data symbols. When P_f is small and the number of subcarriers is large, the bandwidth and energy consumed by transmitting additional pilots can be safely ignored.

With predictor coefficients $\underline{\boldsymbol{\omega}} = [\omega_1, \omega_2, \dots, \omega_{(2P_f+1)P_t}]^T$, the linear prediction of $H(n_0+n_p, k_0)$ is [5]

$$\hat{H}(n_0+n_p, k_0) = \underline{\boldsymbol{\omega}}^H \underline{\boldsymbol{y}}. \tag{4.11}$$

For the linear minimum mean square error (LMMSE) predictor, the coefficient vector $\underline{\boldsymbol{\omega}}$ is

$$\begin{aligned} \underline{\boldsymbol{\omega}} &= \mathbb{E}\left[\underline{\boldsymbol{y}} \times \underline{\boldsymbol{y}}^H\right]^{-1} \mathbb{E}\left[\underline{\boldsymbol{y}} \times H^*(n_0+n_p, k_0)\right] \\ &= \left(E_p\boldsymbol{R}_t \bigotimes \boldsymbol{R}_f + N_0\boldsymbol{I}\right)^{-1} \left(\sqrt{E_p}\boldsymbol{r}_{y,t} \bigotimes \boldsymbol{r}_{y,f}\right) \end{aligned} \tag{4.12}$$

where $\boldsymbol{R}_t$ is the time-domain autocorrelation matrix with elements $\boldsymbol{R}_t(i_1,i_2) = r_t[D_t(i_1 - i_2)]$, $\boldsymbol{R}_f$ is the frequency-domain autocorrelation matrix with elements $\boldsymbol{R}_f(i_1,i_2) = r_f[D -$

$f(i_1 - i_2)]$, $\boldsymbol{r}_{y,t}$ is the time domain cross-correlation vector with elements $\boldsymbol{r}_{y,t}(i) = r_t(n_p + iD_t - D_t)$,$i \in \{1, \ldots, P_t\}$, $\boldsymbol{r}_{y,f}(i)$ is the frequency domain cross-correlation vector with elements $\boldsymbol{r}_{y,f}(i) = r_f[iD_f - (P_f + 1)D_f]$,$i \in \{1, \ldots, 2P_f + 1\}$, $\boldsymbol{I}$ is the identity matrix, and $\bigotimes$ is the Kronecker product. The corresponding normalized mean square error (NMSE) of this predictor is [5]

$$\begin{aligned}\sigma^2 &= \mathbb{E}\left[|H(n_0 + n_p, k_0) - \hat{H}(n_0 + n_p, k_0)|^2\right] \\ &= 1 - \left(\boldsymbol{r}_t \bigotimes \boldsymbol{r}_f\right)^H \left(\boldsymbol{R}_t \bigotimes \boldsymbol{R}_f + N_0\boldsymbol{I}\right)^{-1} \left(\boldsymbol{r}_{y,t} \bigotimes \boldsymbol{r}_{y,f}\right)\end{aligned} \tag{4.13}$$

To illustrate the performance of this predictor, we consider an OFDM system that uses FFT size of 128, and we leave 8 outmost subcarriers as guard. The bandwidth of each subcarrier is 10.94 KHz, which is the same as in the Mobile WiMAX system. The total bandwidth of this system is about 1.3 MHz. For each OFDM sysmbol, a cyclic prefix of duration 33.5 us is added so the OFDM symbol rate is 10 KHz. We assume that the carrier frequency is 2.5 GHz, which is typical for the Mobile WiMAX deployment [74]. The vehicular speed is set to 86.4 km/hour and the corresponding maximum Doppler frequency is f_{dm}=200 Hz. The pilot spacing in time domain is $D_t = 8$ so that the sampling frequency for predictor is 8 KHz/8=1 KHz=$5f_{dm}$, which is suggested in [5]. Other parameters are shown in Table 4.1.

For the fading channel, we adopt the ETSI Vehicular B model [75], which has six paths and rms delay spread of 4 us. The time-varying coefficient of each path is generated from the modified Jakes model with 32 scatterers [76]. Since in this model the largest path delay is 20 us [75, Table 1.2.2.3], which is shorter than the duration of CP, the ISI can be removed at the receiver.

The performance of LRP in this OFDM system is shown in Figure 4.3. The NMSE of prediction is under 10^{-1} for prediction ranges shorter than 0.1λ. As the prediction range increases, the NMSE saturates to 0.6-0.7.

Table 4.1: Parameters of simulated OFDM system

Number of subcarriers	120
Subcarrier bandwidth	10.94 KHz
System bandwidth	1.3 MHz
Cyclic prefix duration	33.5 us
OFDM symbol rate	8 Ksps
Pilot spacing in time (D_t)	8
Pilot spacing in frequency (D_f)	8
Predictor order in time (P_t)	20
Predictor order in frequency ($2 \times P_f + 1$)	3
Maximum Doppler frequency (f_{dm})	200 Hz
rms delay spread	4 us
Number of paths	6

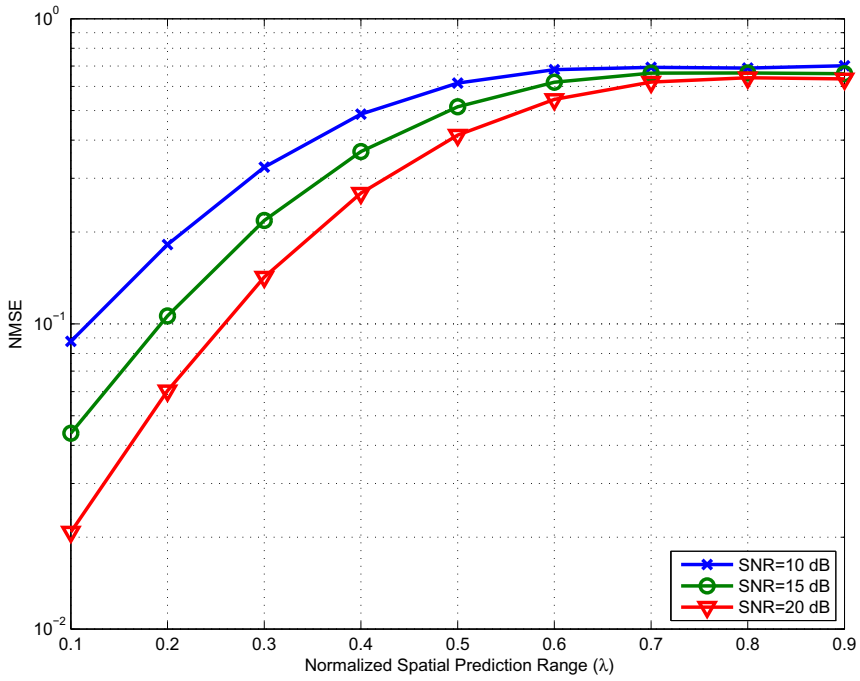

Figure 4.3: NMSE vs. prediction range for different SNR (E_p/N_0) levels.

4.2.3 Adaptive Discrete Bit Loading for OFDM

In the OFDM system, there are K subchannels with independent additive Gaussian noise. Suppose the minimum energy required on the kth channel is E_k so that $m_k = g_{\hat{H}_k}(E_k)$ coded bits/symbol can be transmitted while the target BER is maintained. For the fixed coding rate r of convolutional encoder, we are interested in the solution that maximizes the SE while satisfying the overall energy constraint, i.e., [77]

$$\max \left\{ r \sum_{k=1}^{K} m_k \right\} \text{ subject to } \sum_{k=1}^{K} E_k \leq E_T \tag{4.14}$$

where E_T is the energy constraint for each OFDM symbol.

In practice, we have $g_{\hat{H}_k}(0) = 0$ and the function $g_{\hat{H}_k}(E_k)$ is concave [72]. Under this condition, it has been shown in [77] that the discrete waterfilling algorithm based on the greedy principle [78] achieves the optimal solution of (4.14). This algorithm is shown in Table 4.2. In step S1 of this algorithm, the function $g^{-1}_{\hat{H}_k}(m_k)$ provides the energy to transmit

m_k bits on the kth subcarrier while maintaining the target BER. Thus, Δ_k denotes the additional energy required to enlarge the constellation size. The remaining energy available to allocate is E_{rem}.

Table 4.2: The discrete waterfilling algorithm based on the greedy principle

S0) Initialize $E_{rem} \leftarrow E_T$, $m_k \leftarrow 0$ for all $k \in \{1, \ldots, K\}$

while true

S1) Use the predicted channel coefficient $\hat{H}_k$ to calculate $\Delta_k = g^{-1}_{\hat{H}_k}(m_k + 1) - g^{-1}_{\hat{H}_k}(m_k)$ for all $k \in \{1, \ldots, K\}$. (If 2^{m_k+1} is larger than the maximum constellation size, then $\Delta_k \leftarrow \infty$)

S2) Find $k_0 = \arg\min_k \Delta_k$, $k \in \{1, \ldots, K\}$

if $E_{rem} < \Delta_{k_0}$ **then**

S4) Stop allocation

else

S5) Assign $m_{k_o} \leftarrow m_{k_o} + 1$, $E_k \leftarrow g^{-1}_{\hat{H}_k}(m_k + 1)$, $E_{rem} \leftarrow E_{rem} - \Delta_{k_o}$.

For ABICM in OFDM system, the difficult part is to find out the equation $m_k = g_{\hat{H}_k}(E_k)$, or equivalently $E_k \triangleq g^{-1}_{\hat{H}_k}(m_k)$, for the given channel condition. Although this problem was discussed in [72], perfect CSI was assumed there. Moreover, the solution given in [72] is based on some experimental parameters to maintain the required BER.

Here, we are interested in the mobile radio communication system. In this system, the prediction errors are present for practical feedback delays between receiver and transmitter. Therefore, we will investigate the cases where only imperfect CSI is available as in [27]. Moreover, we are looking for analytical solutions that does not depend on the experimental results to maintain the required BER.

4.3 ABICM with Imperfect CSI

4.3.1 Imperfect Channel State Informaiton

Without loss of generality, we focus on the channel coefficient of one subcarrier in one OFDM symbol. Dropping the time and subcarrier indexes (n, k) in (4.4), we denote the corresponding channel coefficient and its linear MMSE prediction as H and $\hat{H}$, respectively. Since H is a Gaussian random variable and $\hat{H}$ is its linear prediction (4.11), they are jointly Gaussian distributed with cross-correlation [63]

$$\rho = \mathbb{E}\left[H\hat{H}^*\right] / \sqrt{\mathbb{E}\left[|H|^2\right]\mathbb{E}\left[|\hat{H}^*|^2\right]} \tag{4.15}$$

Since ρ is related to the NMSE σ^2 by $\sigma^2 = 1 - \rho^2$ for the LMMSE prediction [63], both of them are frequently used as a indicator of CSI reliability, e.g., in [5, 26, 27, 63].

Given the prediction $\hat{H}$, the actual channel coefficient can be written as

$$H = \hat{H} + e \tag{4.16}$$

where the prediction error $e \sim \mathcal{CN}(0, \sigma^2)$. According to the orthogonality principle, e and $\hat{H}$ are independent Gaussian random variables. For the adaptive MQAM, we are interested in the amplitudes $\alpha \triangleq |H|$ and $\hat{\alpha} \triangleq |\hat{H}|$. Conditioned on predicted $\hat{\alpha}$, α is a Rician random variable with the probability density function (PDF) [79, eq. (3)]

$$p\left(\alpha|\hat{\alpha}\right) = 2\alpha(1+K)\exp\left[-K - \alpha^2(1+K)\right] \times I_0\left[2\alpha\sqrt{K(1+K)}\right] \tag{4.17}$$

where $K \triangleq \hat{\alpha}^2/\sigma^2$ is the Rician parameter.

4.3.2 Original ABICM Scheme

In ABICM, the MQAM constellation of transmitted symbol is selected according to the predicted $\hat{H}$. The candidate constellations are $\{\chi_m\}$ of sizes $|\chi_m| = 2^m$, $2^m \in \mathbb{M}$, where $\mathbb{M}$ is the set of possible MQAM constellation sizes employed by the adaptive modulator. The minimum Euclidean distance between any two points in the constellation χ_m is $d_{min,m}$. The average symbol energy of constellation χ_m is $E(m)$.

Now we consider the evaluation of $E(m)$, the minimum energy required in a subchannel to maintain target BER P_t while the knowledge of noise variance N_0 and predicted channel amplitude $\hat{\alpha}$ is available. Since the exact BER analysis is hard to obtain, utilization of relaxed Bhattacharyya bounds was suggested in [27]. In this method, the error probability of a single bit-error event is considered. Suppose that the symbol X is transmitted, and another symbol $\hat{X}$ is chosen at the receiver. Both X and $\hat{X}$ are selected from constellation χ_m. For the AWGN channel with channel amplitude α, the Bhattacharyya bound of this error event is [80, p. 63]

$$\mathbb{P}\left(X \to \hat{X} \middle| \alpha\right) \leq \exp\left(-\frac{\alpha^2 |X-\hat{X}|^2}{4N_0}\right), X \in \chi_m, \hat{X} \in \chi_m. \tag{4.18}$$

As stated before, the channel amplitude α is Rician distributed given the channel prediction $\hat{H}$. Hence, this Bhattacharyya bound needs to be averaged over the distribution of α, i.e.,

$$\begin{aligned}
\mathbb{P}\left(X \to \hat{X} | \hat{\alpha}\right) &\leq \int_0^\infty \exp\left(-\frac{\alpha^2 |X-\hat{X}|^2}{4N_0}\right) p(\alpha|\hat{\alpha}) d\alpha \\
&\leq \int_0^\infty \exp\left(-\frac{\alpha^2 d_{min,m}^2}{4N_0}\right) p(\alpha|\hat{\alpha}) d\alpha \\
&= \frac{1+K}{1+K+C} \exp\left(-\frac{KC}{1+K+C}\right)
\end{aligned} \tag{4.19}$$

where $C \triangleq d_{min,m}^2 (K+1)\sigma^2/(4N_0)$ and $K \triangleq \hat{\alpha}^2/\sigma^2$. In the last step of (4.19), we used [79, eq. (33)] and (4.17).

In order to relate the Bhattacharyya bound in (4.19) to the target BER, a non-adaptive BICM scheme, which is called *nominal scheme*, is considered in [27]. Both this nominal scheme and the ABICM scheme under investigation use the same convolutional encoder. The CSI is unknown to the transmitter in the nominal scheme, so that its Bhattacharyya bound has to be averaged over Rayleigh distributed α:

$$\begin{aligned}
\mathbb{P}\left(X \to \hat{X}\right) &\leq \int_0^\infty \exp\left(-\frac{\alpha^2 |X-\hat{X}|^2}{4N_0}\right) p(\alpha) d\alpha \\
&= \frac{1}{1+|X-\hat{X}|^2/(4N_0)} \\
&\leq \frac{1}{1+d_0^2/(4N_0)}
\end{aligned} \tag{4.20}$$

where d_0^2 is the minimum Euclidean distance in the constellation employed by the nominal scheme. Define D_0 as the value of the bound (4.20) when the target BER is achieved. It can be determined through simulation of nominal scheme. For example, a nominal scheme that uses 8PSK modulation and rate 2/3, 8-state convolutional encoder achieves the target BER of 10^{-5} at SNR 18dB in [27, 69]. The corresponding bound obtained from (4.20) is $D_0 = 1/\left[1 + d_0^2/(4N_0)\right] = 0.0976$ [27]. It is argued in [27] that the BER of ABICM can be maintained approximately at the BER of the nominal scheme if (4.19)$\leq D_0$. Hence, to maintain the BER, the energy required to transmit m bits/symbol is

$$g_{\hat{H}}^{-1}(m) = \arg\min_{E(m)} \left\{ \frac{1+K}{1+K+C} \exp\left(-\frac{KC}{1+K+C}\right) - D_0 \leq 0 \right\} \tag{4.21}$$

where K and C are defined under (4.19), and the relation between $E(m)$ and $d_{min,m}$ depends on the specific QAM constellation. For instance, there is $d_{min,m}^2 = 6E(m)/(2^m - 1)$ for square QAM constellations [72].

There are potential problems with this original ABICM method. First, bounds of single-bit-error probability are employed in (4.21), while the performance is measured by BER. Due to this mismatch, the resulting BER may significantly deviate from the target BER. Second, the Bhattacharyya bound is inaccurate and only the error at the minimum Euclidean distance was considered. Utilization of inaccurate estimates for both the ABICM and the nominal scheme (4.21) makes the resulting BER unpredictable. Due to above reasons, it was shown that the simulated BER deviates from the target BER [27, Fig. 5]. In [27], the actual transmit power has to be adjusted in simulation to ensure that the resulting BER is close enough to the target BER. However, the amount of power adjustment has to be determined through a number of simulations.

4.3.3 Improved ABICM Method 1

As stated before, one of the problems for the original ABICM method is that the upper-bound for single-bit-error probability is loose. Here, we consider the adoption of expurgated bound, which is proven to be a much tighter bound than the Bhattacharyya

union bound and BICM union bound for the calculation of BER [70].

For simplicity, we first consider the single-bit-error probability as in the original ABICM scheme [27]. Suppose that two bit sequences $\underline{\boldsymbol{c}}$ and $\hat{\underline{\boldsymbol{c}}}$ stem from the same states and end with the same states. They only differ by $d = 1$ bit at the ith bit such that $c_i \neq \hat{c}_i$, $c_i \in \underline{\boldsymbol{c}}$ and $\hat{c}_i \in \hat{\underline{\boldsymbol{c}}}$. Assume this bit c_i is transmitted through constellation χ_m, the labeling rule is μ [70], and the associated channel prediction is $\hat{H}$. Then we denote the pair-wise error probability (PEP) as

$$\mathbb{P}(\underline{\boldsymbol{c}} \to \hat{\underline{\boldsymbol{c}}}|\chi_m, \hat{H}) = f(d = 1, \mu, \chi_m, \hat{H}). \tag{4.22}$$

When Gray labeling is applied, the expurgated bound of above equation can be easily obtained as [70, eq. (47)]

$$f_{ex}(d = 1, \mu, \chi_m, \hat{H}) = m^{-1} \sum_{p=1}^{m} 2^{-1} \sum_{b\in\{0,1\}} 2^{-(m-1)} \sum_{X\in\chi_{m,b,p}} \mathbb{P}(X \to \hat{Z}|\hat{H}) \tag{4.23}$$

where $\chi_{m,b,p}$ is the the subset of constellation χ_m that has label b at the pth bit position, and $\hat{Z}$ is the unique nearest neighbor of X in subset $\chi_{m,\bar{b},p}$.

To calculate $P(X \to \hat{Z}|\hat{H})$, we assume maximum likelihood (ML) detection with the knowledge of perfect CSI H at the time of detection. Denote the received symbol as Y when X is transmitted. The conditional probability of Y is [70, eq. (23)]

$$p_H(Y|X) = \frac{1}{\pi N_0} \exp\left(-|Y - HX|^2/N_0\right) \tag{4.24}$$

Then the metric difference between X and $\hat{Z}$ at the decoder is [70, eq. (33)]

$$\Delta(X, \hat{Z}) = \log p_H(Y|X) - \log p_H(Y|\hat{Z}) \tag{4.25}$$

and the single-bit-error probability is [70, eq. (34)][59, p. 943]

$$\mathbb{P}(X \to \hat{Z}|\hat{H}) = \mathbb{P}\left[\Delta(X, \hat{Z}) \leq 0\right] = \frac{1}{2\pi j} \int_{\varepsilon-j\infty}^{\varepsilon+j\infty} \Phi^{\hat{H}}_{\Delta(X,\hat{Z})}(s) \frac{ds}{s} \tag{4.26}$$

where ε is a small positive number and $\Phi_\Delta(s)$ is given by [70, eq. (35)][81]

$$\Phi^{\hat{H}}_{\Delta(X,\hat{Z})}(s) = \mathbb{E}\left[e^{-s\Delta(X,\hat{Z})}|\hat{H}, X, \hat{Z}\right] = \frac{\exp\left(-\frac{s(1-s\hat{N}_0)K\left|X-\hat{Z}\right|^2/(K+1)}{1+s(1-s\hat{N}_0)K\left|X-\hat{Z}\right|^2/(K+1)}\right)}{1 + s(1 - s\hat{N}_0)K\left|X - \hat{Z}\right|^2/(K+1)} \tag{4.27}$$

where $\hat{N}_0 = (\sigma^2 + |\hat{H}|^2)N_0$ and $K = |\hat{H}^2|/\sigma^2$ is the Rician parameter. In above equation, the second equality is from [70, eq. (50)], but have a different definition of $\hat{N}_0$ since the variance of H conditioned on $\hat{H}$ is not normalized to one in our case. Finally, (4.26) can be evaluated numerically through the method advocated in [82].

As in [27], we select a non-adaptive BICM scheme as the nominal scheme. This nominal scheme has the same convolutional encoder as the ABICM under test. When this nominal scheme achieves the target BER at a certain SNR, then the corresponding D_0 is calculated from (4.23) using the fixed constellation and the facts that $\hat{H} = 0$. For example, when 4-state rate-2/3 convolutional encoder and 4-QAM are employed, the target BER 10^{-5} is achieved at E_s/N_0=17.1 dB and the corresponding $D_0 = f(1, \mu, \chi_2, 0)$=0.0095. Finally, the energy required to maintain the BER is

$$g_{\hat{H}}^{-1}(m) = \arg \min_{E(m)} \left\{ f_{ex}(d = 1, \mu, \chi_m, \hat{H}) - D_0 \leq 0 \right\} \tag{4.28}$$

This equation is similar to the equation used by original method, but more accurate expurgated bound is employed.

4.3.4 Improved ABICM Method 2

In (4.28), both $f_{ex}(d = 1, \mu, \chi_m, \hat{H})$ and D_0 are the single-bit-error probability, i.e., $d = 1$. However, d_{free}, the free Hamming distance of convolutional codes, is higher than 1. As a result, the expurgated bound of the ABICM scheme does not rely on this probability [70]. To further improve the ABICM scheme, we consider the expurgated bound for PEP with $d > 1$ in this subsection.

Suppose that two bit sequences $\underline{\boldsymbol{c}}$ and $\underline{\hat{\boldsymbol{c}}}$ stem from the same states and end with the same states. They differ by d bits. The channel predictions and constellations associated with those error bits are $\hat{\boldsymbol{H}} = [\hat{H}^1, \hat{H}^2, \ldots, \hat{H}^d]$ and $\boldsymbol{\chi} = [\chi^1, \chi^2, \ldots, \chi^d]$, respectively. Here, we assume that ideal interleaver is applied so that $\hat{H}^i$, $i \in [1, d]$ are independent identically distributed (i.i.d) variables. Similarly, the corresponding channel coefficients $\boldsymbol{H} = [H^1, H^2, \ldots, H^d]$ are also independent variables. The PEP is bounded by [70, eq.

(48)]

$$\mathbb{P}(\underline{\boldsymbol{c}} \to \underline{\hat{\boldsymbol{c}}}|\boldsymbol{\chi}, \hat{\boldsymbol{H}}) \leq f_{ex}(d, \mu, \boldsymbol{\chi}, \hat{\boldsymbol{H}}) \triangleq \frac{1}{2\pi j} \int_{\varepsilon - j\infty}^{\varepsilon + j\infty} \prod_{i=1}^{d} \psi_{ex}^{i}(s) \frac{ds}{s}. \tag{4.29}$$

As in [70, eq. (49)], here we have defined

$$\begin{aligned} \psi_{ex}^{i}(s) &\triangleq \mathbb{E}\left[e^{-s\Delta(X,\hat{Z})}|\hat{H}^{i}, \chi^{i}\right] \\ &= \frac{1}{m^{i} 2^{m^{i}}} \sum_{p=1}^{m^{i}} \sum_{b=0}^{1} \sum_{X \in \chi_{b,p}^{i}} \Phi_{\Delta(X,\hat{Z})}^{\hat{H}^{i}}(s) \end{aligned} \tag{4.30}$$

where m^i is the size of constellation χ^i, $\{X \in \chi_{b,p}^i\}$ is the subset of χ^i that has bit b on the pth bit, and $\Phi_{\Delta(X,\hat{Z})}^{\hat{H}^i}(s)$ was defined in (4.27). In the first equality of (4.27), the expectation is taken over X and the channel coefficient H^i. In (4.29), the product of ψ_{ex}^i is due to the fact that $p(\boldsymbol{H}|\hat{\boldsymbol{H}}) = p(H^1|\hat{H}^1)p(H^2|\hat{H}^2)\dots p(H^d|\hat{H}^d)$.

Without loss of generality, assume that we know the predicted channel coefficient and the constellation size associated with coded bit c_{i_0}, i.e, $\hat{H}^{i_0}$ and χ^{i_0}, where $i_0 \in \{1, \dots, d\}$. Our goal is to determine the associated symbol energy that satisfies the target BER through maintaining the PEP (4.29). However, to determine the PEPs that involves the bit c_{i_0}, we need to know the channel predictions, constellation sizes, as well as transmission energies for all correlated coded bits c_i, $i \in \{1, \dots, d\}$ and $i \neq i_0$ as in (4.29). Due to the random interleaving, this knowledge is not available in practical systems. To circumvent this problem, note that bit loading algorithm should select the symbol energy and constellation so that all symbols have the same target BER. Since $\psi_{ex}^i(s)$ determines the error probability of each symbol, we assume $\psi_{ex}^i(s) = \psi_{ex}^{i_0}(s)$ for all $i \in \{1, \dots, d\}$, where i_0 is one of the d indices with known $\hat{H}^{i_0}$ and χ^{i_0}. Based on this assumption, we can calculate the expurgated bound (4.29) that uses $\hat{H}^{i_0}$ and χ^{i_0} instead of vectors $\hat{\boldsymbol{H}}$ and $\boldsymbol{\chi}$ in (4.29). This simplified expurgated bound is defined as

$$\hat{f}_{ex}(d, \mu, \chi^{i_0}, \hat{H}^{i_0}) \triangleq \frac{1}{2\pi j} \int_{\varepsilon - j\infty}^{\varepsilon + j\infty} \left[\psi_{ex}^{i_0}(s)\right]^{d} \frac{ds}{s} \tag{4.31}$$

The above equation is exactly the expurgated bound of PEP for non-adaptive BICM scheme

that uses constellation χ^{i_0} in the Rician fading channel with K factor $|\hat{H}^{i_0}|^2/\sigma^2$ for all bits [70, eq. (48)]. Similar to (4.26), this bound (4.31) can be solved numerically.

To use the discrete waterfilling algorithm in Table 4.2, we need to calculate $g_{\hat{H}}^{-1}(m)$, which is the required symbol energy to transmit m bits per symbol while maintaining the target BER. Therefore, it is necessary to relate (4.31) to the target BER. For a rate k_c/n_c convolutional encoder with free Hamming distance d_{free}, the well-known union bound for BER P_b is [70, eq. (26)]

$$P_b \leq \frac{1}{k_c} \sum_{d=d_{free}}^{\infty} W_I(d) \hat{f}_{ex}(d, \mu, \chi^{i_0}, \hat{H}^{i_0}). \tag{4.32}$$

where $W_I(d)$ is the weight of error events at Hamming distance d for this code. Due to the utilization of simplified expurgated bound (4.31), we are able to determine the upper-bound on the BER using only one pair $\{\chi^{i_0}, \hat{H}^{i_0}\}$ in (4.32). Finally, if we know the predicted channel coefficient $\hat{H}$ and have selected the constellation size $|\chi_m| = 2^m$ for a symbol, then the average symbol energy $g_{\hat{H}}^{-1}(m)$ that satisfies the BER constraint is derived from (4.32):

$$g_{\hat{H}}^{-1}(m) = \arg\min_{E(m)} \left\{ \frac{1}{k_c} \sum_{d=d_{free}}^{\infty} W_I(d) \hat{f}_{ex}(d, \mu, \chi_m, \hat{H}) - P_t \leq 0 \right\} \tag{4.33}$$

where P_t is the target BER. We refer (4.33) as the improved ABICM scheme 2 and its effectiveness will be examined in the next section.

4.4 Simulation Results

In all simulations, the target BER is 10^{-5} and the set of constellation sizes is $\mathbb{M} = \{0, 4, 16, 64\}$. If not specified otherwise, the rate-2/3 4-state optimal convolutional encoder [59] is employed for all methods. The OFDM system and the channel model discussed in section 4.2 are used to examine different ABICM methods.

First, we investigate the BER achieved by three different ABICM methods described in section 4.3. For both the original ABICM and the improved ABICM scheme 1, the nominal non-adaptive BICM scheme uses quadrature phase shifted keying (QPSK) and the resulting D_0 values are 0.0375 (4.21) and 0.0095 (4.28), respectively.

Fig 4.4 and 4.5 show the simulated BER against the NMSE of prediction for different methods at SNR=15 dB and 20 dB, respectively. In both figures, the BER of the original ABICM is significantly lower than the target BER, which causes its SE to be lower than for the other two methods. Although the BER of the improved method 1 is closer to the target BER than the original method, it is notably higher than the target BER for most MMSE values. Finally, the BER of improved method 2 is very close to the target BER for all simulated MSE and SNR values. These results indicate that the inaccurate estimation of error probability in (4.19) and (4.20) is only one of the reasons that the original method misses the target BER. When more accurate expurgated bound is employed for the calculation of single-bit-error probability, the improved method 1 still misses the target BER. Additional reasons include the fact that the single-bit-error probability cannot accurately reflect the BER of ABICM and the dependency on a non-adaptive ABICM nominal scheme. When we eliminate the nominal scheme and calculate the BER directly in the improved method 2, the simulated BER is very close to the target BER. Hence, we used only the improved method 2 in the remaining simulations.

Figure 4.6 compares the SE of different adaptive modulation methods for different SNR values and CSI reliability. When CSI is reliable (σ^2=0.001), the ATCM achieves the highest SE for medium to high SNR. The reason is that ATCM has larger Euclidean distance than the ABICM [22]. On the other hand, the SE of ATCM is significantly degraded by imperfect CSI, while the ABICM still maintains high SE for σ^2=0.1. Both ABICM and ATCM outperform UAM. We also show the SEs of nonadaptive BICM schemes that uses QPSK and 16QAM. With the aid of CSI, the ABICM significantly outperforms these non-adaptive schemes. On the other hand, due to the coding gain and diversity, the non-adaptive BICM with 16QAM has slightly higher SE than that of the UAM when $\sigma^2 = 0.1$. Figure 4.7 shows that the corresponding BERs of ABICM are very close to the target BER specified before simulation.

Figure 4.8 shows the variation of SE versus NMSE. The SEs of both UAM and ATCM drop rapidly as the NMSE increases. Since the ATCM is more sensitive to the

prediction errors than UAM [23], the former is slightly outperformed by the latter for σ^2 above 0.2. On the other hand, the SE of ABICM decreases slowly, the resulting SE of ABICM is still above 1.0 bps/Hz for σ^2=0.5.

In Figure 4.9, we can see that the SE of both UAM and ATCM decreases rapidly with increasing prediction range, and their SEs approach zero for prediction range above 0.4λ. On the other hand, the SE of ABICM saturates at about 0.9 bps/Hz for long prediction ranges. Although ABICM is much less sensitive to prediction errors than UAM and ATCM, the LRP technique is still very useful to ABICM. In Figure 4.9, the LRP nearly doubles the SE of outdated CSI method for prediction ranges 0.2-0.3λ.

4.5 Conclusions

In this chapter, we investigated the ABICM aided by LRP for OFDM systems. New ABICM methods based on the expurgated bound are proposed. Compared with previously investigated techniques, these new methods achieve better BER accuracy. In particular, one of the proposed methods generates the BER that is very close to the specified target BER. It is shown that ABICM is less sensitive to the prediction errors than the ATCM and UAM. However, the LRP technique still significantly improves the SE of ABICM over the outdated CSI method at practical prediction ranges.

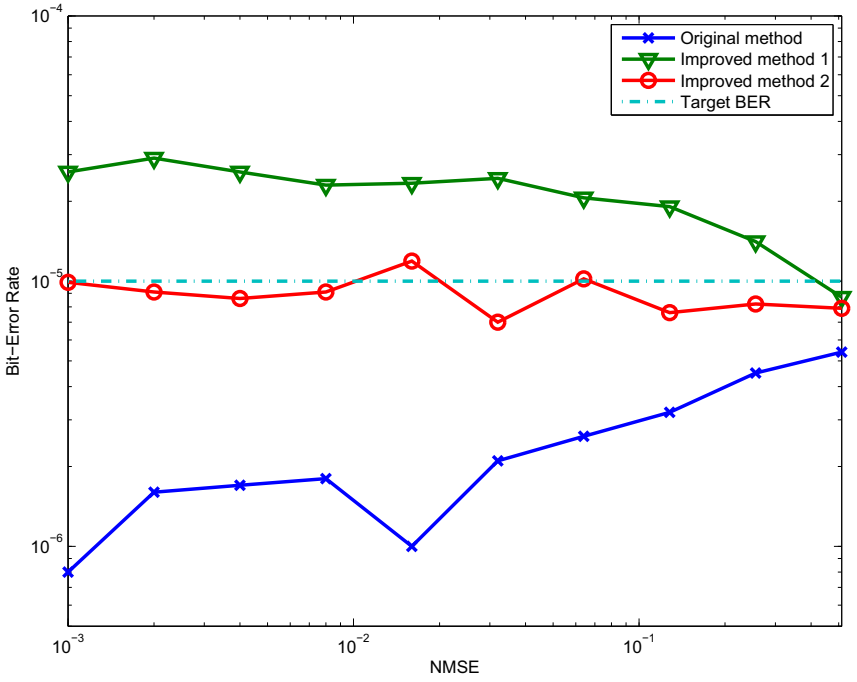

Figure 4.4: BER vs. NMSE of prediction for SNR $E_T/(K \times N_0)$=15 dB.

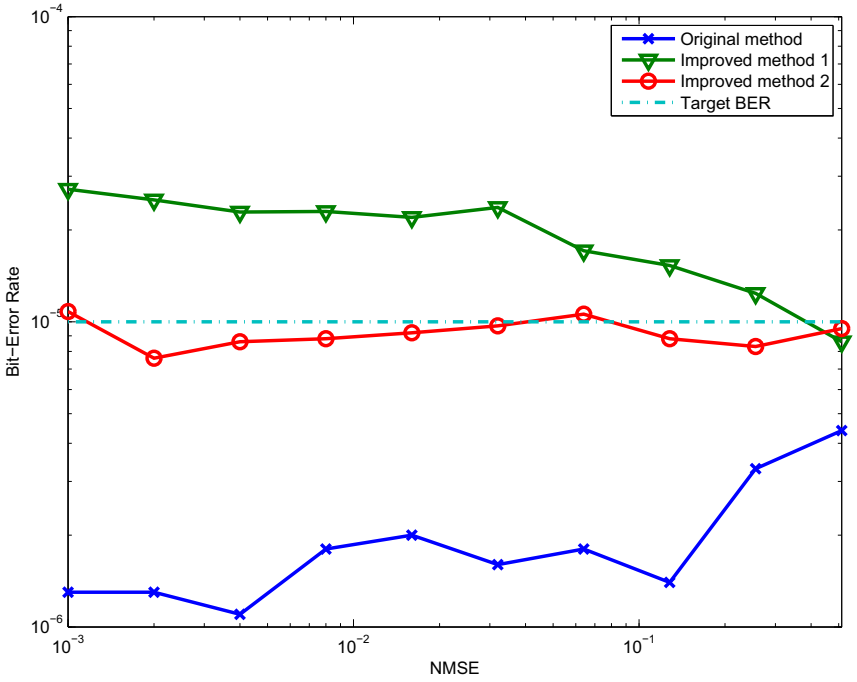

Figure 4.5: BER vs. NMSE of prediction for SNR $E_T/(K \times N_0)$=20 dB.

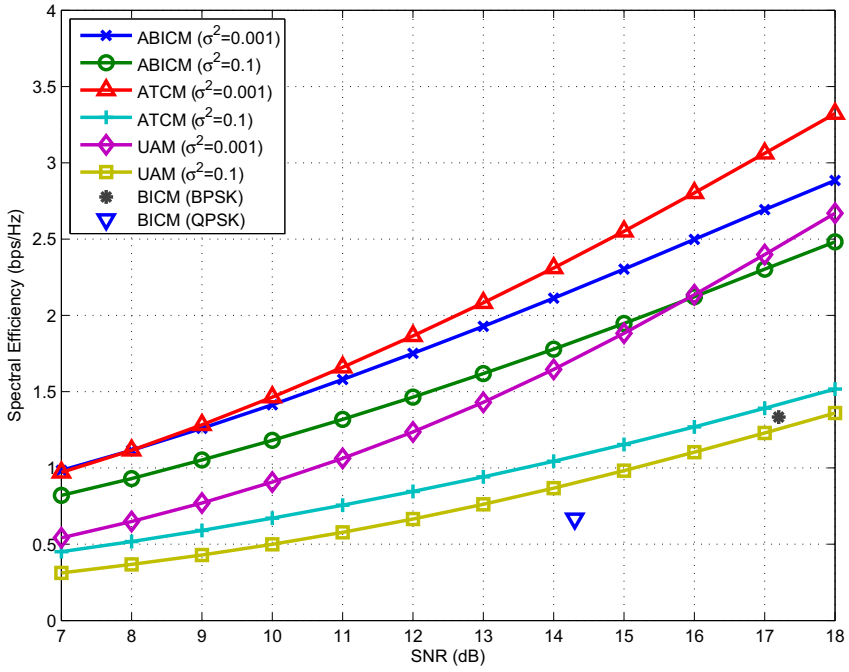

Figure 4.6: SE vs. SNR ($\frac{E_T}{K \times N_0}$) for $\sigma^2 = 0.001$ and $\sigma^2 = 0.1$

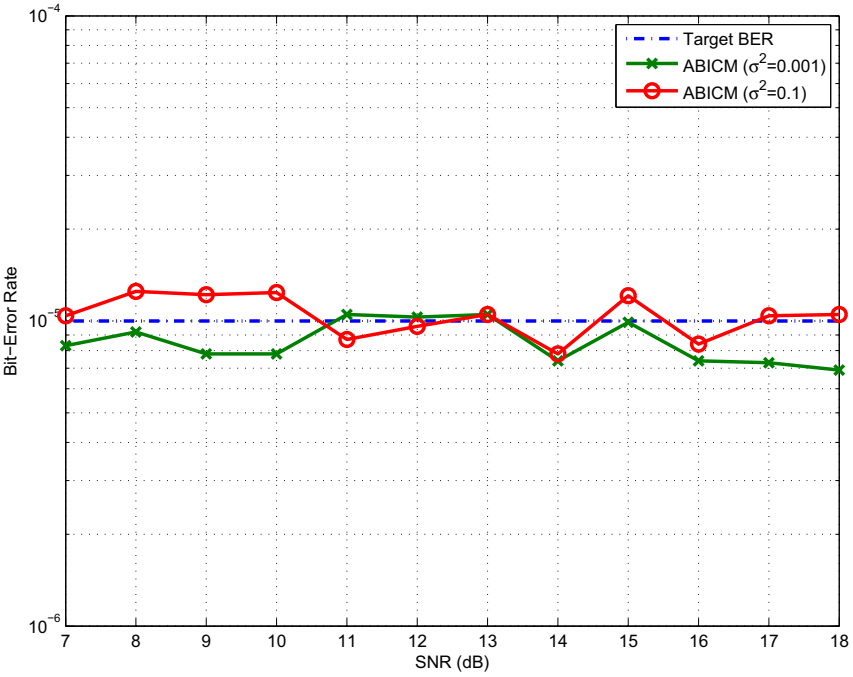

Figure 4.7: BER vs. SNR ($\frac{E_T}{K \times N_0}$) for $\sigma^2 = 0.001$ and $\sigma^2 = 0.1$

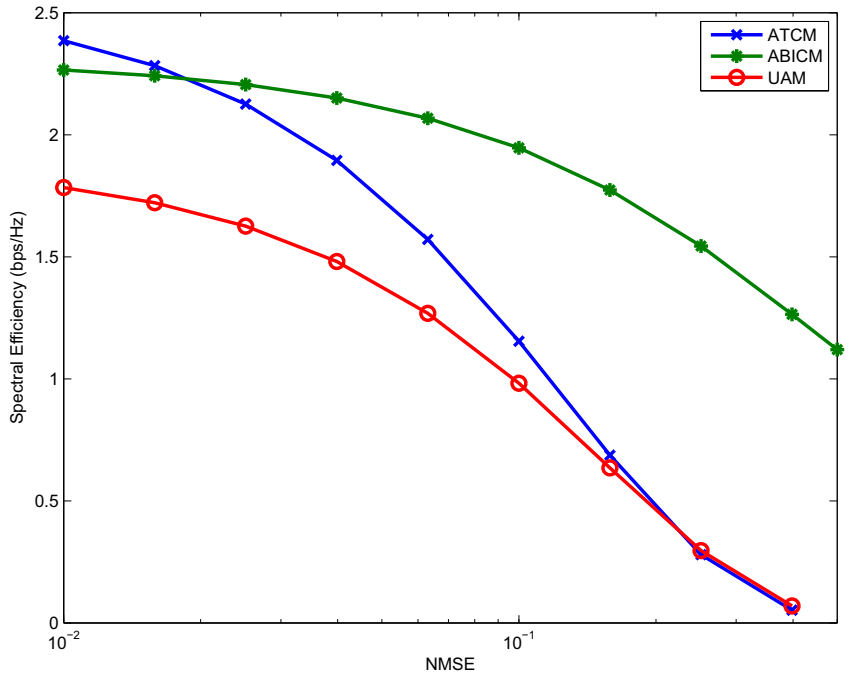

Figure 4.8: BER vs. NMSE for SNR=15 dB

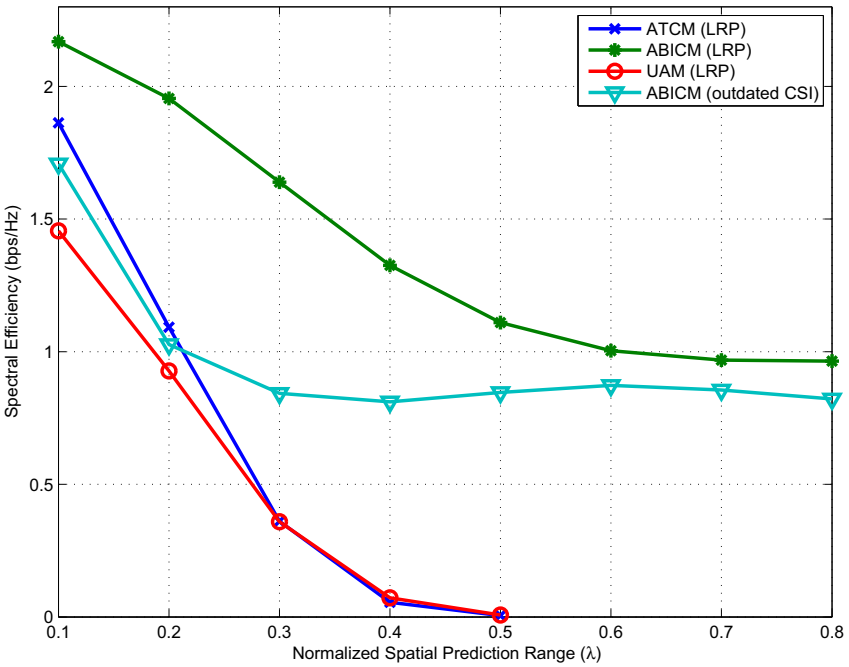

Figure 4.9: BER vs. normalized spatial prediction range for SNR=15 dB

Chapter 5

Conclusions

Adaptive transceiver techniques have evolved as one of the key enabling technologies to meet the increasing demand for high-speed wireless data access services. In this dissertation, we investigated several important topics in the area of adaptive transceiver design and analysis.

For the reverse link of MC-CDMA with AFH, a novel allocation algorithm that outperforms the original WF algorithm was proposed. The proposed allocation algorithm is combined with MUDs using the SINR analysis. It is demonstrated that combined improved subcarrier allocation and MUD is very effective in mitigating MAI, resulting in much larger system capacity than for the non-adaptive MC DS-CDMA system. This conclusion is confirmed for realistic rapidly varying fading channels with correlated subcarriers, CSI mismatch, and imperfect power control. For fading channel prediction-aided UAM and ATCM, a novel DANR method is proposed. Compared with previously investigated pilot-aided NR techniques, this method achieves higher throughput by improving the prediction accuracy while maintaining relatively low pilot rate. Moreover, the adaptive modulation aided by LRP has better performance with the realistic physical model than for the Jakes model in the practical SNR range.

For ABICM, new energy adaptation methods based on the expurgated bound were proposed. Compared with previously investigated techniques, these new methods achieve

better BER accuracy. In particular, one of the proposed methods generates the BER that is very close to the specified target BER. It was shown that ABICM is less sensitive to the prediction errors than the ATCM and UAM. However, the LRP technique still significantly improves the SE of ABICM over the outdated CSI method at practical prediction ranges.

In summary, this dissertation has tackled two key steps in implementation of adaptive transceivers: prediction and adaptation. With the LRP technique, we showed that different adaptive wireless systems, e.g., MC-CDMA with AFH, single and multicarrier adaptive MQAM system, significantly outperform non-adaptive systems. On the other hand, the investigation of adaptive modulation techniques helps us to understand the required prediction accuracy to maintain spectral efficiency. For ATCM and UAM, the NR techniques are required to achieve the desired accuracy at practical SNR values. Moreover, the exploitation of adaptive modulated data symbols in NR improves the prediction accuracy as well as the spectral efficiency.

Bibliography

[1] J. F. Hayes, "Adaptive feedback communications," *IEEE Transactions on Communication Technology*, vol. 16, no. 1, pp. 29–34, Feb. 1968.

[2] L. Hanzo, C. H. Wong, and M. S. Yee, *Adaptive Wireless Transceivers: Turbo-Coded, Turbo-Equalized and Space-Time Coded TDMA, CDMA, and OFDM Systems*. Wiley-IEEE Press, 2002.

[3] "Special issue on adaptive modulation and transmission in wireless systems," *Proc. IEEE*, Feb. 2007.

[4] A. Duel-Hallen, "Fading channel prediction for mobile radio adaptive transmission systems," *Proc. IEEE*, vol. 95, pp. 2299–2313, Dec. 2007.

[5] A. Duel-Hallen, S. Hu, and H. Hallen, "Long-range prediction of fading signals," *IEEE Signal Process. Mag.*, vol. 17, pp. 62–75, May 2000.

[6] S. Semmelrodt and R. Kattenbach, "Investigation of different fading forecast schemes for flat fading radio channels," in *Proc. IEEE VTC*, 2003-Fall, pp. 149–153.

[7] K. E. Baddour and N. C. Beaulieu, "Improved pilot-assisted prediction of unknown time-selective Rayleigh channels," in *Proc. IEEE Int. Conf. Commun. (ICC)*, June 2006, pp. 5192–5199.

[8] J.-K. Hwang and J. H. Winters, "Sinusoidal modeling and prediction of fast fading processes," in *Proc. IEEE GLOBECOM*, Nov. 1998, pp. 892–897.

[9] P. Stoica and R. Moses, *Spectral Analysis of Signals*. Upper Saddle River, NJ: Prentice Hall, 2005.

[10] I. C. Wong and B. L. Evans, "Low-complexity adaptive high-resolution channel prediction for OFDM systems," in *Proc. IEEE GLOBECOM*, Nov. 2006.

[11] T. Zemen and B. H. Fleury, "Time-variant channel prediction using time-concentrated and band-limited sequences," in *Proc. IEEE ICC*, 2006.

[12] R. J. Lyman, "Linear prediction of continuous-time, bandlimited processes, with applications to fading in mobile radio," 2000.

[13] R. J. Lyman and A. Sikora, "Prediction of fading envelopes with diffuse spectra," in *Proc. IEEE ICASSP*, 2005, pp. 753–756.

[14] H. Hallen, A. Duel-Hallen, S. Hu, T.-S. Yang, and M. Lei, "A physical model for wireless channels to provide insights for long range prediction," in *Proc. IEEE MILCOM*, Oct. 2002, pp. 627–631.

[15] T. Ekman, "Prediction of mobile radio channels: modeling and design," Ph.D. dissertation, Uppsala University, Sweden, 2002.

[16] T. Jia, A. Duel-Hallen, and H. Hallen, "Improved long-range prediction with data-aided noise reduction for adaptive modulation systems," in *Proc. 43rd Annual Conference on Information Sciences and Systems*, Princeton, NJ, 2008.

[17] ——, "Performance of adaptive coded modulation enabled by long-range fading prediction with data-aided noise reduction," in *Proc. IEEE MILCOM*, San Diego, CA, Nov. 2008.

[18] R. Steele and W. T. Webb, "Variable rate QAM for data transmission over rayleigh fading channels," in *Proceedings of Wireless '91*, Calgary, Alberta, CA, pp. 1–14.

[19] W. T. Webb and R. Steele, "Variable rate QAM for mobile radio," *IEEE Trans. Commun.*, vol. 43, no. 7, pp. 2223–2230, 1995.

[20] S. Otsuki, S. Sampei, and N. Morinaga, "Square QAM adaptive modulation/TDMA/TDD systems using modulation level estimation with walsh function," *Electronics Letters*, vol. 31, pp. 169–171, Feb. 1995.

[21] A. J. Goldsmith and S.-G. Chua, "Variable-rate variable-power MQAM for fading channels," *IEEE Trans. Commun.*, vol. 45, pp. 1218–1230, Oct. 1997.

[22] ——, "Adaptive coded modulation for fading channels," *IEEE Trans. Commun.*, vol. 46, no. 5, pp. 595–602, May 1998.

[23] S. Falahati, A. Svensson, M. Sternad, and H. Mei, "Adaptive trellis-coded modulation over predicted flat fading channels," in *Proc. IEEE VTC*, vol. 3, 2003, pp. 1532–1536.

[24] G. E. Øien, H. Holm, and K. J. Hole, "Impact of channel prediction on adaptive coded modulation performance in Rayleigh fading," *IEEE Trans. Veh. Technol.*, vol. 53, no. 3, pp. 758–768, May 2004.

[25] K. J. Hole, H. Holm, and G. E. Øien, "Adaptive multidimensional coded modulation over flat fading channels," *IEEE J. Sel. Areas Commun.*, vol. 18, no. 3, pp. 1153–1158, 2004.

[26] D. L. Goeckel, "Adaptive coding for time-varying channels using outdated fading estimates," *IEEE Trans. Commun.*, vol. 47, no. 6, pp. 844–854, July 1999.

[27] P. Ormeci, X. Liu, D. L. Goeckel, and R. D. Wesel, "Adaptive bit-interleaved coded modulation," *IEEE Trans. Commun.*, vol. 49, no. 9, pp. 1572–1581, Sept. 2001.

[28] S. Hara and R. Prasad, "Overview of multicarrier CDMA," *IEEE Commun. Mag.*, vol. 35, pp. 106–133, Dec. 1999.

[29] Q. Chen, E. S. Sousa, and S. Pasupathy, "Multicarrier CDMA with adaptive frequency hopping for mobile radio systems," *IEEE J. Sel. Areas Commun.*, vol. 14, pp. 1852–1858, Dec. 1996.

[30] Y. H. Kim, I. Song, S. Yoon, and S. R. Park, "A multicarrier CDMA system with adaptive subchannel allocation for forward links," *IEEE Trans. Veh. Technol.*, vol. 48, pp. 1428–1436, Sept. 1999.

[31] H. J. Kim, I. Song, J. Lee, and S. Y. Kim, "A truncated adaptive transmission scheme for hybrid multicarrier CDMA/FDM systems in forward link," *IEEE Trans. Veh. Technol.*, vol. 54, pp. 967–976, May 2005.

[32] S. Kondo and L. B. Milstein, "Performance of multicarrier DS CDMA systems," *IEEE Trans. Commun.*, vol. 44, pp. 238–246, Feb. 1996.

[33] T. Jia and A. Duel-Hallen, "Subchannel allocation for multicarrier CDMA with adaptive frequency hopping and decorrelating detection," in *Proc. IEEE MILCOM*, Washingtong, DC, Oct. 2006.

[34] ——, "Performance of improved channel allocation for multicarrier CDMA with adaptive frequency hopping and multiuser detection," in *Proc. IEEE International Conference on Communications*, Beijing, China, 2008, pp. 4780–4784.

[35] K. W. Yip and T.-S. Ng, "Effects of carrier frequency accuracy on quasi-synchronous, multicarrier DS-CDMA communications using optimized sequences," *IEEE J. Sel. Areas Commun.*, vol. 17, pp. 1915–1923, Nov. 1999.

[36] L.-L. Yang and L. Hanzo, "Multicarrier DS-CDMA: a multiple access scheme for ubiquitous broadband wireless communications," *IEEE Commun. Mag.*, vol. 41, pp. 116–124, Oct. 2003.

[37] L. Hanzo and B.-J. Choi, "Near-instantaneously adaptive HSDPA-style OFDM versus MC-CDMA transceivers for WIFI, WIMAX, and next-generation cellular systems," *Proc. IEEE*, vol. 95, no. 12, pp. 2368–2392, Dec. 2007.

[38] F. Adachi, D. Garg, S. Takaoka, and K. Takeda, "Broadband CDMA techniques," *IEEE Wireless Communications*, vol. 12, no. 2, pp. 8–18, 2005.

[39] P. Fan, J. Li, and Z. Cao, "A near optimal subchannel allocation policy in forward links for multicarrier CDMA system," in *Proc. IEEE VTC'01-spring*, vol. 2, Rhodes, Greece, 2001, pp. 896–900.

[40] S. Verdu, *Multiuser Detection*. Cambridge, UK: Cambridge University Press, 1998.

[41] H. Liu, *Signal Processing Applications in CDMA Communications*. Norwood, MA: Artech House Publishers, 2000.

[42] J. Park, J. Kim, S. Choi, N. Cho, and D. Hong, "Performance of MC-CDMA system in non-independent Rayleigh fading," in *Proc. IEEE ICC*, vol. 1, Vancouver, Canada, 1999, pp. 506–510.

[43] T. S. Rappaport, *Wireless Communications: Principles and Practice*, 2nd ed. Upper Saddle River, NJ: Prentice Hall, 2002.

[44] W. C. Jakes, *Microwave Mobile Communications*. New York, NY: Wiley, 1974.

[45] T.-S. Yang, A. Duel-Hallen, and H. Hallen, "Enabling adaptive OFDM for mobile radio channels," in *Proc. IEEE MILCOM*, vol. Vol. 2, 2004, pp. 704–710.

[46] J. K. Cavers, "An analysis of pilot symbol assisted modulation for Rayleigh fading channels," *IEEE Trans. Veh. Technol.*, vol. 40, no. 4, pp. 686–693, Nov. 1991.

[47] U. Madhow and M. Honig, "MMSE interference suppression for direct sequence spread spectrum CDMA," *IEEE Trans. Commun.*, vol. 42, no. 12.

[48] C. Y. Wong, R. S. Cheng, K. B. Letaief, and R. D. Murch, "Multiuser OFDM with adaptive subcarrier, bit and power allocation," *IEEE J. Sel. Areas Commun.*, vol. 17, no. 10, p. 1747.

[49] W. Rhee and J. Cioffi, "Increase in capacity of multiuser OFDM system using dynamic sub-channel allocation," in *Proc. IEEE Veh. Technol. Conf.*, vol. 2, May 2000, pp. 15–18.

[50] J. Jang and K. Lee, "Transmit power adaptation for multiuser OFDM systems," *IEEE J. Sel. Areas Commun.*, vol. 21, no. 2, pp. 171–178, Feb. 2003.

[51] S. Yoon, Y. Cho, C. Chae, and H. Lee, "System level performance of OFDMA forward link with proportional fair scheduling," in *Proc. of IEEE PIMRC*, Barcelona, Spain, 2004.

[52] Z. Han, Z. Ji, and K. J. R. Liu, "Fair multiuser channel allocation for OFDMA networks using nash bargaining and coalitions," *IEEE Trans. Commun.*, vol. 53, no. 8, pp. 1366–1376, Aug. 2005.

[53] V. Poor and S. Verdu, "Probability of error in MMSE multiuser detection," *IEEE Trans. Inf. Theory*, vol. 43, pp. 858–871, May 1997.

[54] W. H. Press, S. A. Teukolsky, W. T. Vetterling, and B. P. Flannery, *Numerical Recipes in C: the Art of Scientific Computing*, 2nd ed. Cambridge, UK: Cambridge University Press, 1997.

[55] H. C. Huang and S. C. Schwartz, "A comparative analysis of linear multiuser detectors for fading multipath channels," in *Proc. IEEE Globecom*, vol. 1, San Francisco, CA, 1994, pp. 11–15.

[56] S. Falahati, A. Svensson, T. Ekman, and M. Sternad, "Adaptive modulation systems for predicted wireless channels," *IEEE Trans. Commun.*, vol. 52, pp. 307–316, Feb. 2004.

[57] S. Zhou and G. B. Giannakis, "Adaptive modulation for multiantenna transmissions with channel mean feedback," *IEEE Trans. Wireless Commun.*, vol. 3, no. 5, pp. 1626–1636, Sept. 2004.

[58] X. Cai and G. B. Giannakis, "Adaptive PSAM accounting for channel estimation and prediction errors," *IEEE Trans. Wireless Commun.*, vol. 4, pp. 246–256, Jan. 2005.

[59] J. Proakis, *Digital Communications*, 4th ed. New York, NY: McGraw-Hill, 2001.

[60] L. Lindobm, A. Ahlen, M. Sternad, and M. Falkenstrom, "Tracking of time-varying mobile radio channels - part II: a case study," *IEEE Trans. Commun.*, vol. 50, pp. 156–167, Jan. 2002.

[61] D. Schafhuber and G. Matz, "MMSE and adaptive prediction of time-varying channels for OFDM systems," *IEEE Trans. Wireless Commun.*, vol. 4, pp. 593–602, Mar. 2005.

[62] T. Eyceoz, S. Hu, and A. Duel-Hallen, "Performance analysis of long range prediction for fast fading channels," in *Proc. 33rd Annual Conference on Information Sciences and Systems (CISS'99)*, 1999, pp. 656–661.

[63] S. Zhou and G. B. Giannakis, "How accurate channel prediction needs to be for transmit-beamforming with adaptive modulation over Rayleigh MIMO channels?" *IEEE Trans. Wireless Commun.*, vol. 3, pp. 1285–1294, May 2004.

[64] G. Ungerboeck, "Trellis-coded modulation with redundant signal sets part ii: state of the art," *IEEE Commun. Mag.*, vol. 25, no. 2, pp. 12–21, Feb. 1987.

[65] C. H. Aldana and J. Cioffi, "Channel tracking for multiple input, single output systems using EM algorithm," in *Proc. IEEE Int. Conf. Commun. (ICC)*, June 2001, pp. 586–590.

[66] K. E. Baddour and N. C. Beaulieu, "Nonparametric doppler spread estimation for flat fading channels," in *Proc. IEEE WCNC*, vol. 2, Baltimore, MD, 2003, pp. 953–958.

[67] R. Raheli, A. Polydoros, and C. K. Tzou, "Per-survivor processing: a general approach to MLSE in uncertain environments," *IEEE Trans. Commun.*, vol. 43, pp. 354–364, Feb. 1995.

[68] C. D. Meyer, *Matrix analysis and applied linear algebra*. SIAM, 2000.

[69] E. Zehavi, "8-PSK trellis codes for a rayleigh channel," *IEEE Trans. Commun.*, vol. 40, pp. 873–884, May 1992.

[70] G. Caire, G. Taricco, and E. Biglieri, "Bit-interleaved coded modulation," *IEEE Trans. Inf. Theory*, vol. 44, no. 3, pp. 927–946, May 1998.

[71] V. K. N. Lau, "Performance analysis of variable rate: symbol-by-symbol adaptive bit interleaved coded modulaiton for Rayleigh fading channels," *IEEE Trans. Veh. Technol.*, vol. 51, no. 3, pp. 537–550, May 2002.

[72] K. Song, A. Ekbal, S. T. Chung, and J. M. Cioffi, "Adaptive modulation and coding (AMC) for bit-interleaved coded OFDM (BIC-OFDM)," *IEEE Trans. Wireless Commun.*, vol. 5, pp. 1685–1694, July 2006.

[73] I. C. Wong and B. L. Evans, "Optimal OFDMA subcarrier, rate, and power allocation for ergodic rates maximization with imperfect channel knowledge," in *Proc. IEEE Int. Conf. on Acoustics, Speech, and Signal Proc.*, 2007.

[74] "Mobile WiMAX - part II: a comparative analysis," http://www.wimaxforum.org, WiMAX Forum, Tech. Rep., 2006.

[75] "Selection procedures for the choice of radio transmission technologies for the UMTS," *ETSI Std. TR 101 112 v. 3.2.0*, 1998.

[76] P. Dent, G. E. Bottomley, and T. Croft, "Jakes fading model revisited," *Electronics Letters*, vol. 29, no. 13, pp. 1162–1163, 1993.

[77] J. Campello, "Optimal discrete bit loading for multicarrier modulation systems," in *Proc. IEEE ISIT*, Cambridge, MA, 1998, p. 193.

[78] D. Hughes-Hartogs, "Ensemble modem structure for imperfect transmission media," US Patents no. 4,679,227, 1985.

[79] D. Divsalar and M. K. Simon, "The design of trellis coded MPSK for fading channels: Performance criteria," *IEEE Trans. Commun.*, vol. 36, no. 9, pp. 1004–1012, Sept. 1988.

[80] A. J. Viterbi and J. K. Omura, *Principles of digital communication and coding.* McGraw-Hill, 1979.

[81] J. Ventura-Traveset, G. Caire, and G. Taricco, "Impact of diversity reception on fading channels with coded modulation. part I: coherent detection," *IEEE Trans. Commun.*, vol. 45, pp. 563–572, May 1997.

[82] E. Biglieri, G. Caire, G. Taricco, and J. Ventuura, "Simple method for evaluating error probabilities," *Electronic Letters*, vol. 32, no. 3, pp. 191–192, Feb. 1996.

APPENDIX

Appendix A. Complexity Analysis of Allocation Algorithms for MC-CDMA with Adaptive Frequency Hopping

In this appendix, we use K,M,N to denote the number of users in the system, the number of subcarriers, and number of substreams/user, respectively. To simplify our results, we assumed that $KN \gg M$, which is usually true for practical systems.

Matched Filter Receiver

In the WF algorithm, the allocation is finished in KN iterations. In each iteration, there are only K divisions. Therefore, this algorithm requires K^2N divisions to finish one allocation.

Next, we consider the complexity of the proposed allocation algorithm (Table 2.2) with MF receiver. At the ith iteration in this algorithm, there are $i-1$ previously assigned substreams and one substream to be assigned. The multiplication/division operation is only needed in the calculation of SINR. The number of required divisions is $i+M-1$ since the number of substreams in each subcarrier is incremented by one due to the new allocated substream. Over all iterations, the total number of divisions in allocation would be

$$\sum_{i=1}^{KN}(i+M-1) = \frac{(KN-1)KN}{2} + MKN \approx \frac{(KN)^2}{2} \tag{A.1}$$

To calculate the power of interference, we also need one addition to calculate the total power on each subcarrier and one subtraction to exclude the power of user itself. After allocating the ith substream, there is one addition to update the total power of interference on that subcarrier. Therefore, the required number of additions/subtractions is $i+M+1$ for the ith iteration and

$$\sum_{i=1}^{KN}(i+M+1) = \frac{(KN+1)KN}{2} + KN + MKN \approx \frac{(KN)^2}{2} \tag{A.2}$$

for all iterations.

Table A.1: Steps in computing the matrix inversion

Operation	# of mult./div.	# of add./sub.
$[\boldsymbol{R}(P_m-1)]^{-1}\boldsymbol{\rho}$	$(P_m-1)^2$	$(P_m-2)^2$
$u\left[\boldsymbol{R}^{-1}(P_m-1)\right]^{-1}\boldsymbol{\rho}$	P_m-1	$(P_m-2)^2$
$u\left[\boldsymbol{R}(P_m)\right]^{-1}\boldsymbol{\rho}\boldsymbol{\rho}^H\left[\boldsymbol{R}(P_m)\right]^{-1}$	$\frac{P_m(P_m-1)}{2}$	0

Linear Decorrelating Detector

Here, we consider the computation complexity of executing recursion (2.22)

The proposed allocation algorithm has KN iterations. In the ith iteration, there are $i-1$ assigned substreams and one substream to be assigned. On the mth subcarrier, there are $P_{m,i}$ assigned substreams. Since the required number of multiplications/divisions $N_{mult/div}$ is a function of $P_{m,i}$, while $P_{m,i}$ is determined by the time-varying channel coefficients, the exact number of operations is not available. However, it is possible to obtain an upper bound for the required number of operations. The derivation is as follows

$$\begin{aligned} N_{mult/div} &\approx \sum_{i=1}^{KN}\sum_{m=1}^{M} 1.5(P_{m,i}+1)^2 \\ &\le 1.5\sum_{i=1}^{KN}(i+M-1)^2 \\ &= \frac{1}{4}\left[KN(KN+1)(2KN+1) - M(M-1)(2M-1)\right] \\ &\approx \frac{(KN)^3}{2} \end{aligned} \tag{A.3}$$

where the following facts are used in deriving (A.3)

$$\sum_{m=1}^{M}(P_{m,i}+1) = i+M-1 \tag{A.4}$$

$$\sum_{m=1}^{M} a_m^2 \le \left(\sum_{m=1}^{M} a_m\right)^2 \text{ for all non-negative } a_m \tag{A.5}$$

and

$$\sum_{i=1}^{n} i^2 = \frac{n(n+1)(2n+1)}{6} \tag{A.6}$$

According to (A.3), we can say that the required number of multiplications/divisions for one allocation is less than $(KN)^3/2$ for large KN, or the computational complexity is $O((KN)^3)$.

Successive Interference Canceller

To compute λ_{SIC} for one substream in (2.14), we need at most $3P_{m,i}$ multiplications/divisions. Then the number of multiplications/divistions required for all substreams in that subcarrier is $3(P_{m,i}+1)^2$. Though the direct computation of Q-function and square root are very complex, they can be implemented simply through a lookup table. Similarly to the calculation for LDD, the required number of multiplications/divistions is bounded by

$$\begin{aligned} N_{mult/div} &\approx \sum_{i=1}^{KN}\sum_{m=1}^{M} 3(P_{m,i}+1)^2 \\ &\leq 3\sum_{i=1}^{KN}(i+M-1)^2 \\ &= \frac{1}{2}\left[KN(KN+1)(2KN+1) - M(M-1)(2M-1)\right] \\ &\approx (KN)^3 \end{aligned} \tag{A.7}$$

Summary

In summary, the order of complexity for various allocation algorithm is shown in Table 2.4.